UNIVERSITÀ DEGLI STUDI DI MILANO

DEPARTMENT OF PHYSICS

PH.D. SCHOOL IN
PHYSICS, ASTROPHYSICS AND APPLIED PHYSICS
CYCLE XXXVIII

Monitoring phonon dynamics in quantum materials by Time-Resolved Raman Scattering

Disciplinary Scientific Sector PHYS/03A

Ph.D. Thesis of:

Alice Margherita Finardi
ORCID 0009-0005-2295-9815
Matr. R13971

Director of the School: Prof. A. Mennella
Supervisor of the Thesis: Prof. G. Rossi
Co-supervisor of the Thesis: Dr. R. Cucini

A.Y. 2024-2025

Commission of the final examination:

External Referees:
Prof. G. Cerullo & Prof. I. Zardo

External Members:
Prof. G. Cerullo & Prof. I. Zardo

Internal Member:
Prof. G. Rossi

Final examination:

23rd January 2026
Dipartimento di Fisica, Università degli Studi di Milano, Italy

But then science is nothing but a series of questions that lead to more questions, which is just as well, or it wouldn't be much of a career path, would it?

T. Pratchett

Cover illustration:
A. M. Finardi
Internal illustrations:
A. M. Finardi
Design:
A.D. Copia, Copiae

MUR subject:
PHYS/03A

Contents

Abstract

This thesis collects the results of my work as doctoral student of the Ph.D. School in Physics, Astrophysics and Applied Physics at Università degli Studi di Milano, that has been carried out since October 2022 at the Istituto Officina dei Materiali of the Consiglio Nazionale delle Ricerche (IOM-CNR) and within the framework of Nanoscale Foundries and Fine Analysis (NFFA) facility.

My research activity has been devoted to the study of phonon dynamics in photoexcited quantum materials, employing time-resolved spontaneous Raman spectroscopy (TRRS) as the primary experimental approach. Among ultrafast spectroscopies, TRRS provides unique access to phonons and other low-energy excitations in systems impulsively driven into transient non-equilibrium states, allowing mode-specific monitoring of their population dynamics. This makes TRRS particularly powerful for investigating electron-phonon and phonon-phonon couplings, as well as the evolution of crystal symmetries after photoexcitation. Motivated by the broad span of applications of this technique and by its complementarity with other ultrafast spectroscopies targeting electronic, lattice or spin degrees of freedom, a dedicated TRRS setup was developed at the NFFA-SPRINT laboratory, hosted in the premises of the FERMI@Elettra facility (Elettra-Sincrotrone Trieste).

This booklet thus summarizes my work for the commissioning and characterization of the new setup, and presents the results from three case studies addressing the properties of semiconductors, 2D chalcogenides and a strong correlated oxide. In a first experiment, the phonon relaxation dynamics of silicon is investigated. The possibility of tuning the phonon-phonon anharmonic interaction is explored by varying the external temperature and the excitation density. Furthermore, the photodoping dynamics is directly monitored via a Fano interference effect between electronic and phononic Raman scattering. A second experiment, targeting bulk and single-layer MoS_2, reveals a photodoping-induced phonon frequency renormalization and a long-lived excitation anisotropy in the phonon subsystem, dictated by mode symmetries and inaccessible under equilibrium conditions. In a third experiment, TRRS is employed to monitor the evolution of the lattice symmetry of magnetite and the phonon-specific energy flow while triggering a photoinduced Verwey phase transition.

Introduction

Understanding how the macroscopic properties of materials emerge from their microscopic building blocks is probably the central goals of condensed matter physics. Since the 1930s, the complexity of interactions between different degrees of freedom has been encoded in the concept of quasiparticles, *i.e* electrons, holes, phonons, magnons, and others, which provide the language through which we describe both the ground state of a material and its excitations from it generated by external perturbations. The energies, lifetimes, momentum dispersions, and mutual interactions of quasiparticles govern a wide range of fundamental and technologically relevant properties, from charge transport, thermal conductivity, and light absorption/emission, to emergent phenomena such as magnetism, charge-ordering, superconductivity. Conventional equilibrium spectroscopies provide invaluable access to these properties but remain fundamentally limited to information about the interaction averaged over all scattering channels.

In contrast, time-resolved spectroscopies offer a direct view into how different degrees of freedom exchange energy and momentum. By impulsively driving a system out of equilibrium and probing its subsequent relaxation back to a stable state, they enable the temporal separation of distinct interactions. This allows to address the interplay between specific degrees of freedom, estimate the coupling strengths between specific quasiparticles, and in some cases access metastable states that are not reachable from thermodynamic equilibrium conditions. The rapid development of ultrashort pulsed light sources has made these approaches possible. Femtosecond lasers, high-harmonic generation sources, and free-electron lasers now cover a broad energy range from the terahertz to the hard X-ray regime, enabling time-resolved extensions of nearly all major spectroscopies.

Within this broad landscape, time-resolved spontaneous Raman spectroscopy (TRRS) has proven itself to be a particularly powerful probe. Raman scattering is uniquely suited to probe phonons and other low-energy bosonic excitations. In a pump-probe implementation, TRRS provides simultaneous access to phonon populations, frequencies, linewidths, as well as lattice symmetry properties, thus allowing to extract information about electron–phonon and phonon–phonon couplings, as well as on structural dynamics accompanying phase transitions. Its capability to offer a clear, mode-resolved picture of lattice dynamics without requiring coherent phonon excitation, is particularly valuable in light of the growing need for accurate interpretations of the results of time-resolved experiments and the exploration of phononic approaches to controlling material properties, both requiring to move beyond treating the lattice subsystem as a single

thermal reservoir. Moreover, when integrated with time-resolved optical and electronic spectroscopies that probe electronic degrees of freedom, TRRS can become a key element of multi-messenger research in the time domain.

This is the general framework and motivation in which the present thesis is developed. In particular, the work presented here is devoted to the application of TRRS to the study of phonon dynamics in photoexcited quantum materials, and has led to the original experimental results reported here.

On the methodological side, the research included the commissioning of a new TRRS end-station at the NFFA-SPRINT laboratory, designed to provide state-of-the-art access to ultrafast lattice dynamics within a UHV-compatible environment. The setup was conceived to ensure full interoperability with other sample-growth and spectroscopic methods available in the NFFA facility, thereby enabling a true multi-messenger approach in which experimental campaigns employing multiple complementary techniques can be conducted under reproducible environmental condition. The project is the result of a joint effort by IOM-CNR, Università degli Studi di Milano, Università di Perugia, and Sapienza Università di Roma, and is intended to become part of the NFFA research infrastructure as a user facility.

Thesis Overview

The thesis is structured in three main parts.

Part I lays the groundwork for this thesis. It introduces the motivation for developing a time-resolved spontaneous Raman spectroscopy (TRRS) setup and situates the present experimental work within the broader context of time-resolved spectroscopic studies. It also provides the theoretical and experimental background needed to understand the performed measurements.

Chapter 1 motivates the study of phonon dynamics out of equilibrium. It first discusses the ways in which time-resolved spectroscopies allow to go beyond equilibrium investigations, and then focuses on the specific advantages of TRRS, highlighting its distinctive features compared with other time-resolved phonon probes.

In Chapter 2 the theoretical foundations of spontaneous Raman scattering are provided, with a particular focus on the information about phonons that can be retrieved in a typical Raman spectroscopy experiment.

Chapter 3 outlines the principles of TRRS, reviewing the physical insights that can be obtained with this technique and providing examples of typical case studies present in literature. It also discusses the effects of using a pulsed source, rather than a continuous-wave one, as a probe.

Part II (Chapter 4) describes the experimental realization of TRRS at the NFFA-SPRINT laboratory. The chapter details the design of the optical scheme and the sample environment, presents the characterization measurements carried out during the commissioning of the setup, and concludes with perspectives for further developments.

Part III presents the results of three case studies.

Chapter 5 reports on silicon, chosen as a benchmark system to validate the TRRS setup. The dynamics of the longitudinal optical phonon is investigated, exploring the effect of different temperatures and fluences on the photoexcitation of long-lived carriers (detected through a dynamical Fano interference effect) and anharmonic phonon–phonon interactions.

Chapter 6 focuses on MoS_2, in both bulk and monolayer form. TRRS reveals a strong effect of transient photodoping on the phonon frequencies, and fluence-dependent data suggest the presence of different photodoping regimes. The chapter highlights the potential of mode-specific mapping of phonon populations with TRRS, showing how it can reveal specific electronic de-excitation pathways and the persistence of long-lived nonthermal phonon states.

Lastly, Chapter 7 addresses magnetite, a paradigmatic strongly correlated oxide undergoing a complex metal-insulator and structural phase transition (Verwey transition) mediated by strong electron phonon coupling. In this case, TRRS demonstrates its ability to simultaneously monitor the dynamics of lattice symmetry changes, phonon spectral modifications, and the transient populations of phonons and low-energy modes, proving its potential in the investigations of photoinduced phase transitions.

Part I

Background

CHAPTER 1

Probing phonons out of equilibrium

1.1 Why time-resolved spectroscopies?

Experimental condensed matter physics addresses the study of the macroscopic properties of materials and of the microscopic physical interactions from which they emerge. This is crucial both for advancing our understanding of fundamental physics and for the possibility of control and tailor material properties, with the ultimate aim of designing systems with the desired electrical, elastic, thermal, magnetic (or other) functionalities.

In order to achieve this, it is necessary to characterize the electronic and structural ground state of a material, and the low-energy excitations, which determine its response to external stimuli. A wide range of spectroscopic techniques has been developed to this aim, employing probes with different sensitivities to access specific degrees of freedom of the material. Furthermore, by varying thermodynamic parameters such as temperature, pressure, or by doping, spectroscopic investigations allow to explore the stability limits of the material ground state and map its proximity in the system energy landscape to possible competing phases.

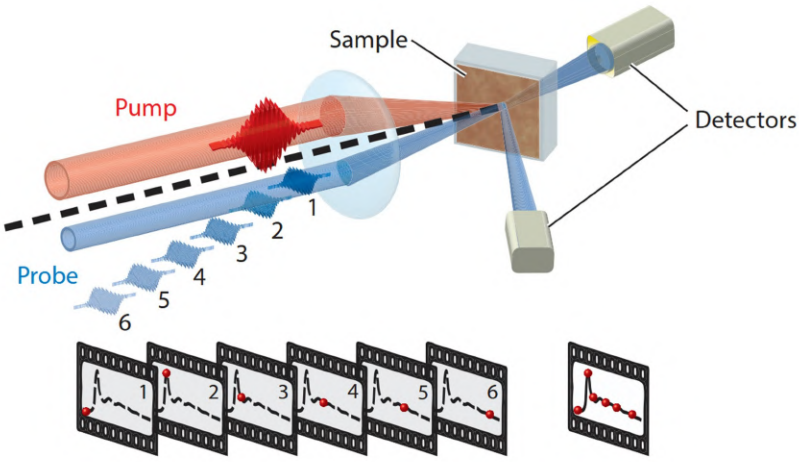

Figure 1.1: Schematic representation of a pump-probe experiment. A pump pulse (red) is used to excite the sample out of equilibrium. A second probe pulse (blue) reaches a sample at a controlled delay, allowing to measure the response of the material at a very precise instant. From [1].

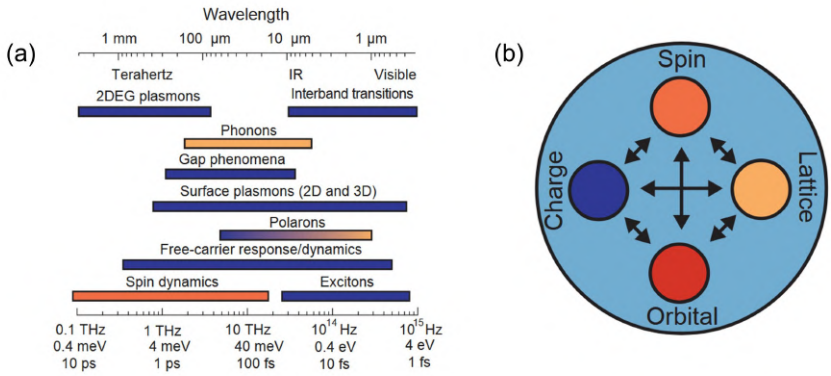

Figure 1.2: (a) Typical fundamental excitations in a complex solid material, plotted against the corresponding energy, timescale and resonant photon energy. (b) Scheme of the mutually interacting degrees of freedom in a condensed matter system. Reproduced from [2].

It is, however, possible to go beyond this type of investigations by driving a material out of its thermodynamic equilibrium state and then probing it while it is in a non-equilibrium transient state. This approach not only provides access to properties of the ground state that remain "hidden" at equilibrium, such as the strength of coupling between different degrees of freedom, but also allows to "test" the system stability, revealing transient or metastable phases, and ultimately providing hints to develop strategies for the dynamical control of the material properties.

This progress has been made possible by the development of time-resolved spectroscopies, enabled by the availability of increasingly short pulsed, energy tunable light sources. To capture the transient configurations the time resolution of the measurement must be shorter than the relaxation time of the system towards equilibrium. This timescale varies widely depending on the material and the process under investigation, but for most of the dynamics of interest in condensed matter systems (electronic, charge, lattice, spin dynamics) it is "ultrafast", i.e. in the range of picoseconds and below, as illustrated in Figure 1.2 [1, 3].

In most ultrafast time-resolved spectroscopies, this temporal resolution is achieved through the pump–probe method (Figure 1.1). In this approach, the system is first brought to an excited state by a first ultrashort laser pulse (the pump), and then interrogated by a second pulse (the probe) at controlled delays. By varying the optical path length of one of the beams, this delay can be tuned with sub-femtosecond precision. The result is a sequence of "snapshots" of the system while its state evolves as a consequence of the energy deposited by the pump, allowing to investigate the photoexcited state and map the relaxation back to a thermodynamic ground state.

Coherent pulsed table-top sources spanning the THz to Soft X-ray spectral range and temporal resolution now approaching the $10^{-17} - 10^{-16}$ second scales [4–6], combined with Free-Electron Lasers extending this coverage into the hard X-ray regime, have led to the development of time-resolved counterparts of most equilibrium spectroscopies and scattering methods and inspired novel approaches, giving rise to an exceptionally vast landscape of ultrafast techniques. A complete overview of time-resolved (TR) techniques is out of scope here; however, it is useful to outline the main ways in which pump-probe

methods allow to go beyond equilibrium investigations and the underlying motivations, in order to contextualize the studies presented in this thesis.

By carefully selecting the pump characteristics (energy, fluence, duration) and therefore the type of excitation created in the system, as well as the initial state of the material, time-resolved experiments can indeed be tailored to address different goals.

Probing relaxation pathways and couplings between degrees of freedom

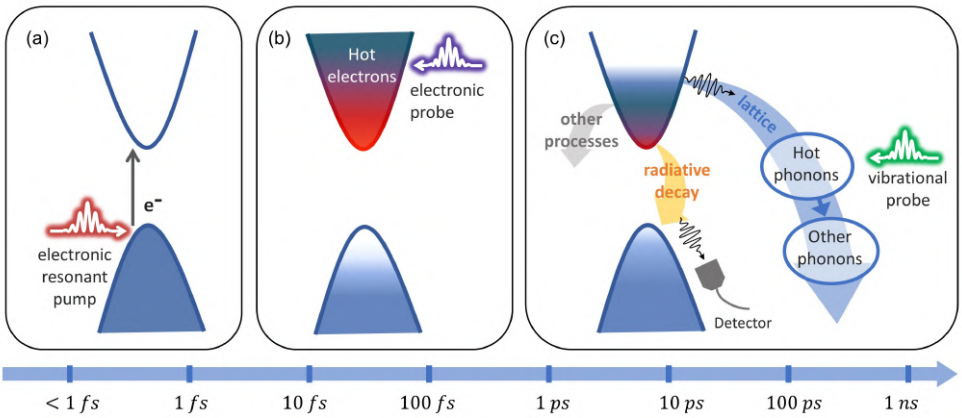

Figure 1.3: Excitation and deexcitation processes in a prototypical pump-probe experiment and relative timescale. (a) A pump pulse prompts electrons from the ground state to higher-energy levels. (b) Electrons thermalize to a high-temperature quasi-equilibrium distribution. (c) Electrons relax towards the ground state via different processes, including energy transfer to lattice degrees of freedom. In (b) and (c) probe pulses interrogating different degrees of freedom are shown.

A first class of pump-probe experiments is dedicated to achieve a better understanding of the equilibrium properties of a material by perturbing it with a controlled excitation source and monitoring the relaxation back to the initial ground state by a probe sensitive to a well-defined quasiparticle. In fact, the properties of the quasiparticles through which we describe the ground state and low-energy excitations of condensed matter systems (electrons, holes, phonons, magnons) are determined by their "dressing", given by interactions with all the other quasiparticles. In equilibrium measurements, such interactions can only be inferred from the energy broadening of populated states, inversely proportional to their average lifetime which results from all scattering channels combined. In contrast, monitoring the dynamics of a given quasiparticle in a previously photoexcited system, makes it possible to separate on the temporal scale different excitation and decay processes. For sufficiently weak perturbations, which do not change the system free-energy landscape, these processes are governed by the same interactions that govern equilibrium properties. The pump-probe approach allows to resolve the rate at which the energy exchange develops between different degrees of freedom (or between different quasiparticles of the same type) develops; in this way, such method enables to estimate of the specific coupling strengths among quasiparticles [4, 6, 7].

A clear example is provided by the studies of relaxation pathways in photodoped semiconductors, which include two of the three experimental investigations presented in this thesis. As schematically illustrated in Figure 1.3, the arrival of an optical pump

excites electrons to higher-energy bands, resulting in an out-of-equilibrium electron distribution. Within the first tens to hundreds of femtoseconds, the electron population thermalizes via electron-electron scattering to a high quasi-equilibrium temperature (*i.e.* electrons obey an interal equilibrium statistics associated to an effective temperature higher than that describing the thermodynamical behaviour of the other degrees of freedom in the system). This is followed by a cascade of relaxation processes that progressively redistribute the excess of energy among the different degrees of freedom: cooling of the electron population through electron-phonon scattering (occuring over hundreds of femtoseconds to a few picoseconds), internal thermalization of the phonon subsystem via phonon-phonon scattering (a few to tens of picoseconds), radiative and non-radiative recombination of the excited carriers, and finally heat diffusion (nanoseconds to microseconds). By selecting probes with suitable sensitivity and temporal resolution, time-resolved spectroscopies are able to access the different stages of this relaxation and disentangle the various pathways, for instance distinguishing between electronic decay channels occurring on different timescales and producing distinct experimental signatures.

Exploring quasi-equilibrium and hidden metastable phases

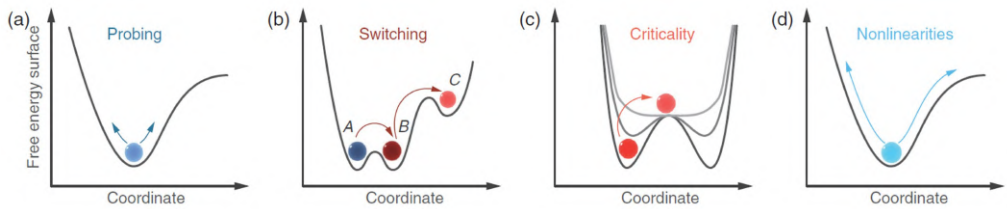

Figure 1.4: Nonthermal pathways triggered by laser excitation. The panels illustrate the system state in a potential or free energy landscape as a function of a system coordinate, such as an electronic order parameter or a lattice displacement. (a) Weak excitations around the ground state allow to probe low-energy modes and their mutual couplings. (b) A more intense or more energetic laser pulse can drive the system in an alternative ground state B or to a metastable hidden state C. (c) An even more intense excitation can modify the free-energy landscape itself, inducing non-equilibrium critical behaviour. (d) A strong excitation can also drive the system into anharmonic regimes allowing to probe nonlinear effects and change effective couplings in the material. Reproduced from [8].

At thermodynamic equilibrium, the stability of a material state is determined by the permanence of the system at a minimum of the free-energy landscape, despite thermal fluctuations. Equilibrium measurements therefore allow us to study the system in proximity of this minimum, or, in the presence of phase transitions, to map the succession of thermodynamic equilibrium states as the free-energy landscape evolves, leading to a new minimum.

Time-resolved spectroscopies, by contrast, can test the limits of stability of a phase by inducing perturbations that are stronger than thermal fluctuations and monitor the dynamics for the re-establishment of the initial state (Figure 1.4 (a)). Moreover, ultrashort laser pulses can drive an out-of-equilibrium phase transition and force it along specific dynamical pathways, by transiently changing the coupling between relevant degrees of freedom (Figure 1.4 (d)). This approach is particularly powerful in strongly correlated

materials, where the intricate interplay of electronic, spin, and structural degrees of freedom produces complex phase diagrams characterized by multiple competing ordered states. Accessing transient non-equilibrium states makes it possible to identify which orders are in competition as the transients may mimick actual phases (magnetic, superconducting, topological), and to determine which degree of freedom ultimately governs the selection of the equilibrium ground state, a question that equilibrium measurements alone cannot typically resolve.

Even more intriguingly, ultrafast experiments have revealed the possibility to drive the system into hidden phases, *i.e.* to create novel quantum states located in regions of the free energy landscape that cannot be reached by spontaneous fluctuations from thermal equilibrium (Figure 1.4 (b, c)).

Such studies have been applied across a broad range of correlated materials, with notable examples including charge-density-wave systems, metal–insulator transitions in Mott materials such as VO_2 and manganites, superconductors, as well as other transition metals oxides such as magnetite [1, 4, 7, 8].

Coherent control of transient states

One of the challenging attempts by ultrafast science is the non-thermal control and manipulation of quantum material properties through light. In this case, intense pulses are tailored in energy, polarization, wavefront, to induce a specific coherent driving of the system, forcing it along a selected trajectory in phase space, re-ranking competing orders (suppressing some and enhancing others), or inducing ultrafast switching between distinct ordered states [8, 9].

Remarkably, such selective excitation can produce effects against naïve expectations. For example, instead of destabilizing ordered phases by heating, energy deposited into specific degrees of freedom can stabilize or even create long-range order. Fascinating demonstrations include the light-induced enhancement of superconductivity [10] and ferroelectricity [11], and the emergence of chirality in an initially non-chiral crystal [12].

We note that there is a natural logical progression between the three types of ultrafast investigations: envisioning and achieving coherent control of a material state requires a deep understanding of the coupling between the different degrees of freedom, their role in stabilizing the equilibrium ground state, and the location of nearby states of interest in the free energy landscape.

The studies presented in this thesis fall primarily into the first of the described categories (and, in the case of magnetite, extend partly into the second), investigating relaxation pathways in the phonon subsystem and expanding the knowledge about the changes that can be induced by non-thermal perturbations, such as the generation of a long-lived anisotropic phonon distribution in MoS_2, or the photoinduced phase transition in magnetite.

1.2 Why time-resolved spontaneous Raman spectroscopy?

Because this thesis is devoted to the study of phonon dynamics in photoexcited quantum materials, a focus is required on the motivation for investigating these specific degrees of freedom and on the techniques available for this purpose, highlighting the particular characteristics of the method employed here: time-resolved spontaneous Raman scattering (TRRS).

First of all, phonons represent the fundamental collective excitations of the atomic nuclei in a solid, and, as such, one of the basic building blocks of condensed matter. The phonon interactions among different modes and with the electronic degrees of freedom, govern a wide range of macroscopic properties, including elastic properties, thermal conductivity, carrier mobility and electrical conductivity, thermal lattice expansion, and band gap renormalization as a function of temperature. Phonons also play a crucial role in determining the stability of a given lattice structure and in the emergence of long-range ordered phases such as superconductivity (formation of Cooper-pairs) and charge-density waves. In light of the discussion in the previous section, one clearly grasps the interest in probing phonons with time-resolved spectroscopies. Such approaches allow to determine excitation/relaxation pathways and to directly address the microscopic couplings (electron-phonon, phonon-phonon, etc.) that regulate the interactions mentioned above. A variety of ultrafast spectroscopies have been developed to investigate the out-of-equilibrium properties of phonons and their dynamics. Among these are time-resolved (TR) reflectivity and transmission, four-wave mixing techniques such as transient-grating spectroscopy (TG) and femtosecond stimulated Raman scattering (FSRS), time-resolved X-ray diffraction (TR-XRD), ultrafast electron diffraction (UED) and ultrafast electron diffuse scattering (UEDS), besides, naturally, TRRS.

A relevant distinction should be drawn here between techniques that probe coherently excited phonons and those that probe incoherent phonons. TR-reflectivity and TR-transmission, as well as TG, detect phonon excitations from the oscillatory modulation they induce in time on the optical properties of the material [4, 13]. These techniques thus require the excitation of coherent phonons, creating a net average displacement of the ions at a given instant in time. While with some differences, FSRS is also based on the coherent driving of Raman active-phonons [14]. By contrast, UED, UEDS, TR-XRD, and TRRS are sensitive to the incoherent phonon excitation, *i.e.* randomly phased vibrations that follow the lattice normal modes but do not produce a net atomic displacement at any instant. These techniques thus exist as phonon probes also in their equilibrium counterparts, in which they measure the spontaneous thermal populations of the modes. When implemented in pump–probe schemes, they can monitor the time evolution of phonon populations as they are modified by photoexcitation and by interactions with other excited degrees of freedom.

Although both types of techniques provide information about the equilibrium and out-of-equilibrium phonon frequencies, the relaxation processes they probe are intrinsically different. In the first case, the characteristic decay time of the probed phonon mode reflects the loss of coherence of the collective excitation, while in the second case it corresponds to the decay of the population of that specific phonon due to the transfer of energy to other degrees of freedom.

While coherent phonon generation has many valuable applications, incoherent phonon probes offer the significant advantage of not relying on specific coherent excitations induced by the pump pulse to access lattice dynamics. This makes them versatile tools, with no restriction on the type of pump to be used and thus applicable to a wide variety of excitation conditions. TRRS studies, in particular, have indeed been carried out both with optical pumping, depositing energy into the electronic subsystem and probing phonons subsequently excited via electron-phonon coupling, as well as with mid-infrared pumping, in which case optical phonons are generated by the decay of coherently driven modes and can be used as a tool to monitor the system while controlling its state with a selected excitation [13, 15].

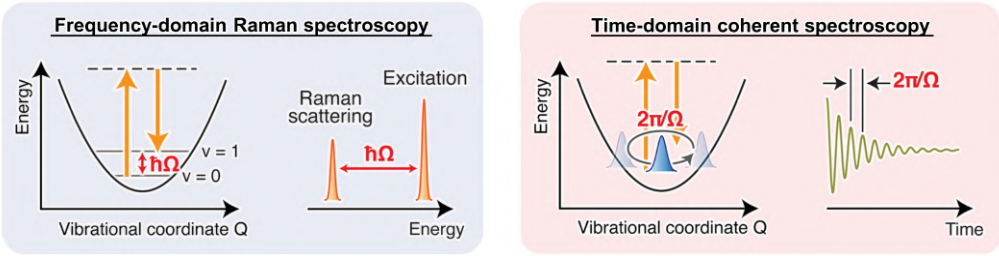

Figure 1.5: Schematic of frequency- and time-domain phonon spectroscopies. In Raman spectroscopy, both at equilibrium and in out-of-equilibrium conditions, the vibrational energy of Raman-active modes is measured as an energy difference in the spectrum of the scattered radiation. In time-domain spectroscopies, coherent phonon modes are observed as the temporal oscillation of the optical signal as a function of the pump-probe delay and the frequency can be retrieved from the period of oscillation. Adapted from [16].

In the specific case of TRRS, the versatility of the pump is combined with other advantages.

First, since the measurement is performed in the frequency domain, the temporal dynamics induced by the pump is intrinsically separated from the spectral analysis of the phonon modes. As shown in Figure 1.5, in techniques measuring in the time-domain, such as time-resolved reflectivity/transmission and TG, the phonon mode frequencies and linewidths are extracted from the measured oscillation profile in time through Fourier analysis. Therefore, possible changes induced by the pump on the phonon modes characteristics, such as a transient frequency shift, are superimposed to the modulation that allows to extract the object of the measurement itself. Conversely, in TRRS, phonon frequencies and linewidths are obtained directly in the frequency domain, thus intrinsically separated from the modulations induced by the pump, allowing an accurate measurement of these quantities at each chosen delay from the pump.

A second advantage is that TRRS does not require a resonant condition between the probe photon energy and the material electronic or vibrational modes. This allows the use of sources in the optical range, very convenient from a technical point of view, and brings significant experimental flexibility. In addition, compared to other incoherent probes, TRRS benefits from being a low-energy-photon-based technique. Unlike UED or UEDS, it does not suffer from the complications inherent to electron spectroscopies, and unlike TR-XRD, it can be performed with compact tabletop setups rather than requiring large-scale facilities.

Finally, it is worth noting that each of these spectroscopies is subject to specific selection rules, which define their sensitivity to phonons of different symmetry and wavevector. TRRS, as will be detailed in the following chapters, is limited to Raman-active excitation with $q \approx 0$, whereas for example UEDS can access phonons only away from the Brillouin zone center [17, 18]. Thus, while TRRS is a powerful probe of phonon dynamics, it is important to recognize that no single approach can provide time-resolved access to the full phonon spectrum. A complete picture inevitably requires the complementary use of multiple techniques.

CHAPTER 2

Fundamentals of Raman Spectroscopy

The Raman effect was first observed in 1928 by C.V. Raman and K.S. Krishnan, who discovered that when light is scattered by matter, the "ordinary" diffused radiation, at the same frequency as the incident beam, is accompanied by weaker radiation shifted to a lower frequency [19]. Since the invention of laser, this effect has become the foundation of Raman spectroscopy, an effective and widely used technique for investigating condensed matter systems.

When a material is illuminated by electromagnetic radiation, incident photons may undergo several different processes: they can be transmitted without interacting with the material, absorbed, or scattered. Most scattered photons undergo elastic Rayleigh scattering, in which their momentum is changed but their energy is conserved. Instead, Raman-scattered photons undergo an inelastic scattering process, in which they either gain energy from an active low-energy mode of the material (antiStokes process) or reduce it by creating a new excitation (Stokes process). The energy difference between the incident and scattered photons is therefore equal to the energy of such mode. The resulting spectrum of the scattered radiation thus consists of a central Rayleigh peak at the laser frequency ω, accompanied by two weaker sidebands at $\omega \pm \omega_\nu$, corresponding to the Stokes and antiStokes components, as schematically illustrated in Figure 2.1. Because low-energy excitations are often associated to ionic degrees of freedom, Raman spectroscopy of solid state materials is generally used to obtain direct information about lattice symmetries and dynamics. Nonetheless, other degrees of freedom (*e.g.* electronic or magnetic) can also generate Raman scattering channels, broadening the scope of the technique.

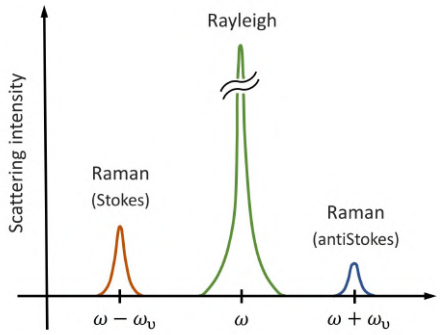

Figure 2.1: Schematic representation of the scattering spectrum of radiation from a material illuminated by a field at frequency ω. Raman peaks are shifted from the elastic (Rayleigh) peak by ω_ν, *i.e.* the frequency of a low-energy excitation of the material. The typical orders of magnitude of the peaks intensities (not reported in the appropriate scale in the graph) are $I_{Rayleigh} \sim 10^{-3} I_0$, $I_{Raman} \sim 10^{-6} I_0$.

This chapter provides a theoretical description of the Raman effect. A semiclassical model is first presented to build physical intuition, followed by a full quantum treatment. The discussion is based primarily on [20–22].

2.1 Semiclassical model

A first theoretical description of the Raman effect can be obtained within a semiclassical framework. Although this approach does not account for all the observed properties of Raman scattering, it is worth introducing because of its simplicity and its ability to provide intuitive insights into Raman selection rules.

Let us consider first the interaction of a single diatomic molecule with electromagnetic radiation, *i.e.* with an oscillating electric field of the form $\mathbf{E} = \mathbf{E}_0 \cos(\omega t)$. Under the action of $\mathbf{E}$, a dipole moment $\boldsymbol{\mu}$ is induced in the system. If the field is not too strong, the dipole moment is given within the framework of linear response theory and can be expressed as:

$$\boldsymbol{\mu} = \alpha \mathbf{E} = \alpha \mathbf{E}_0 \cos(\omega t) \tag{2.1}$$

where α is the polarizability of the molecule. The induced dipole moment thus oscillates in time, acting in turn as a source of electromagnetic field. If we assume α as a time independent quantity, the dipole will radiate at the same frequency ω as the incoming radiation, giving rise to Rayleigh elastic scattering. However, the polarizability can be tuned by the internal degrees of freedom of the system. If we consider the diatomic molecule to be vibrating with frequency ω_v, the consequent modulation of the interatomic distance can lead to a variation in time of the polarizability, which can be expanded in a Taylor series around the equilibrium distance R_0:

$$\alpha(R) = \alpha_0 + \left.\frac{\partial \alpha}{\partial R}\right|_{R=R_0} (R - R_0) \tag{2.2}$$

where $\alpha_0 = \alpha(R_0)$. Representing the molecular vibration as an harmonic oscillator with normal coordinate $R - R_0 = q_v = q_v^0 cos(\omega_v t)$, the expression for the dipole moment becomes:

$$\begin{aligned} \boldsymbol{\mu} &= \alpha_0 \mathbf{E}_0 \cos(\omega t) + \mathbf{E}_0 \left.\frac{\partial \alpha}{\partial R}\right|_{R=R_0} q_v^0 cos(\omega t) cos(\omega_v t) \\ &= \alpha_0 \mathbf{E}_0 \cos(\omega_0 t) + \frac{\mathbf{E}_0}{2} \left.\frac{\partial \alpha}{\partial R}\right|_{R=R_0} q_v^0 [\cos((\omega - \omega_v)t) + \cos((\omega + \omega_v)t)] \end{aligned} \tag{2.3}$$

where we can notice the appearance, along with the first term associated with Rayleigh scattering, of new components of the emitted radiation at shifted frequencies with respect to the exciting field ($\omega \pm \omega_v$), corresponding to the Stokes and anti-Stokes components of the Raman effect.

The model shown above can be easily extended to the case of a crystal. In this case, including the wavevector dependence explicitly, the interaction with a sinusoidal field $\mathbf{E}(\mathbf{r}, t) = \mathbf{E}(\mathbf{k}, \omega) \cos(\mathbf{k} \cdot \mathbf{r} - \omega t)$ will induce in the material a polarization:

$$\begin{aligned}\mathbf{P}(\mathbf{r},t) &= \alpha(\mathbf{k},\omega)\mathbf{E}(\mathbf{r},t) \\ &= \alpha_0(\mathbf{k},\omega)\mathbf{E}(\mathbf{k},\omega)\cos(\omega t) + \frac{1}{2}\mathbf{E}(\mathbf{k},\omega)\frac{\partial\alpha}{\partial\mathbf{Q}}\bigg|_0 \mathbf{Q}(\mathbf{q},\omega_v)\cdot \\ &\cdot\{\cos[(\mathbf{k}-\mathbf{q})\cdot\mathbf{r}-(\omega-\omega_v)t] + \cos[(\mathbf{k}+\mathbf{q})\cdot\mathbf{r}-(\omega+\omega_v)t]\}\end{aligned} \tag{2.4}$$

where $\mathbf{Q}(\mathbf{r},t) = \mathbf{Q}(\mathbf{q},\omega_v)\cos(\mathbf{q}\cdot\mathbf{r}-\omega_v t)$ is now the lattice displacement associated to a phonon mode and $\alpha_0(\mathbf{k},\omega) = \alpha(\mathbf{k},\omega)|_{\mathbf{Q}=0}$.

A simple semiclassical description thus allows to account for the Raman effect, satisfying both the conservation of energy and the conservation of momentum. Moreover, it provides a first criterion for identifying Raman-active vibrational modes from the selection rule $\frac{\partial\alpha}{\partial\mathbf{Q}}\Big|_0 \neq 0$. In other words, unlike infrared absorption, Raman scattering does not require a vibration to induce a permanent dipole moment; rather, the vibration must modulate the polarizability.

Nevertheless, the semiclassical model fails to explain some key experimental observations, such as the systematic intensity difference between Stokes and antiStokes peaks ($I_S > I_{AS}$), or resonance enhancements at specific excitation wavelengths. A rigorous description of the Raman effect therefore requires a full quantum treatment.

2.2 Quantum description

From the quantum point of view, any scattering process can be schematized as follows: an incident photon of energy $\hbar\omega$ is absorbed by the system bringing it to a virtual excited state, and this is followed by the decay to a final steady state with the emission of a new photon. The intermediate virtual state can be considered a quantum state with a lifetime so short that it cannot be directly measured, and thus with such a large energy indetermination to make a temporary violation of conservation of energy possible. As shown in Figure 2.2, if the final state is equal to the initial state, the Rayleigh elastic process occurs. However, the virtual state can also decay to an energy level different from the initial one, giving rise to an inelastic scattering process. In the case of Raman scattering by vibrational modes, the system decays to the initial electronic state but to vibrational level at higher or lower energy by emitting a Stokes ($\omega_S = \omega - \omega_v$) or antiStokes ($\omega_{AS} = \omega + \omega_v$) photon, respectively. The antiStokes process clearly requires the initial state to be an excited state of the system.

It is possible to derive the expression of quantum Raman cross section from perturbation theory, considering the radiation-matter interaction as a perturbation on the non-interacting systems. We thus consider the Hamiltonian of the system to be

$$H = H_0 + H_{int} \qquad H_0 = H_{mat} + H_{rad} \tag{2.5}$$

where the non-interacting Hamiltonian H_0 appropriately describes the system at $t \to \pm\infty$. The radiation-matter interaction term, obtained with the minimal coupling prescription, can be expressed as:

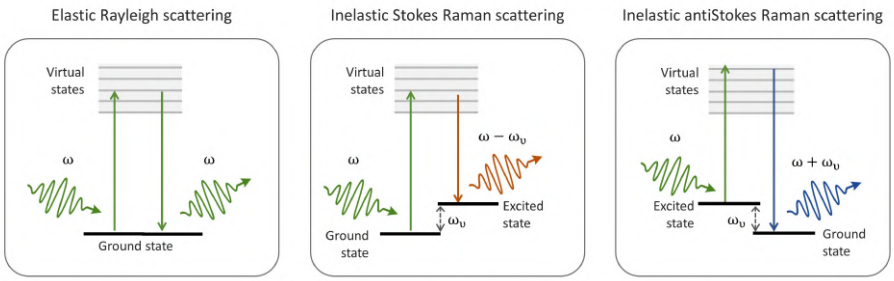

Figure 2.2: Schematic representation of elastic and inelastic scattering processes from a quantum point of view.

$$\begin{aligned} H_{int} &= H_1 + H_2 \\ H_1 = -\frac{e}{mc}\sum_i \mathbf{A}(\mathbf{r}_i)\cdot\mathbf{p}_i \qquad & H_2 = \frac{e^2}{2mc^2}\sum_i \mathbf{A}^2(\mathbf{r}_i) \end{aligned} \tag{2.6}$$

Here **A** is the vector potential operator of the applied field:

$$\mathbf{A}(\mathbf{r}) = \sum_{\mathbf{k},\lambda}\sqrt{\frac{2\pi\hbar c^2}{V\omega_{\mathbf{k}}}}\left(a_{\mathbf{k},\lambda}e^{i\mathbf{kr}} + a^\dagger_{\mathbf{k},\lambda}e^{-i\mathbf{kr}}\right)\hat{\boldsymbol{\epsilon}}_{\mathbf{k},\lambda} \tag{2.7}$$

where $a^\dagger_{\mathbf{k},\lambda}, a_{\mathbf{k},\lambda}$ are the creation and annihilation operators of a photon with momentum $\mathbf{k}$ and polarization λ and $\hat{\boldsymbol{\epsilon}}_{\mathbf{k},\lambda}$ is the corresponding polarization vector.

The scattering process then describes the transition from an initial $|i\rangle$ to a final state $|f\rangle$, which, being eigenstates of the non-interacting system, can be expressed as a tensor product of a photon eigenstate and an eigenstate of the material:

$$|i\rangle = |1_{\mathbf{k},\lambda}, 0_{\mathbf{k'},\lambda'}\rangle|A\rangle \qquad |f\rangle = |0_{\mathbf{k},\lambda}, 1_{\mathbf{k'},\lambda'}\rangle|B\rangle \tag{2.8}$$

where

$$\begin{aligned} H_{mat}|A\rangle &= E_A|A\rangle \qquad & H_{mat}|B\rangle &= E_B|B\rangle \\ H_{rad}|1_{\mathbf{k},\lambda}, 0_{\mathbf{k'},\lambda'}\rangle &= \hbar\omega|1_{\mathbf{k},\lambda}, 0_{\mathbf{k'},\lambda'}\rangle & H_{rad}|0_{\mathbf{k},\lambda}, 1_{\mathbf{k'},\lambda'}\rangle &= \hbar\omega'|0_{\mathbf{k},\lambda}, 1_{\mathbf{k'},\lambda'}\rangle \end{aligned} \tag{2.9}$$

The transition probability from $|i\rangle$ to $|f\rangle$ per unit time is then given by Fermi golden rule:

$$W_{fi} = \frac{2\pi}{\hbar}|\langle f|T|i\rangle|^2\delta(E_f - E_i) \tag{2.10}$$

where the transition matrix $\langle f|T|i\rangle$ is given by:

$$\langle f|T|i\rangle = \langle f|H_{int}|i\rangle + \sum_{l\neq i}\frac{\langle f|H_{int}|l\rangle\langle l|H_{int}|i\rangle}{E_i - E_l} + \ldots \tag{2.11}$$

at different perturbation orders.

Since the vector potential 2.7 is linear in $a_{\mathbf{k},\lambda}$ and $a^{\dagger}_{\mathbf{k},\lambda}$, its action on an eigenstate of the system changes the state by only the creation/destruction of a single photon. Thus in expression 2.11, the first-order terms in **A** describe one-photon emission and absorption processes, and vanish in the present case. The transition matrix for scattering processes is given by second-order terms in **A**:

$$\langle f|T|i\rangle = \langle f|H_2|i\rangle + \sum_{l\neq i} \frac{\langle f|H_1|l\rangle\langle l|H_1|i\rangle}{E_i - E_l} \tag{2.12}$$

For optical photons the dipole approximation $e^{i\mathbf{kr}} \approx 1$ can be applied, and it can be shown that the first term in equation 2.12 vanishes for $A \neq B$, *i.e.* for inelastic scattering processes such as Raman scattering.

In the remaining term, only two photon states give a non-zero contribution to the sum over all possible virtual intermediate states:

$$|l\rangle = |0_{\mathbf{k},\lambda}, 0_{\mathbf{k'},\lambda'}\rangle|I\rangle \qquad |l\rangle = |1_{\mathbf{k},\lambda}, 1_{\mathbf{k'},\lambda'}\rangle|I\rangle \tag{2.13}$$

where $|I\rangle$ is a virtual energy level of the material. Thus the expression 2.12 reduces to:

$$\begin{aligned} T_{Raman} = \sum_I & \frac{\langle B|\langle 0_{\mathbf{k},\lambda}, 1_{\mathbf{k'},\lambda'}|H_1|0_{\mathbf{k},\lambda}, 0_{\mathbf{k'},\lambda'}\rangle|I\rangle\langle I|\langle 0_{\mathbf{k},\lambda}, 0_{\mathbf{k'},\lambda'}|H_1|1_{\mathbf{k},\lambda}, 0_{\mathbf{k'},\lambda'}\rangle|A\rangle}{E_A + \hbar\omega - E_I} + \\ + & \frac{\langle B|\langle 0_{\mathbf{k},\lambda}, 1_{\mathbf{k'},\lambda'}|H_1|1_{\mathbf{k},\lambda}, 1_{\mathbf{k'},\lambda'}\rangle|I\rangle\langle I|\langle 1_{\mathbf{k},\lambda}, 1_{\mathbf{k'},\lambda'}|H_1|1_{\mathbf{k},\lambda}, 0_{\mathbf{k'},\lambda'}\rangle|A\rangle}{E_A - E_I - \hbar\omega'} \end{aligned} \tag{2.14}$$

where the two terms arise from different possible time-orderings of the scattering process. Inserting expression 2.6 it can be shown that the transition matrix simplifies to:

$$T_{Raman} = \frac{2\pi\hbar\sqrt{\omega_{\mathbf{k}}\omega_{\mathbf{k'}}}}{V}\, \hat{\boldsymbol{\epsilon}}_{\mathbf{k},\lambda} \cdot \tilde{\boldsymbol{R}} \cdot \hat{\boldsymbol{\epsilon}}_{\mathbf{k'},\lambda'} \tag{2.15}$$

where we defined the Raman tensor:

$$\tilde{\boldsymbol{R}} = \sum_I \Big[\frac{\boldsymbol{\mu}_{BI}\boldsymbol{\mu}_{IA}}{E_A + \hbar\omega - E_I} + \frac{\boldsymbol{\mu}_{IA}\boldsymbol{\mu}_{BI}}{E_A - E_I - \hbar\omega'}\Big] \tag{2.16}$$

given in terms of the matrix elements of the dipole moment operator $\boldsymbol{\mu} = e\sum_i \mathbf{r}_i$.

Using the derived expression, the transition probability becomes:

$$W_{fi} = \frac{(2\pi)^3\hbar}{v^2}\omega\omega'|\hat{\epsilon}_{\mathbf{k},\sigma} \cdot \tilde{\boldsymbol{R}} \cdot \hat{\epsilon}_{\mathbf{k'},\sigma'}|^2\delta(E_f - E_i) \tag{2.17}$$

Finally, introducing the final density of states for the photons $g(\mathbf{k'})d\mathbf{k'} = \frac{V}{(2\pi)^3}k'^2dk'd\Omega$ and the incident flux of photons $\Phi_{inc} = \frac{c}{V}$ it is possible to write the scattering cross section for a photon with wavevector between **k'** and **k'** + d**k'**:

$$d\sigma = \frac{W_{fi}\rho(\mathbf{k'})d\mathbf{k'}}{\Phi_{inc}} = \hbar c k k'^3|\hat{\epsilon}_{\mathbf{k},\sigma} \cdot \tilde{\boldsymbol{R}} \cdot \hat{\epsilon}_{\mathbf{k'},\sigma'}|^2\delta(E_f - E_i)dk'd\Omega \tag{2.18}$$

and the differential cross section:

$$\frac{d\sigma}{d\Omega dE'} = \frac{\omega\omega'^3}{c^4}|\hat{\epsilon}_{\mathbf{k},\sigma} \cdot \tilde{\boldsymbol{R}} \cdot \hat{\epsilon}_{\mathbf{k}',\sigma'}|^2 \delta(\hbar\omega' - (\hbar\omega - \Delta E_{BA})) \tag{2.19}$$

where the conservation of energy, containing $\Delta E_{BA} = E_B - E_A$, was made explicit.

Notice here how Raman cross-section depends on the fourth power of the frequency of the exciting radiation ($\omega \approx \omega'$), a strong dependence which suggests the use of high frequency radiation for Raman spectroscopy experiments. However, given the second order Raman process would be obscured by possible first-order processes such as absorption by resonant electronic transitions (typically in the UV range), Raman spectroscopy is most commonly performed in the visible-near infrared spectral region.

The expression of the Raman tensor also reveals the possibility of resonance enhancement when the excitation wavelength is appropriately chosen. In fact, in equation 2.16, the denominators tend to zero when $\hbar\omega \approx \hbar\omega' \simeq E_I - E_A$, leading to a divergence in $\tilde{\boldsymbol{R}}$. Although a proper treatment of this divergence is beyond the scope of this discussion, under such conditions a large (but finite) enhancement of the Raman cross-section is obtained. Physically, this condition is realized when the virtual intermediate state accessed during the scattering process is close in energy to an excited eigenstate of the material.

2.3 Scattering by phonons and Stokes and antiStokes intensities

It should be noted that, in the treatment so far, no assumptions have been made regarding the specific nature of the initial and final internal states of the material $|A\rangle$ and $|B\rangle$, nor about the type of excitation responsible for the difference between them. The above formulation thus includes the possibility of changing the system electronic, vibrational or spin state, and indeed Raman scattering has been experimentally observed in association with a variety of low energy excitations, including electronic transitions, phonons, and magnons.

Yet, the case most commonly studied with Raman spectroscopy, as well as the main topic of this thesis, is Raman scattering by phonon modes. In this case, the states of the system should be described by an electronic and a lattice part, coupled through the electron-lattice interaction described by the Hamiltonian H_{EL}. The interaction with light would then not alter the electronic state of the system, which would be the ground state for both the initial and final configurations, but would rather modify the lattice part through the creation or annihilation of phonons. For one-phonon creation, this can be described by expressing the initial and final states as:

$$\begin{aligned} |A\rangle &= |0; n_\nu\rangle + \sum_a \frac{|a; n_\nu + 1\rangle\langle n_\nu + 1; a|H_{EL}|0; n_\nu\rangle}{E_0 - E_a - \hbar\omega_\nu} \\ |B\rangle &= |0; n_\nu + 1\rangle + \sum_b \frac{|b; n_\nu\rangle\langle n_\nu; b|H_{EL}|0; n_\nu + 1\rangle}{E_0 + \hbar\omega_\nu - E_b} \end{aligned} \tag{2.20}$$

where 0 denotes the electronic ground states, a and b intermediate electronic states, and n_ν is the number of phonons with energy $\hbar\omega_\nu$ [23].

Combining these expressions with equation 2.16, another common form for the Raman tensor, expressed in terms of the electron-lattice and electron-radiation interactions (H_{ER}), can be derived:

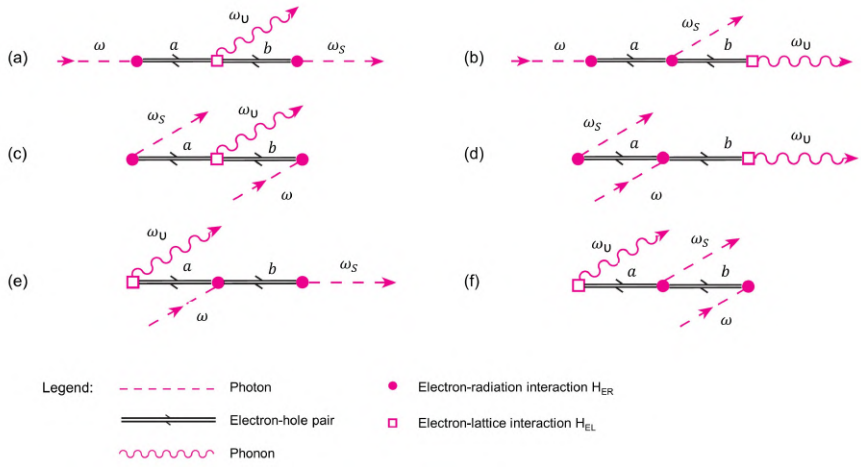

Figure 2.3: Feynman diagrams for the six scattering processes that contribute to one-phonon Stokes Raman scattering. Adapted from [22].

$$\tilde{\boldsymbol{R}} = \sum_{a,b} \frac{\langle n_\nu + 1; 0|H_{ER}|a; n_\nu + 1\rangle\langle n_\nu + 1; a|H_{EL}|b; n_\nu\rangle\langle n_\nu; b|H_{ER}|0; n_\nu\rangle}{[\hbar\omega - (E_a - E_0)][\hbar\omega - \hbar\omega_\nu - (E_b - E_0)]} + \ldots \quad (2.21)$$

where $H_{ER} \equiv H_1$, since the direct coupling of photons with the lattice modes is negligible, and H_{EL} contains the creation and destruction operators of phonons $b_\nu, b_\nu^\dagger$. The omitted terms correspond to all the possible time orderings of the processes, represented by the Feynman diagrams in Figure 2.3, giving rise to the complete six-term expression reported elsewhere [22].

Equation 2.21 highlights more clearly the role of the electron-phonon coupling in determining the Raman scattering intensities. In fact H_{EL}, which we do not report explicitly, contains the deformation potential matrix, which describes the modulation of the electronic potential induced by the lattice deformation [20]. This factor, just as the classical analogous $\frac{\partial\alpha}{\partial\mathbf{Q}}$, depends on the symmetry of each vibrational mode, and ultimately determines the symmetry of the Raman tensor $\tilde{\boldsymbol{R}}$. Thus, once inserted in the bilinear product with the photon polarization vectors (as shown in equation 2.19) it gives rise to the Raman selection rules.

Finally, by inserting the explicit expression of H_{EL} into equation 2.21 and accounting for the optical properties of the material (*i.e.* reflection, absorption and refraction effects), the expression for the Stokes scattering rate at a specific wavelength can be derived [24]:

$$R'_S = \left[\frac{T_S T_L P_L \omega_S^3 \Delta\Omega}{(\alpha_L + \alpha_S)\eta_L \eta_S}\right]\left[\frac{n_\nu + 1}{32\pi^2 c^4 \omega_\nu}\right]|\hat{\epsilon}_{\mathbf{k},\sigma} \cdot \tilde{\boldsymbol{R}} \cdot \hat{\epsilon}_{\mathbf{k}',\sigma'}|^2 \quad (2.22)$$

and, extending the treatment to the case of the destruction of a phonon, for the antiStokes scattering rate:

$$R'_{AS} = \left[\frac{T_{AS}T_L P_L \omega_{AS}^3 \Delta\Omega}{(\alpha_L + \alpha_{AS})\eta_L \eta_{AS}}\right]\left[\frac{n_\nu}{32\pi^2 c^4 \omega_\nu}\right] |\hat{\epsilon}_{\mathbf{k},\sigma} \cdot \tilde{\boldsymbol{R}} \cdot \hat{\epsilon}_{\mathbf{k'},\sigma'}|^2 \tag{2.23}$$

where $\eta_L, \eta_S, \eta_{AS}$ are the indices of refraction at the laser (ω), Stokes ($\omega_S = \omega - \omega_\nu$) and antiStokes frequencies ($\omega_{AS} = \omega + \omega_\nu$), while $\alpha_L, \alpha_S, \alpha_{AS}$ are the corresponding absorption coefficients, and T_L, T_S, T_{AS} the transmission coefficients. P_L is the laser power, $\Delta\Omega$ the collection solid angle. Defining a factor $C = \frac{T_L P_L \Delta\Omega}{32\pi^2 c^4 \eta_L \omega_\nu}$ containing all constants equal for both Stokes and antiStokes sides, the rates take the compact form:

$$\begin{aligned} R'_S &= C\frac{T_S}{(\alpha_L + \alpha_S)\eta_S}\omega_S^3 (n_\nu + 1)\chi^2 \\ R'_{AS} &= C\frac{T_{AS}}{(\alpha_L + \alpha_{AS})\eta_{AS}}\omega_{AS}^3\, n_\nu\, \chi^2 \end{aligned} \tag{2.24}$$

where we defined $\chi^2 = |\hat{\epsilon}_{\mathbf{k},\sigma} \cdot \tilde{\boldsymbol{R}} \cdot \hat{\epsilon}_{\mathbf{k'},\sigma'}|^2$ for brevity.

From this expression, it is clear that the difference in intensity between the Stokes and antiStokes peaks is naturally explained within the quantum model. Being associated with the creation and annihilation of a phonon, respectively, the scattering rate for the Stokes process contains the eigenvalue of the creation operator, $n_\nu + 1$, while the antiStokes process contains the eigenvalue of the annihilation operator, n_ν. Assuming that the optical constants do not vary significantly between the Stokes and antiStokes sides (a reasonable approximation when ω is far from resonances, given the small energy difference between the two peaks compared to electronic energy scales), the phonon population can therefore be extracted from the antiStokes/Stokes intensity ratio as:

$$\frac{R'_{AS}}{R'_S} \approx \frac{\omega_{AS}^3}{\omega_S^3}\frac{n_\nu}{n_\nu + 1} = \left(\frac{\omega + \omega_\nu}{\omega - \omega_\nu}\right)^3 e^{-\frac{\hbar\omega_\nu}{k_B T}} \tag{2.25}$$

where, in the last term, the Bose–Einstein distribution for the phonon population, $n_\nu(T) = \frac{1}{e^{\frac{\hbar\omega_\nu}{k_B T}} - 1}$, has been used, highlighting the pronounced temperature dependence of $\frac{R'_{AS}}{R'_S}$.

While giving more details about the theory of Raman spectroscopy is beyond the scope of this thesis, three additional remarks are worth mentioning:

- **Raman linewidth.** In the treatment presented so far, no broadening mechanisms were considered, resulting in a Raman spectrum composed of discrete delta functions. If a finite lifetime of phonons (primarily arising from anharmonic phonon-phonon scattering) is taken into account, each Raman spectral feature associated with a specific phonon excitation acquires a Lorentzian profile, with a linewidth inversely proportional to the phonon lifetime [20].

- **Momentum conservation.** The explicit dependence on the phonon momentum q was also omitted for simplicity, but the overall conservation of momentum requires $\mathbf{q} = \mathbf{k'} - \mathbf{k}$. However, when visible light is employed, the photon momentum ($\sim 10^5 cm^{-1}$) is negligible compared to the typical size of the first Brillouin zone ($\sim 10^8 cm^{-1}$). This justifies the common approximation $|\mathbf{q}| \approx 0$, *i.e.* that Raman scattering probes vibrational modes at the Γ point.

- **Higher-order Raman processes.** The discussion in this section has been limited to first-order Raman processes, involving the creation or annihilation of a single phonon. However, by extending the expansion in equation 2.20, second- or higher order Raman processes can be taken into account, in which two or more phonons are excited/deexcited as a result of the interaction. In these cases, momentum conservation applies to the sum of phonon momenta: higher order processes allow to relax the constraint $|\mathbf{q}| \sim 0$ and access vibrational modes away from the Brillouin-zone centre, including acoustic branches. This type of phenomena has typically a much lower intensity than first-order processes, but can be enhanced under resonance conditions. Importantly, the scattering rate of higher-order processes depends on the population of all modes involved, and the temperature dependence of the antiStokes to Stokes ratio is modified accordingly. For instance, in the case of the excitation of two identical phonons [25]:

$$\frac{R'_{AS}}{R'_{S}} \propto \frac{n_\nu^2}{(n_\nu + 1)^2} = e^{-\frac{2\hbar\omega_\nu}{k_B T}} \tag{2.26}$$

CHAPTER 3

Time-Resolved Spontaneous Raman Spectroscopy

Applying the pump–probe scheme to spontaneous Raman spectroscopy enables to access all the information contained in the Raman cross-section in a time-resolved manner. The result is a particularly informative technique, given that, as detailed in the previous chapter, the Raman spectra provide data on the phonon frequencies, symmetries, lifetimes, populations, and possibly also on the electronic population. In this chapter I describe how the relevant information can be extracted from pump–probe Raman measurements, and what insights it provides into the microscopic and macroscopic properties of the investigated system. The implications of performing Raman spectroscopy with an ultrashort probe pulse are also discussed.

3.1 Raman spectroscopy on a pumped system

As discussed in Chapter 1, the key difference between spontaneous time-resolved Raman spectroscopy (TRRS) and the other main optical techniques probing nonequilibrium phonon dynamics lies in the fact that, in TRRS, the probe triggers the same scattering events as in equilibrium measurements [26]. The possibility to probe phonons, indeed, does not rely on the creation of a coherent excitation. Thus, spontaneous TRRS provides access to the transient state phonon properties of the examined system, while it is captured in an out-of-equilibrium condition induced by the pump, e.g., in presence of a photoexcited hot carrier or hot phonon temporary population [13].

In the pump–probe configuration, it is therefore possible to map the Raman signal as a function of the delay from the system excitation, and follow the temporal evolution of the frequency, the linewidth, and the intensity of each peak independently. In the following, I summarize the main information on the microscopic properties and the macroscopic state of the system that can be extracted from TRRS measurements and provide examples of relevant studies conducted on condensed matter systems.

Equivalent phonon temperature

The primary strength of TRRS is its capability to directly access the excitation and relaxation dynamics of phonons or, more generally, any measured Raman-active excitation. Experimentally, the creation of an additional phonon population induced by the pump is typically evidenced by a marked increase in the antiStokes peak intensity.

From equation 2.25, it is clear how the simultaneous measurement of the Stokes and antiStokes sides of the Raman spectrum allows to extract the phonon population and the temperature. At equilibrium, this approach is routinely used for thermometry applications, allowing to extract the local temperature of a sample. In TRRS, instead, it enables

mapping the photoexcited phonon population, often expressed in terms of an effective nonequilibrium phonon temperature, according to:

$$n_\nu(t) = \left[\left(\frac{\omega + \omega_\nu(t)}{\omega - \omega_\nu(t)} \right)^3 \frac{I_S(t)}{I_{AS}(t)} - 1 \right]^{-1}$$
$$T_\nu(t) = \frac{\hbar\omega_\nu(t)}{k_B} \left[ln \left(\frac{I_S(t)}{I_{AS}(t)} \left(\frac{\omega + \omega_\nu(t)}{\omega - \omega_\nu(t)} \right)^3 \right) \right]^{-1} \tag{3.1}$$

where the temporal dependence indicates that we are referring to the measured values at each pump-probe delay, and the temperature is to be intended as an effective "local" temperature in time.

In principle the dynamical modification of the phonon population can be estimated comparing the intensity of a single side of the spectrum (typically the antiStokes, owing to its stronger dependence on n_ν) at positive and negative delays. However, such an approach may be affected by pump-induced variations in the Raman tensor or in the optical constants, introducing additional temporal dependencies in equation 2.24. By contrast, in the Stokes/antiStokes intensity ratio these effects are automatically cancelled out, making it the more robust approach to the analysis of the transient state.

From the measured rise and decay dynamics, it is then possible to extract the characteristic timescale for the phonon excitation (determined by electron–phonon or, for modes weakly coupled with the electronic subsystem, phonon–phonon scattering) and the lifetime of its population (determined by its anharmonic coupling to other phonons). Remarkably, unlike spectroscopies measuring in the time-domain, TRRS allows these quantities to be obtained independently for each measured phonon mode. This is particularly relevant. At equilibrium, the extracted phonon temperature is essentially the same for all modes, since it reflects the lattice temperature (exception made for special cases involving resonances or a strong variation of optical constants in the probed frequency range, where 2.25 is not applicable). Out of equilibrium, however, the population of a given phonon mode depends on the coupling strength of the specific branch and wavevector with the degree of freedom where the pump energy is initially transferred (usually the electronic subsystem). As a result, the relaxation process proceeds through nonequilibrium phonon distribution states that may persist for several ps before eventually thermalizing via phonon–phonon interactions. Having mode-resolved access to phonon dynamics therefore enables the identification of energy relaxation pathways within the phonon subsystem, allowing to add a fine structure to the simplified three-temperature models commonly used to reproduce the nonequilibrium dynamics of materials, in which the lattice is described by the use of a single temperature.

Mapping the phonon relaxation dynamics has been one of the central goals of TRRS studies since the very first experiments in a condensed matter system (by von der Linde *et al.* in 1980 [27] and Kash *et al.* in 1985 [28]), dedicated to monitor the nonequilibrium LO phonon population in GaAs generated by the energy relaxation of optically created electron–hole pairs. More recently, the investigation of relaxation pathways in graphite, achieved through the combined use of TRRS and TRARPES, has provided experimental evidence for the necessity of including phonon–phonon interactions in any realistic description of hot-carrier relaxation [29]. This conclusion is further supported

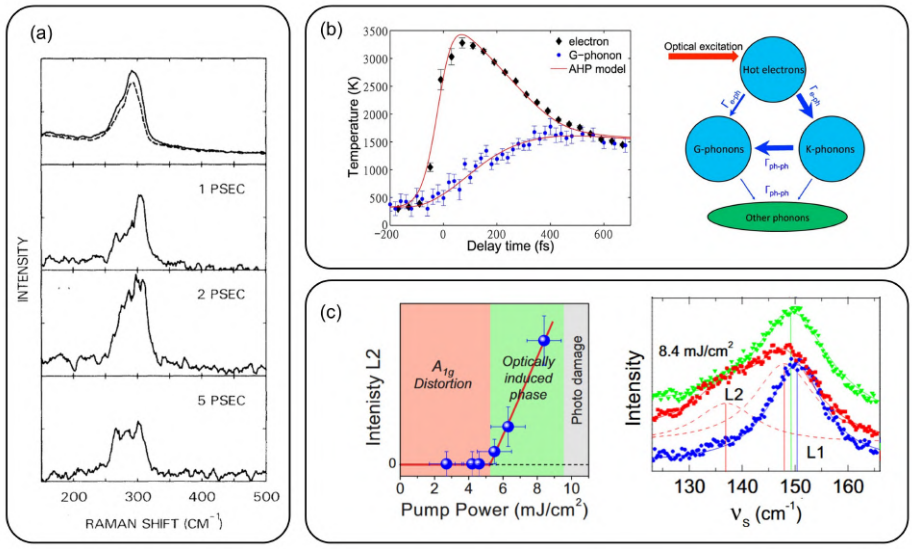

Figure 3.1: Examples of TRRS studies on phonon relaxation dynamics and excitations/deexcitation pathways and photoinduced phase transitions. (a, top panel) AntiStokes Raman spectrum for room temperature GaAs at 1 ps delay (continuous line) and negative delay (dashed line). (a, other panels) Difference spectra at various delays. Adapted from [27]. (b) Comparison of the dynamics of electronic temperature (black, measured by TRARPES) and G-phonon temperature (blue, measured by TRRS) in graphite and sketch of energy transfer during the hot carrier relaxation. Adapted from [29]. (c) Detection of a photoinduced phase transition in antimony from the maximum intensity of the new vibrational mode L2. TRRS spectra at pump-probe delays of -10 ps, 1 ps and 20 ps are shown in blue, red and green, respectively. Adapted from [30].

by the measurements on MoS_2 presented in Chapter 6 of this thesis, where the comparison of phonon temperatures across different modes, both optical and acoustic, reveals pronounced and long-lived transient anisotropies in the phonon population across the Brillouin Zone.

It should be noticed, however, that the identification of relaxation pathways is intrinsically limited to phonon modes that are measurable by Raman spectroscopy, typically zone-center optical modes allowed by the selection rules. Nevertheless, second-order Raman processes may in some cases grant access to zone-edge modes or acoustic phonons. A further limitation arises at low temperature, where the antiStokes intensity can easily drop below the noise level of the detection system. In that case the noise level imposes a threshold on the minimum measurable phonon population increase.

Phonon spectrum modifications

In addition to intensity variations, it is also possible to observe in TRRS spectra pump-induced changes in the position and linewidth of the Raman peaks. Unlike phonon population dynamics, such effects are not universally present in all pumped samples, but when observed they can reveal distinctive phenomena and macroscopic modifications of the material. First, shifts and broadenings of the Raman peaks may indicate the presence of time-dependent strain, for example due to the generation of a propagating

strain pulse within the material [31].

Furthermore, since the phonon spectrum is inherently linked to the crystal symmetry, Raman spectroscopy is sensitive to structural transient distortions or phase transitions that induce symmetry modifications. Indeed, temperature-dependent equilibrium Raman measurements are routinely employed to identify novel phases and determine the corresponding transition temperatures. In the pump–probe configuration, TRRS can thus reveal the presence of new optically induced phases through the appearance or disappearance of phonon peaks and track the subsequent dynamics of recovery towards the equilibrium state, or, conversely, highlight their possible metastable character. TRRS has been thus used for example to uncover the possibility of inducing an ultrafast transition in Peierls-distorted antimony to a structural phase inaccessible under thermal equilibrium conditions [30], and, in this thesis, it is employed to detect a photoinduced Verwey transition in magnetite (see Chapter 7).

Moreover, the sensitivity of Raman spectroscopy to low-energy excitations besides phonons allows TRRS to detect phase transitions other than structural ones: in cuprates, the Raman peak associated with Cooper-pair breaking provides a marker of the superconducting phase, enabling the monitoring of its transient suppression under optical pumping [32, 33].

In this context, a particular strength of TRRS lies in the possibility of directly comparing the dynamics of the observed phase transition with that of the population of phonons and/or other quasiparticles, extracted from the antiStokes/Stokes intensity ratio within the same experiment. This capability is extremely relevant for the study of phase transitions involving multiple coupled degrees of freedom, which are extremely difficult to disentangle in equilibrium conditions, but may exhibit distinct and separable dynamical behaviours.

Resonant quench and electronic dynamics

While phonon population dynamics is encoded in the differential variation of the Stokes and antiStokes Raman intensities, TRRS experiments may also reveal pump-induced intensity variations that affect both sides in the same way. Typically, these variations carry information about changes in the electronic properties of the system.

The component of the intensity independent of the phonon population, according to equations 2.24, is given by:

$$\frac{I_S(t)}{\left(\omega - \omega_\nu(t)\right)^3} - \frac{I_{AS}(t)}{\left(\omega + \omega_\nu(t)\right)^3} = C'\chi^2(t) \tag{3.2}$$

where it was assumed that the optical constants do not vary significantly over the considered frequency range, and can therefore be summarized in the factor $C' = C\frac{T}{2\alpha\eta}$, which is identical for the Stokes and antiStokes sides.

From this expression it is clear that any significant pump-induced variation of the optical constants will manifest as a global modulation of the Raman signal intensity through the factor $C'(t)$. However, in cases where variations of the optical constants are negligible, or can be independently determined through complementary measurements, it becomes possible to isolate the temporal dynamics of χ, *i.e.* the bilinear product of the Raman tensor with the photon polarization vectors.

This aspect is particularly interesting when Raman measurements are performed under resonant probe conditions: in such case the dynamics of χ^2 can provide direct in-

sight into the photoexcited carrier dynamics. Indeed, under resonance, the virtual state to which the probe excites the system in the first step of the Raman process coincides with a real electronic state, leading to a strong enhancement of the Raman cross section. In such conditions, the Raman tensor becomes directly proportional to the optical transition probability from the ground state to the excited electronic state:

$$\tilde{\boldsymbol{R}} \propto |\langle 0|H_{ER}|a\rangle|^2 \tag{3.3}$$

This transition probability is, in turn, inherently linked to the occupation of the electronic states $|0\rangle$ of the excited state $|a\rangle$.

Thus, if the pump induces a substantial change in the occupation of the electronic states $|0\rangle$ and $|a\rangle$, the corresponding modification of the optical transition probability directly affects the Raman intensity. This effect has been experimentally observed, for instance, in WS_2, where an above-bandgap excitation produces a ground state bleaching/excited state filling, thereby quenching the resonant condition of the probe and leading to a transient decrease of the Raman signal [34]. Under these conditions, the temporal evolution of χ^2 mirrors the one of the electronic population, thereby enabling to track the relaxation dynamics of the photoexcited electrons, holes or excitons.

3.2 Effects of a pulsed probe

In pump–probe experiments, the temporal resolution of the measurement is enabled by the use of a pulsed probe. It is therefore natural to ask whether, and in what ways, the use of a pulsed probe may influence the measurement, especially how it may differ from standard Raman measurements performed under CW excitation. From a theoretical standpoint, it has been shown that in the zero-pump limit the non-equilibrium Raman response reproduces the equilibrium one, with the only modification being the additional broadening arising from the limited frequency resolution of a pulsed probe (discussed shortly below) [26]. Experimentally, however, certain differences do appear that are worth mentioning.

First, the use of a pulsed laser makes it more difficult to operate in a perturbative regime of the probe, as well as to remain below the damage threshold of the material. The Raman signal intensity scales with the average laser power, and given the intrinsically low scattering efficiency, the average laser power is often critical in the measurements of spontaneous Raman scattering. Achieving the same average power of a CW laser with a pulsed source, however, implies reaching significantly high peak powers. This can lead both to damage effects (easily triggered by the peak maximum intensity even when the average power remains below the nominal threshold), as well as an increased perturbation of the system, such as the probe-induced modification of the phonon population discussed in the next section. To mitigate these issues, TRRS is typically performed with high repetition-rate laser sources (hundreds of kHz, MHz), which allow high average power while keeping the energy per pulse relatively low.

Two other effects of using the pulsed source, which can be clearly observed in the data reported in this thesis, are illustrated in the following.

Time and frequency resolution trade-off

From the equations derived in the previous section, it follows directly that the spontaneous Raman scattering process reflects the spectral bandwidth of the exciting field.

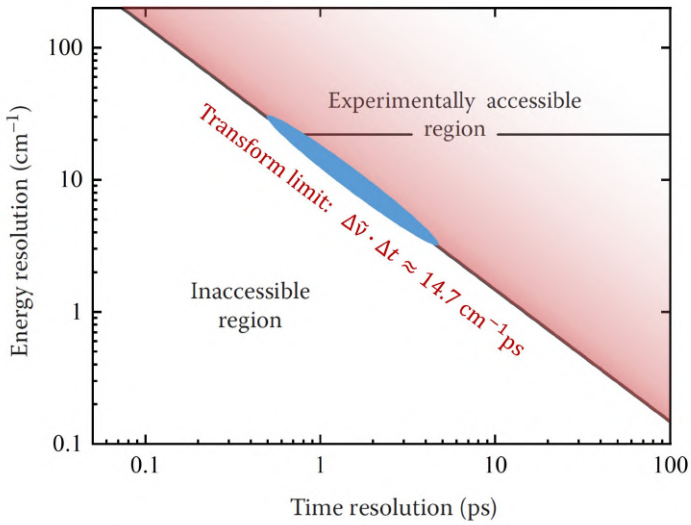

Figure 3.2: Experimentally accessible region in the time-frequency bandwidth plane. The blue oval indicates the region of interest for investigations of the phonon dynamics.

Indeed, from the conservation of energy ($\delta(\hbar\omega' - (\hbar\omega \pm \Delta E_{BA}))$ in equation 2.19 for the Stokes case), the scattered photon energy is simply rigidly shifted with respect to the incoming one. Consequently, any finite spectral broadening of the exciting laser is directly transferred to a corresponding broadening of the Raman peak.

In standard equilibrium Raman experiments employing CW radiation, it is typically possible to achieve a spectral resolution of $\sim 1\ \mathrm{cm}^{-1}$. Under these conditions, the measured linewidths of the Raman peaks are dominated by the intrinsic phonon lifetime broadening, typically ranging from sub-cm^{-1} to a few cm^{-1}.

However, as the probe duration shortens, its spectral width increases. For transform-limited Gaussian pulses, the time-bandwidth product is given by $\Delta\tilde{\nu}\cdot\Delta t \approx 14.7\ \mathrm{cm}^{-1}\cdot\mathrm{ps}$, where $\Delta\tilde{\nu}$ and Δt are the FWHM in the spectral and temporal domains, respectively. This relation imposes a fundamental constraint on the time and frequency resolution experimentally accessible by TRRS (and in general by spectroscopies based on spontaneous processes), as illustrated in figure 3.2. Since the characteristic timescale of phonon dynamics is of the order of picoseconds, laser pulses of comparable duration are required to properly probe it, thus determining a typical employed laser bandwidth of $\sim 15\ \mathrm{cm}^{-1}$. Thus, the frequency resolution in a TRRS experiment is generally limited by the bandwidth of the probe pulses.

Measured phonon population

Although, as mentioned above, probing with ultrashort pulses formally yields the same Raman cross section as a CW probe (apart from the expected increase in the peaks linewidths), experiments sometimes reveal significant discrepancies between the phonon temperatures extracted with CW and pulsed probes (see for example data on MoS_2 reported in section 6.5 of Chapter 6). In particular, pulsed probing can lead to an overestimation of the phonon population.

This effect can be interpreted as a "self-pumping" by the probe pulse itself, and it thus becomes especially relevant when the probe photon energy lies above the bandgap of the material. A simplified description of the underlying phenomenology is sketched below and illustrated in Figure 3.3.

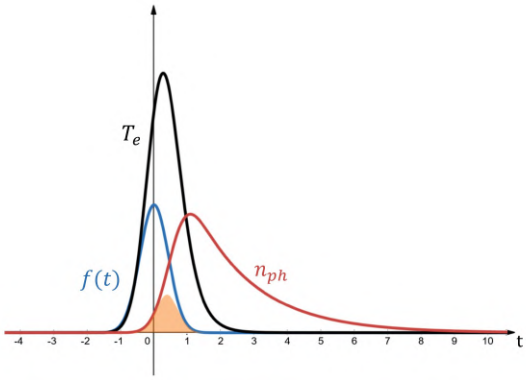

Figure 3.3: Schematic representation of a possible effect of a pulsed probe on the phonon population measurement. Blue, black and red lines represent the Gaussian temporal profile of the laser, the electronic temperature and the phonon population, respectively. An orange area evidences the area of the overlap between $n_{ph}(t)$ and the probe pulse, giving rise to the enhancement in the measured population (see text). The displayed intensities are arbitrary.

Let us consider a system probed with a laser pulse of the form $I(t) = I_0 g(t)$. While the probe impinges on the sample, the electronic temperature increases due to the fraction of the intensity which is absorbed by the system, and subsequently decays by and transferring energy into the phonon subsystem via electron–phonon coupling. Considering a Gaussian pulse $g(t) = \frac{1}{\sqrt{2\pi}\sigma} e^{-t^2/2\sigma^2}$, and assuming an instantaneous rise of electronic temperature proportional to $I(t)$ and an exponential relaxation characterized by the total electron–phonon coupling constant γ_{eph}, the time dependence of the electronic temperature increase $\Delta T_e(t)$ results to have the functional form:

$$F(t) = Ae^{-\gamma_{eph}t}\left[\text{erf}\left(\frac{t-\gamma_{eph}\sigma^2}{\sqrt{2}\sigma}\right)+1\right] \tag{3.4}$$

where A is a constant collecting all time-independent quantities.

After the strong rise, the electronic relaxation leads to an increase of the phonon population n_{ps}. For a phonon mode strongly coupled to the electrons, the temporal evolution of $n_{ph}(t)$ can be well approximated by the same functional form, delayed by a characteristic time t_0^{ph} and with γ_{eph} replaced by the phonon–phonon coupling constant γ_{phph}.

By measuring the phonon population with the same pump pulse, the obtained results would be increased by an amount:

$$n_{ph}^{mis} = \int_{-\infty}^{\infty} n_{ph}(t)g(t)dt \tag{3.5}$$

Thus, as illustrated in Figure 3.3, whenever there is a finite overlap between the probe pulse and the probe-induced phonon population increase, the measurement can capture an artificially enhanced phonon population compared to equilibrium. For a probe duration of about 1 ps, this situation can easily arise for modes strongly coupled to the electronic subsystem, where t_0^{ph} is comparable to the electron relaxation time, typically of the order of hundred femtoseconds. This effect is thus mode-dependent and may even be exploited to distinguish, even in absence of a pump, phonons modes with stronger or

weaker coupling with the electrons.

It is important to notice that this probe-induced phonon population increase occurs regardless of the presence of the pump and of the pump–probe delay. Thus, the effect of the pump on the equivalent phonon temperature can still be extracted as the difference between the values measured at positive and negative delays. However, this effects signals that the measurement is being performed on a perturbed system, in presence of an additional phonon population. To cleanly disentangle the pump-induced effects, it is therefore necessary to operate with probe powers much lower than the pump power. Finally, it should be noted that this effect depends on the energy per pulse. At fixed fluence, it can thus be mitigated by employing a laser source with higher repetition rate.

Part II

Time-Resolved Raman Spectroscopy at NFFA-SPRINT

CHAPTER 4

A UHV-compatible, time-resolved spontaneous Raman spectrometer for multi-messenger ultrafast studies

In my thesis work I completed the setup and commissioning of a new end-station for time-resolved (TR) optical and Raman spectroscopy of the NFFA-SPRINT laboratory, part of the NFFA facility at IOM-CNR in Trieste in collaboration with Elettra and FERMI. The project of the end-station is a joint effort of IOM-CNR, Università di Milano, Università di Perugia, and Sapienza Università di Roma based on the NFFA-SPRINT laser sources aimed at the research on phonon dynamics in quantum materials, and, subsequently, to integrate the NFFA research infrastructure as a user facility.

The scientific results discussed in this thesis were obtained and refined during three years of measurements that served also to improve and partially redesign the setup acquisition system. This chapter is therefore dedicated to presenting the setup, along with the characterizations and tests of its functionalities carried out during its commissioning.

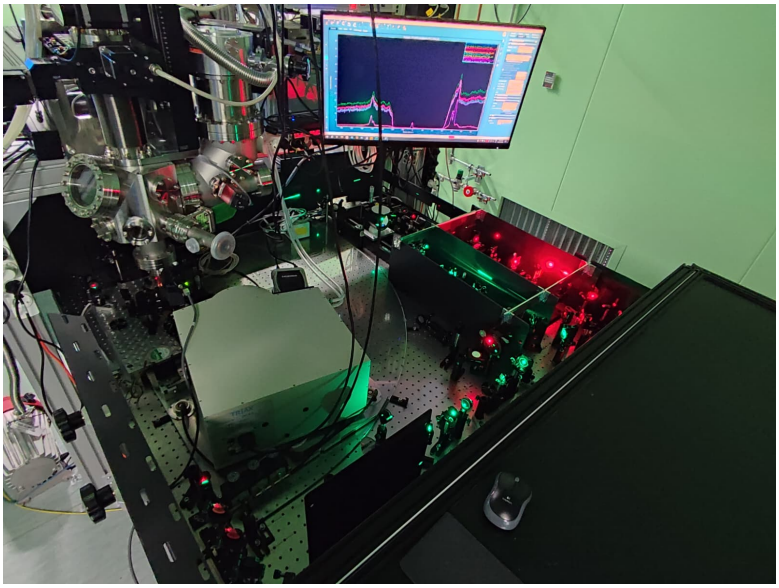

Figure 4.1: Picture of the TRRS setup.

The integration of spectroscopic methods sensitive to multiple degrees of freedom (electrons, phonons, spin-polarization) has proven to be essential to reach a consistent description of physical systems at equilibrium [35–37]. Extending this approach to time-domain, the integration of complementary time-resolved (TR) spectroscopic methods, holds the promise to deliver a complete description of dynamic processes in condensed matter [29]. In this context, the interoperability of different experimental setups is a prerequisite for exploiting multi-messenger science in quantum matter physics.

Full interoperability with the broader NFFA infrastructure (including sample growth, electron and optical spectroscopy, and both time-resolved and time integrated methods) was thus at the basis of the design of the time-resolved Raman spectroscopy (TRRS) setup. To meet this goal, the setup was designed as a ultra-high vacuum (UHV) chamber with a cryogenic manipulator and sample transfer stage where a UHV "suitcase" enables the exchange of freshly grown samples (*e.g.* in the NFFA-PLD facility), their transfer to other end-stations as the SPRINT-HHG beamline for TR-ARPES and TR-Spin Polarimetry [38], or their extraction to atmospheric conditions for in-air optical experiments (photoluminescence lifetime [39], and transient grating spectroscopy and magnetometry [40, 41]).

Moreover, with the same rationale, the setup was designed with future versatility in mind, foreseeing future extentions of its capabilities to other time-resolved optical spectroscopies, such as transient reflectivity at variable angles, and three-pulses techniques such as femtosecond-stimulated Raman scattering.

4.1 Optical scheme and characterizations

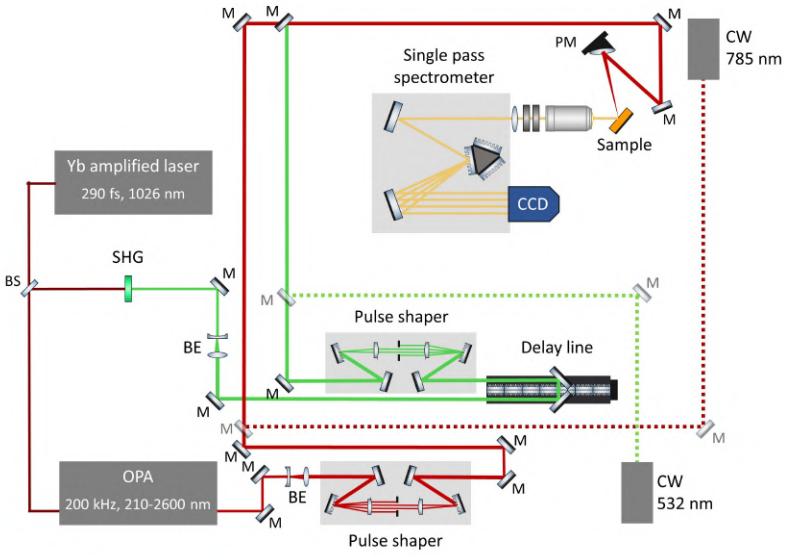

Figure 4.2: Optical scheme of the TRRS setup. In the final part of the optical path the two laser beams are vertically superimposed. Optical elements are labelled as follows. M: mirror; BS: beam splitter; BE: beam expander; SHG: BBO crystal for second harmonic generation; CW: continuous wave laser sources.

The TRRS setup is powered by the shared laser source that serves all experimental stations of the NFFA-SPRINT laboratory. It comprises two Yb:KGW-based laser amplificators (PHAROS, Light Conversion) with a common oscillator, each one emitting pulses with time duration of 290 fs at 1026 nm, variable repetition rate from single shot to 1 MHz, pulse energy of 400 µJ (at 50 kHz) and average power up to 20 W. The lasers can seed a high-harmonic generation (HHG) source dedicated to TRPES experiments, which allows access to the XUV range, and two different optical parametric amplifiers (OPA), covering the UV-visible ($\lambda = 210 - 2600$ nm) and the visible-IR ($\lambda = 640 - 2550$ nm) wavelength ranges. A pulse compressor at the output of the latter allows to reach a pulse duration between 30 and 50 fs. More details on the Pharos, and on the HHG and OPA sources are reported elsewhere [38, 42].

While in principle all available sources (except the HHG) could be exploited for TRRS experiments, in the current configuration the pump pulse is typically provided by the UV-visible OPA, which allows for a broad tunability of the photon energy. The probe is usually the second harmonic (SH) of the laser fundamental emission (1026 nm), generated through a nonlinear BBO crystal and spectrally purified using a dichroic mirror. When required, the role of pump and probe can be exchanged. The OPA operates at fixed repetition rate, which is currently set at 200 kHz. In a preliminary configuration, employed for part of the measurements reported in this thesis, the OPA required to be seeded at a 50 kHz repetition rate.

The optical scheme of the TRRS setup is shown in Figure 4.2. The pump and probe laser pulses enter the Raman setup passing through two 4f pulse shapers, enabling the fine tuning of the pulse duration-spectral bandwidth. The rationale, design, and characterization of the pulse shapers are discussed in details later in this section (see Figure **??**). The relative delay between the pulses is tuned through the use of a motorized delay line, equipped with a corner cube reflector, which allows to choose the delays in the range from -1 ns to +1 ns for each pump-probe pulse configuration. The two pulses are emitted with vertical polarization from the laser sources; for the SH, the generation process rotates the polarization to horizontal, which is restored to vertical by a half-wave plate after the corresponding pulse-shaper. Vertical polarization is maintained for most of the optical path to maximize mirror efficiency. Additional control over the pump and probe polarization is available through the use of achromatic half- and quarter-waveplates (Thorlabs Inc.), while the pulse fluences are adjusted by neutral filters with variable optical density. In the final part of the optical path (top in 4.2 (b)), the pump and probe beams are aligned on parallel axes, vertically superimposed and spaced by 6 mm, and then focused on the same spot on the sample surface by an off-axis parabolic mirror. Throughout the optical path, the OPA output is kept on a propagating axis parallel to the optical table (and coincident with the optical axes of optical elements), which defines the optical scattering plane. The focusing and signal collection geometries are detailed in the following (Figure 4.5). To enable the full in situ sample characterization by conventional Raman spectroscopy (see e.g. Figure 4.4 (b)), two continuous-wave (CW) lasers at 532 nm and 785 nm are also available; they can be aligned on the pump and probe optical paths using removable mirrors.

The inelastically scattered signal is collected by a microscope objective and delivered to a single pass Czerny-Turner spectrometer (Triax model, Horiba scientific). The spectrometer features a 320 mm focal length and is equipped with three diffraction gratings with 300, 600 and 1800 lines/mm (Horiba ruled plane gratings 510-03, 510-12, 510-19) providing a final spectral resolution between 20 and 3 cm^{-1}. A back-illuminated, deep-

depleted CCD (Synapse*Plus* Horiba) with multiple stage thermoelectric and liquid cooling system collects the signal, ensuring low noise and high sensitivity. The signal is acquired and elaborated in real time by the spectrometer company proprietary software.

Pulse shaping

Using a pulsed laser as a source in a TRRS experiment requires a fine tuning of the pulse duration-spectral bandwidth. Indeed, since the detected signal arises from a spontaneous scattering process, the spectral resolution is limited by the bandwidth of the probe pulse, which is in turn intrinsically linked to the overall time resolution of the experiment. The Fourier-transform limit $\Delta t \Delta\omega \sim 15\ \mathrm{ps} \cdot \mathrm{cm}^{-1}$ implies that a time resolution in the ps scale is needed for appreciating a 15 cm^{-1} phonon lineshape.

In our setup, as mentioned above, that is enabled by two 4f pulse shapers on the pump and probe optical paths. The design and working principle of a 4f pulse shaper is sketched in Figure 4.3 (a). The incoming beam is dispersed by a diffraction grating and each chromatic component is focused by a cylindrical lens on a plane where a suitable optical mask designs the desired pulse spectral shape. A second cylindrical lens is used to re-collimate the beam, and a second diffraction grating, mirroring the first one, recomposes the shaped beam. Our experimental realization of the 4f pulse shaper is shown in the picture in Figure 4.3 (b). In our case, a tuning of the spectral bandwidth and of its central wavelength is needed: to this aim, a slit mounted on a lateral micrometric displacement is sufficient.

The effect of pulse shaping on the bandwidth and duration of an OPA pulse at 633 nm is shown in Figure 4.4 (a). The laser shape dependence on the micrometric slit opening, measured through the Raman spectrometer after suitable attenuation, is shown in the inset. The pulse duration, measured by a commercial autocorrelator (APE pulseCheck) placed at the output of the pulse shaper, is displayed as a function of the achieved laser bandwidth. We can see that, as expected from the source characteristics, the pulses generated by the OPA are not transform-limited and we estimated from a fit $\Delta t \Delta\omega \approx 27$ $\mathrm{ps} \cdot \mathrm{cm}^{-1}$. This value showed minimal variation across different slit openings, and even for pulses bypassing the pulse shaper entirely, indicating that the pulse shaper does not significantly affect the time–bandwidth product in our setup. In all the reported experiments the OPA pulse duration is therefore estimated from the measured laser linewidth using the time-bandwidth product extracted from the fit. The data from the pulse shaper characterization also show how it is possible to remove part of the tails in the laser spectrum without affecting the temporal resolution. This is particularly useful, as often those tails are outside the spectral window of attenuation of standard notch/edge filters and lead to strong scattering overcoming the Raman signal.

In Figure 4.4 (b), we show the Raman spectra of an ethanol sample in the CH stretching region [43] as a function of the pulse shaper slit opening. We observe that, when the pulse shaper slit is opened to 30 $\mu\mathrm{m}$ (45 cm^{-1} spectral width), the three peaks in the sample spectrum appear almost completely merged into a single feature; thus a narrow slit opening, and consequently a longer pulse duration, is required to properly resolve the three features. The spectral shape measured with the pulsed laser at 20 $\mu\mathrm{m}$ (30 cm^{-1} spectral width), or lower slit opening, indeed resembles the spectrum obtained by CW laser excitation, approaching the intrinsic lineshape of the bands.

The optimization of the pulse shaper width is a crucial step in every TRRS experiment. For the probe beam, the trade-off between spectral and temporal resolution de-

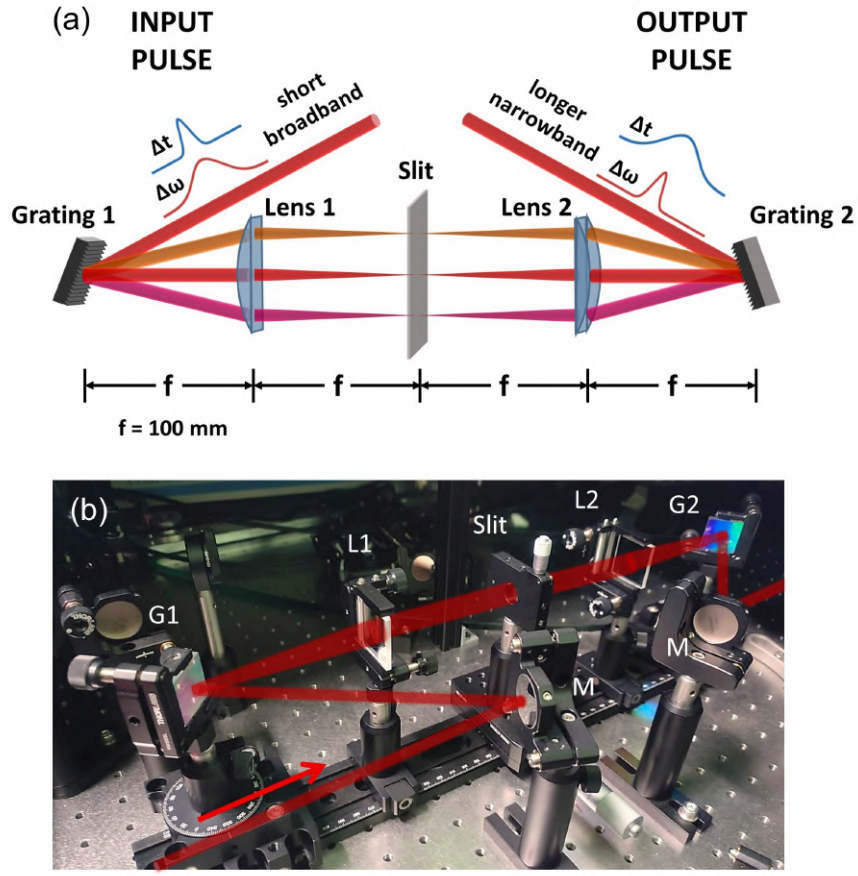

Figure 4.3: Design of the 4f pulse shapers. (a) Sketch of a 4f pulse shaper and its working principle. (b) Picture of our experimental realization. An arrow indicate the beam propagation direction. (M: Mirror; G: Grating; L: Lens)

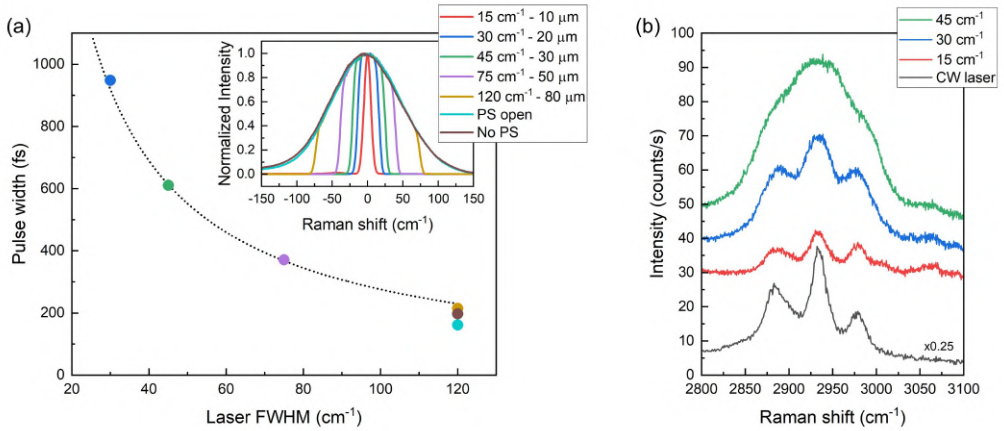

Figure 4.4: Effect of pulse shaping on pulse duration and TRRS spectral resolution. (a) Measured pulse duration as a function of the pulse bandwidth for the 633 nm emission of the OPA; inset: corresponding measured pulse spectra and slit opening values. The intensity of the 15 cm^{-1}-wide pulse was too low for it to be measured by the autocorrelator. A dashed line marks the result of the fitting with a law $\Delta t = C/\Delta\tilde{\nu}$ (b) Raman spectra of ethanol in the high frequency CH stretching region at varying pulse bandwidth ($\lambda_{exc} = 633$ nm) compared to the spectrum acquired under CW excitation ($\lambda_{exc} = 785$ nm).

pends strongly on the system under investigation. When multiple closely spaced modes are present, such as in ethanol, a narrower bandwidth becomes essential to resolve the individual peaks and disentangle the different modes behaviour under photoexcitation. Conversely, if an isolated phonon is probed, achieving a good spectral resolution may be less important, and a broader slit can be chosen to maximize temporal resolution. Even on the pump side, the pulse shaper parameters can play a significant role, since pulses of different duration but equal fluence may drive different excitation processes.

The pulse shaper is therefore a crucial element of the TRRS setup, strongly affecting the overall quality of the measurements. Inevitably, a significant fraction of the laser intensity is lost when narrowing the laser spectrum: in ideal conditions, the Gaussian spectral profile of the laser implies that reducing the bandwidth from 120 cm^{-1} to 15 cm^{-1} reduces the transmitted power to only about 12.5% of its initial value. In practice, the overall efficiency is further lowered by the non-ideal performance of the gratings and by alignment constraints. Because of both its inherently low efficiency and its optical working principles, the proper alignment of the pulse shaper optical elements is particularly critical. Even small misalignments can indeed lead to an inaccurate cut by the micrometric slit, reducing the laser intensity without effectively narrowing its spectral profile, or can alter the recomposed beam divergence and introduce significant optical aberrations in the focused spots. To mitigate these issues, several improvements were implemented during the commissioning of the setup. Beam expanders were inserted before the pulse shapers to enlarge the illuminated area on the gratings and on the cylindrical lenses, thereby increasing efficiency and reducing sensitivity to small misalignments. The five optical elements of the pulse shaper were mounted on a translation rail (see Figure 4.3 (b)), ensuring stable collinearity and facilitating alignment procedures. The gratings themselves were mounted on rotating stages, allowing a straightforward align-

ment of the pulse shaper on the zero-order diffracted beam. Altogether, these measures significantly improved the long-term stability of the setup and its ease of operation.

Beyond controlling the bandwidth, the pulse shaper also enables fine tuning of the laser central frequency within its original spectral profile. This capability is particularly useful when probing Raman modes close to the frequency cutoffs of the notch or edge filters. Moreover, although the tunability is limited by the efficiency of the available commercial gratings, the operating wavelength of the pulse shaper can be conveniently adjusted simply by rotating the gratings, which is especially useful when using the tunable OPA source.

Excitation and collection geometry

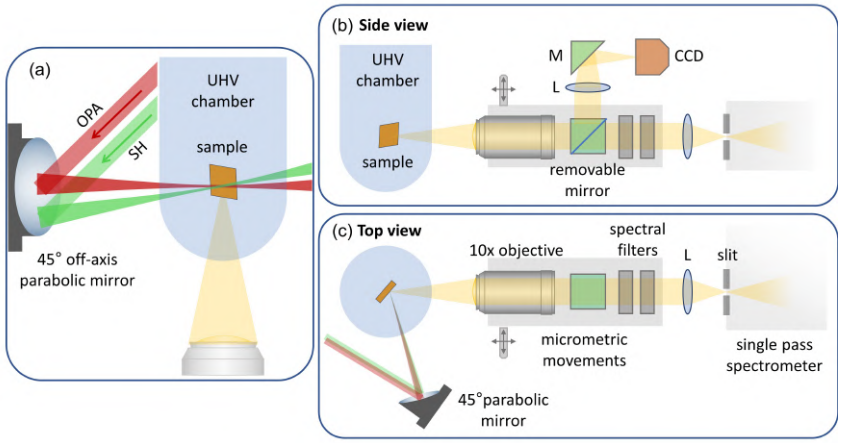

Figure 4.5: Scheme of the excitation geometry (a) and the collection geometry from the side (b) and top (c) view. (L: lens, M: mirror, SH: second harmonics).

In Figure 4.5, we show the sample excitation and signal collection geometry. To maintain it in a vacuum environment (see section 4.2), the sample is inside a UHV chamber whose lower part is constituted by a cylindrical pyrex glass allowing for pan-optical access. A $45°$ off-axis parabolic mirror (50.8 mm focal length) provides both the focusing and the spatial overlap of the pump and probe beams on the sample surface. The output of the OPA (red in Figures 4.2 and 4.5) is focused while remaining aligned parallel to the optical table, while the SH of the PHAROS laser (green in Figures 4.2 and 4.5), aligned on a parallel to the OPA output and 6 mm below, crosses the horizontal direction in the focus. When used as a probe, the incidence of the SH at a finite angle with respect to the optical scattering plane helps to spatially separate the elastic scattering from the collection optics axis. The exclusive use of reflective optics for the focusing and spatial overlap of the beams ensures achromaticity across the entire spectral range available from the lasers sources.

In order to minimize astigmatic aberrations, the focus of the parabolic mirror (i.e. the nominal position where the two beams are both focused and overlapped) is aligned on the rotational center of the pyrex cylinder. This is achieved by first determining the

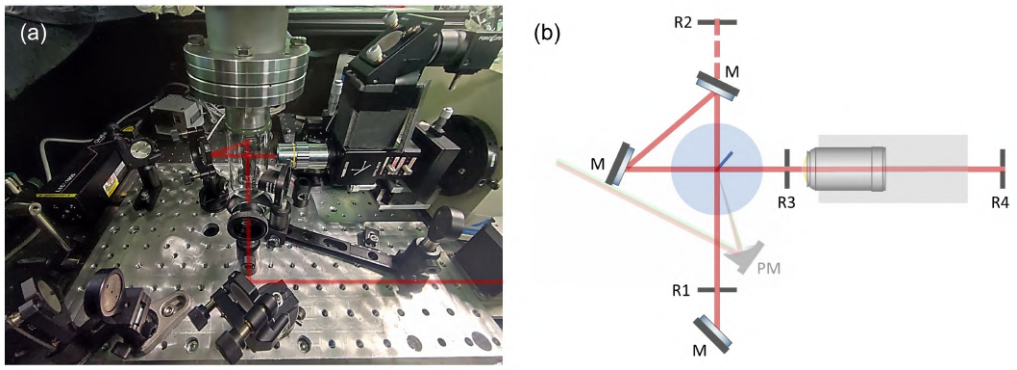

Figure 4.6: Determination of the rotational center of the pyrex glass. (a) Picture and (b) scheme of the excitation and collection optics in the configuration with additional alignment mirrors (M). Red lines show the laser optical path in the alignment configuration, crossing itself in the rotational center of the pyrex cylinder. R1-R4 represent alignment references based on the setup geometry; R4 is the spectrometer entrance slit. The parabolic mirror (PM) and the excitation direction are shown in light colours.

cylinder center at the height of the OPA optical path using additional alignment mirrors, as shown in Figure 4.6. These mirrors are aligned on references on the optical table defining two axis according to the setup geometry, and allow the beam to intersect with itself precisely at the rotation axis. By monitoring the scattering using the available imaging system (described below), the edge of a transparent reference sample can be positioned at the beam intersection point. Finally, the alignment mirrors are removed and the parabolic mirror is finely adjusted to ensure that both beams are precisely focused and overlapped at this location.

The translational movements of the manipulator (see section 4.2) then allow the sample to be positioned in the focal point. A 10x long working distance objective (Mitutoyo Plan Apochromat Objective, 0.28 NA, 34 mm WD), aligned along a radius of the pyrex glass cylinder, collimates the scattered radiation, which is then focalized on the entrance slit of the spectrometer. The focusing lens is properly matched to the spectrometer numerical aperture, ensuring optimal light collection efficieny and spectral resolution. Unlike in conventional backscattering geometries, the non-coaxial design, with different optics for sample excitation and signal collection, allows for an independent regulation of the incident fluence and the collection numerical aperture. Two filter holders after the microscope objective host interchangeable notch/edge filters to remove the elastically scattered component of both the pump and probe beams. The optical imaging of the sample is enabled by a removable mirror which can be inserted after the microscope objective, focusing the scattered radiation on a CCD camera when the sample is illuminated by an external source. The collection and imaging optics are mounted on micrometric movements allowing for a precise alignment of the objective and thus signal optimization.

The CCD field of view was calibrated using a TEM grid with a known pitch as a reference. As shown in Figure 4.7 (a), intensity profiles were extracted from the captured images, and the measured pixel spacing between the peaks corresponding to the grid lines was compared to the known grid spacing in micrometers. This calibration also al-

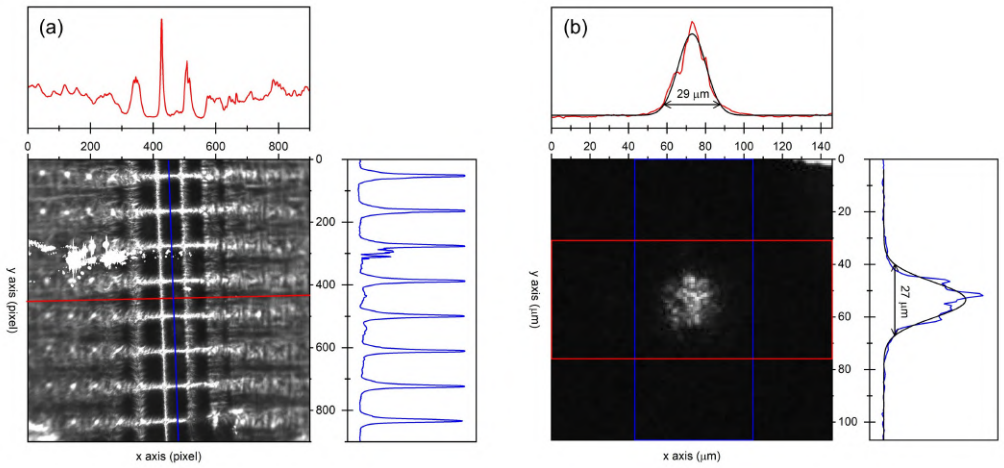

Figure 4.7: (a) Spatial calibration of the imaging CCD on a TEM grid. Top and right panels shown the intensity profiles along the red and blue lines reported in the image. The spacing between the peaks was used for calibration. The image being at focus only in the central parts depends on the measurement angle between the sample surface and the collection optics axis. **(b) Laser spot size measurement** shown for the SH of the Pharos. Top and right panels shown the integrated intensity between the red and blue lines reported in the image. Continuous lines show the result of fitting with Gaussian profiles, from which the reported $1/e^2$ values are obtained.

lows the measurement of the laser spot size on the sample (essential for calculating the laser fluence) from the properly imaged diffusive scattering, as shown in Figure 4.7 (b). Gaussian fits of the integrated intensity profiles have thus shown that the described geometry produces laser spots diameters of 25-30 μm ($1/e^2$). Such estimate is corroborated by the measurement of laser traces left on photosensitive sample surfaces. It should be noted that the spot size can undergo small variations depending on the specific alignment of the lasers on the optical path; therefore, it is good practice to measure it at the beginning of any measurement campaign, either directly on the sample or, if the diffusive scattering is too weak, on the sample holder.

It is worth noting that even small misalignments before the parabolic mirror can move the focal positions of the two beams, potentially resulting in the loss of the spatial overlap. Since these variations are generally small and do not move the foci significantly away from the rotational center of the pyrex cylinder, it is not necessary to realign the parabolic mirror at the beginning of every measurement session. Instead, the following procedure is adopted: first the best focusing condition (*i.e.* minimal spot size) is found adjusting the sample distance from the parabolic mirror with the manipulator, then the spatial overlap of the two beams is optimized by fine tuning two independent steering mirrors.

This procedure, as well as the proper positioning of the sample at the focal point, becomes more challenging when measurements are performed in vacuum inside the pyrex cylinder. Optical aberrations caused by the curvature of the glass indeed distort both the sample image and the diffuse scattering pattern generated by the laser beams. However, the correct positioning of the sample at the point of minimum spot size can still be verified by monitoring the Raman scattering signal and finding the distance between

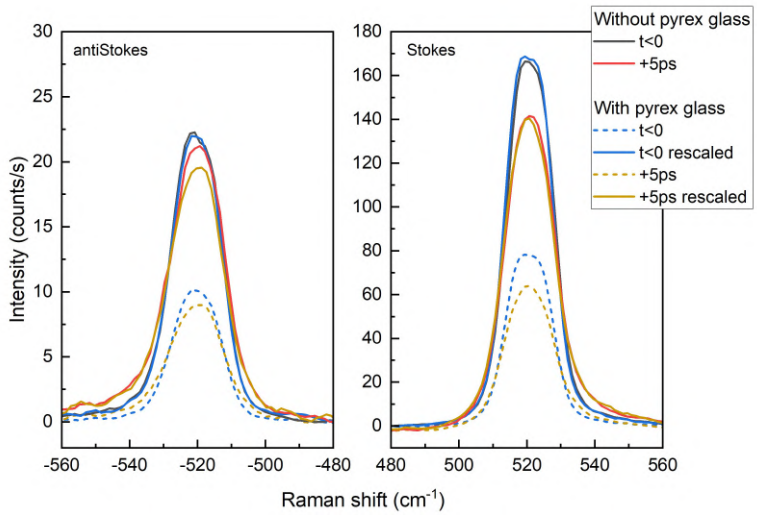

Figure 4.8: Comparison of TRRS measurements on silicon with and without the pyrex glass. The antiStokes and Stokes sides of the Raman spectra of Si (measured with 513 nm probe and 633 nm pump pulses) are shown before the pump-probe coincidence time and at $t = +5$ ps. Black and red continuous lines mark the spectra obtained without the pyrex glass. Blue and yellow lines mark the spectra obtained with the pyrex glass: spectra as acquired are shown as dashed lines, while continuous lines show the same spectra rescaled by a factor 2.15. At both delays the latter are in good correspondence with the spectra obtained without the glass.

the sample and the parabolic mirror that maximizes it. The spatial overlap with the pump beam can then be checked by measuring the magnitude of the pump-induced effect on a reference sample with a known behaviour (e.g., silicon).

The comparison between TRRS measurements on a reference sample carried out with and without the pyrex cylinder also allowed us to verify that the achieved spot size is not significantly affected by the presence of the glass. Figure 4.8 illustrates this comparison for pump–probe measurements on silicon. Although the absolute signal measured from the sample is reduced when the pyrex cylinder is present, the relative effect of the pump remains unchanged. This demonstrates that the sample is excited with comparable fluence in both cases, indicating that the beam spot sizes do not undergo significant variations and the reduction of the overall signal can be attributed primarily to a lower collection efficiency.

4.2 Sample environment

The sample environment is a key originality of the present setup, offering fine control over spatial alignment, temperature, the preservation of sample cleanliness and stability, and the possibility of exchanging samples in UHV with other spectrometers and sample growth systems. The sample is mounted on the cold finger of a cryostat (see below) attached to a motorized UHV manipulator (PMM 12, VAB Vakuum-Anlagenbau GmbH) providing four degrees of freedom: three orthogonal linear translations (X, Y, Z) with a minimum step size of 1 μm, and a full 360° rotation about the manipulator axis (vertical). This enables precise spatial alignment of the sample relative to the excitation and

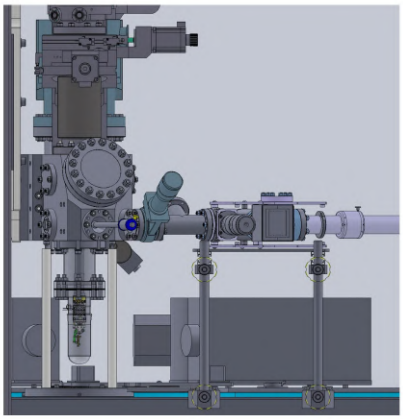

Figure 4.9: CAD model of the UHV chamber and manipulator. On the right side, the UHV suitcase is shown attached in the transfer position.

collection optics, as well as the control over the laser incidence angle, critical for applications such as polarization-dependent Raman measurements. The manipulator can be operated via either joystick or software, with a coarse manual control (10 μm step size) also available for linear translations.

The sample holder is hosted by a UHV chamber, with a pumping system which allows to reach a pressure of 10^{-8} mbar. The chamber is fully bakeable, if actual UHV pressure (10^{-10} mbar) is needed. A UHV-compatible transfer system (Ferrovac UHV suitcase) enables the introduction and removal of samples without breaking vacuum conditions. A CAD model of the chamber and manipulator is shown in Figure 4.9. While Raman spectroscopy can be performed under ambient conditions, the presence of a vacuum environment significantly broadens the experimental capabilities of the current setup. Operating under vacuum: (i) ensures minimal sample contamination during measurements, thereby enabling the investigation of air-sensitive materials and systems whose properties are strongly influenced by surface conditions; and (ii) allows, together with the integrated cryostat, measurements at cryogenic temperatures, essential for most studies involving phase transitions and strongly correlated materials. Moreover, the UHV conditions, combined with the UHV transfer system, ensure full compatibility with the electronic spectroscopy setups available in the SPRINT laboratory and in other laboratory of the NFFA facility (e.g. the APE beamlines of the Elettra Synchrotron, MIMAG laboratory at University of Milano). This integration enables a true multi-messenger approach, allowing experimental campaigns to be conducted under reproducible environmental conditions, from sample growth to measurements using multiple complementary techniques.

Vibration issues

The UHV chamber is suspended on an aluminium H-shaped bridge, mechanically isolated from the optical table. During commissioning, we observed that this geometry leads to a transmission of random mechanical vibrations of the bridge and to the manipulator and the cold finger of the cryostat, on which the sample is mounted.

The vibration spectrum of the system, measured using a ceramic shear accelerometer (Piezotronics, model 393B12) at the laboratory floor, on the optical table, and on top of the UHV chamber, is reported in Figure 4.10 (a). The data show that the spectrum mea-

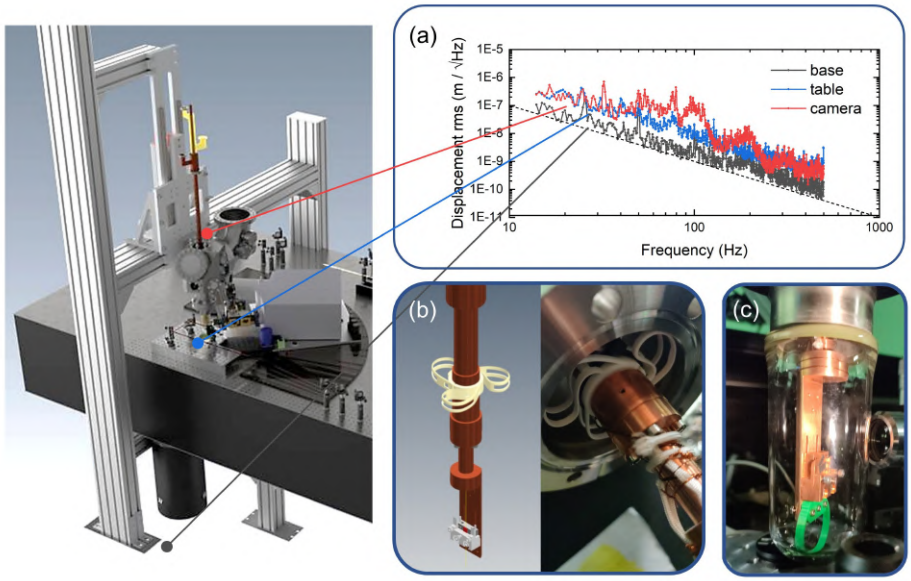

Figure 4.10: Characterization of mechanical vibrations and adopted solutions. (a) Vibrational spectrum measured at the base of the optical table (black), on the optical table (blue) and on top of the UHV chamber (red). A dashed line marks the lower measurement limit. (b) Project and realization of the polymer damper positioned on the metal rod of the cryostat, providing mechanical contact with the UHV chamber. (c) Additional damper for mechanical stabilization when measuring at cryogenic conditions close to the nitrogen boiling point.

sured on top of the chamber is structured around 100 Hz with peaks approaching 1 μm rms, differently to the one of the floor (at the sensitivity limit of the instrument) and of the optical table. Owing to the length of the cryostat rod (over 70 cm), these chamber vibrations can easily result in oscillations exceeding 10 μm at the sample position, as visually estimated from the imaging (direct accelerometer measurements at the sample position are not possible due to the physical dimension of the instrument). The independent vibrations of the sample and the collection optics, mounted on the optical table, degrade the quality of the collected signal.

Because the primary source of vibrations (likely the coupling of the H-bridge surface to turbulence from the laboratory cooling air flow) could not be eliminated, stabilization was achieved by implementing a local damper close to the sample position. As shown in Figure 4.10 (b), the damper, 3D-printed in ABS polymer, creates a contact between the cryostat rod and the walls of the vacuum chamber, effectively reducing oscillations to a level no longer detectable in the imaging.

Cryostat system

The system includes a UHV compatible continuous flow cryostat system (Lake Shore Cryotronics ST-400), capable of operating with both liquid nitrogen and liquid helium. Thermal contact between the sample holder and the cold finger of the cryostat is ensured by two clamping screws. Temperature monitoring and control is achieved via two DT-470 silicon diode sensors: one located inside the cryostat and the other mounted

in vacuum on the cold finger, on the backside of the sample. The second sensor provides the actual temperature on the sample via a properly calibrated correction factor. The locations of the two sensors, as well as the positioning of an additional sensor enabling the measurement of the correction factor, are shown in the picture of the cryostat cold finger in Figure 4.11 (a). The sensors are connected to a Lakeshore 336 temperature controller, enabling continuous monitoring and data logging as well as Proportional Integral-Derivative temperature control with a precision of 0.1 K. Temperature control and stabilization is achieved by the use of a resistive heater positioned inside the cryostat, which also allows to carry out measurements above room temperature (up to 500 K nominal heating power, tested up to 350 K).

As part of the commissioning of the TRRS setup, the cryostat operation was tested under liquid nitrogen flow. The system can stably reach temperatures as low as 77 K. However, we observed that operating too closely the nitrogen boiling point introduces random mechanical vibrations on the manipulator, due to the rapid expansion of nitrogen in the cryostat heat exchanger. Similarly to the vibrations originating from the suspension bridge of the chamber, these fluctuations propagate to the sample position, producing wide oscillations (10–20 μm) that change the measurement position and degrade the quality of the collected signal. To mitigate this issue, a second local damper was added and fixed to the cryostat head (see Figure 4.10 (c)), stabilizing the position of the cryostat cold finger by providing contact with the pyrex glass. With this solution, stable measurement conditions are typically achievable for temperatures above $\sim$ 80 K. In the temperature range near this limit, the mechanical and thermal stability of the cryostat can be further improved by pumping the nitrogen after its passage through the cryostat, thereby reducing pressure fluctuations and ensuring a steadier flow. Further progress can be made in the development of solutions to suppress the mechanical vibrations. For example, a systematic study of the optimal damper shapes and materials, with a focus on the stiffness at low temperatures, could improve the performances. Moreover, a more advanced solution based on the measurement of the sample position with interferometric techniques and the implementation of an active position feedback via software is under study.

The performance of the cryostat was first benchmarked on a silicon sample, confirming the reliability of the system. Figure 4.11 (b) reports the antiStokes and Stokes regions of the Raman spectrum of Si, measured at different temperatures under CW excitation. Spectra are normalized to the Stokes peak area. The characteristic effects of decreasing temperature, namely the blue-shift of the phonon frequency and the reduction of the antiStokes intensity, are clearly observed. The antiStokes/Stokes intensity ratio extracted from the spectra is shown in panel (c) as a function of the measured sample temperature, exhibiting a good agreement with the expected behaviour of the phonon population according to Bose-Einstein distribution ($\frac{I_{AS}}{I_S} \approx e^{-\frac{\hbar\omega_\nu}{k_B T}}$) and providing an independent validation of the temperature calibration. This is particularly important in the context of Raman experiments employing a pulsed probe laser, where the equivalent temperature of a specific phonon mode can deviate significantly from equilibrium values obtained with a CW source. In these cases, thus, the observed discrepancies can be attributed to non-equilibrium effects induced by the pulsed excitation, rather than to temperature calibration errors or excessive sample heating. We note that the availability of CW sources enables direct comparison between pump–probe and equilibrium measurements, allowing such effects to be promptly identified in each experiment.

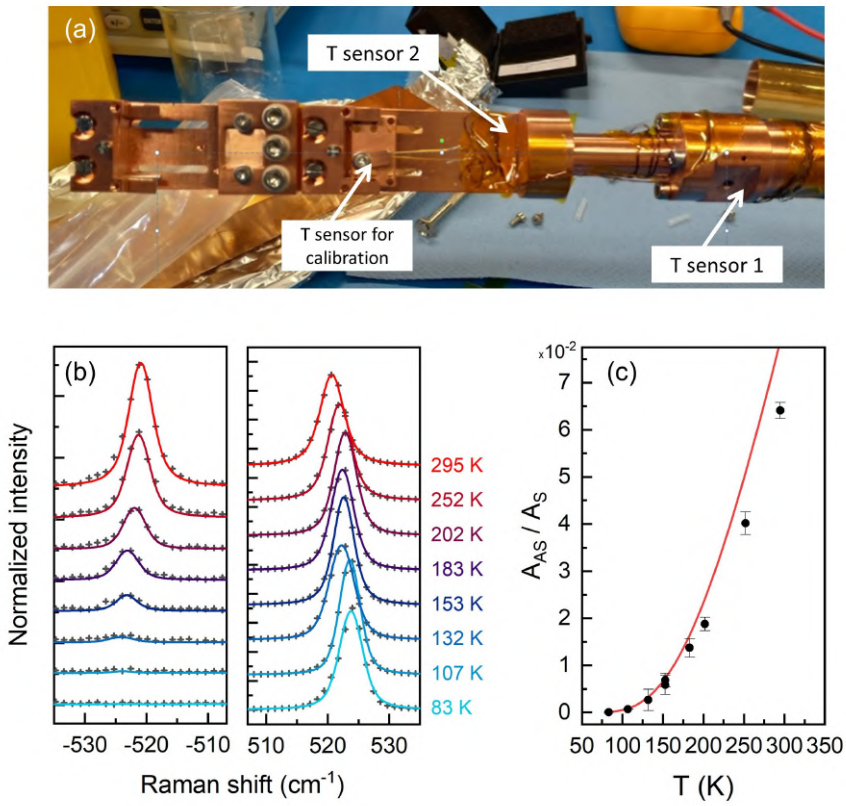

Figure 4.11: Calibration and test of the cryostat system. (a) Picture of the cryostat cold finger during the temperature sensor calibration. The two sensors available for temperature monitoring are indicated as T sensor 1 and 2. An additional sensor is mounted on a sample holder, allowing for the calibration of T sensor 2. (b) Results of test measurements on silicon at different temperatures with a 532 nm CW probe. The intensities of the spectra are normalized to the Stokes peak area. Continuous lines mark the results of fittings with Voigt line profiles. (c) Measured antiStokes/Stokes intensity ratio as a function of the measured sample temperature (on calibrated sensor 2). A continuous red line marks the expected behaviour according to Bose-Einstein distribution function.

By contrast, the operation of the cryostat with liquid helium flow has not yet been tested in the TRRS chamber. Nonetheless, the cryostat itself was previously operated with liquid helium in a dedicated test chamber, demonstrating the capability of reaching temperatures as low as 10 K at the sample stage. Some differences in thermal load in the actual measurement chamber may however affect the cryostat performance and the minimum achievable temperature; these aspects will be assessed in future planned tests.

4.3 Perspective developments

While the present TR Raman spectroscopy setup enables a detailed investigation of ultrafast vibrational dynamics, further developments are planned, aiming to extend its tunability and to allow the integration of additional optical spectroscopy techniques within the same experimental framework. Planned developments will focus on implementing a rotating collection optics module, as enabled by the cylindrical geometry of the pyrex glass allowing for optical access. The microscope objective, filters and imaging optics will be mounted on a rotating platform attached to a ball bearing on the lower flange of the UHV chamber, as shown in Figure 4.12. With the spectrometer fiber-coupled to the collection optics, this design will allow for continuous variation of the collection angle.

This is a disruptive upgrade with respect to the original design where the full spectrometer is sitting on a glass plate and could rotate on pressurized gas bearings in order to explore the pan-optical degree of freedom. The overall stability of alignment is nevertheless critical when moving relevant masses in the current design and the fiber collection solution with limited rotating mass appears definitely preferable.

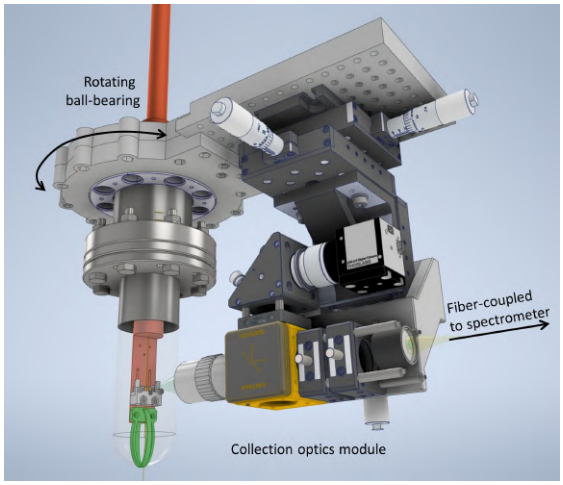

Figure 4.12: Project of the setup configuration for measurement at variable collection angle. The collection optics module are mounted on a platform attached to a ball bearing on the lower flange of the UHV chamber, enabling their rotation around the sample, as indicated.

By removing the constraint of a fixed angle between excitation and detection directions, this upgraded setup will further enhance the possibility of exploring the Raman scattering cross section rules varying independently light polarization direction, as well as incidence and scattering angle (determining the transferred momentum). More importantly, this development will also enable angle-resolved TR reflectivity measurements to be performed within the same apparatus. The combination of collection optics rotation and manipulator rotation will allow for continuous adjustment of the incidence angle from nearly normal (limited only by the lateral dimensions of the parabolic mirror and the microscope objective) to grazing. The present setup is particularly well suited for this extension, owing to (i) the wide tunability of the OPA sources from the UV to IR range and (ii) the vacuum sample environment, preserving surface cleanliness. The latter feature, in particular, will ensure the accuracy and reproducibility of reflectivity measurements, highly sensitive to surface contamination. Such enhancement will significantly broaden the capabilities of the setup, enabling simultaneous investigation of electronic and lattice dynamics with improved geometrical flexibility.

Part III

Case studies

CHAPTER 5

Anharmonic interaction and dynamical Fano resonance in Silicon

This chapter is dedicated to the presentation of the results of a TRRS investigation carried out on silicon, a structurally simple, prototypical semiconductor system that served as the first case study of our newly developed experimental setup. Focusing on the longitudinal optical phonon, we show that TRRS is not only able to track the after pump time evolution of its population, but also to reveal the photoinduced changes of the electronic states as reflected in the phonon lineshape. Moreover, by changing the optical pump fluence and the sample temperature, we highlight the influence of the excitation density on the anharmonic relaxation governing non-equilibrium phonon dynamics.

5.1 Overview

Silicon is one of the most extensively studied materials and plays a central role in semiconductor technology. Despite its widespread interest, only few studies are available on Si out-of-equilibrium phonon dynamics and even fewer employing TRRS. The Si optical and electronic properties are determined by its indirect bandgap of 1.12 eV, corresponding to transitions from the valence band maximum (VBM) located at the Γ point of the Brillouin Zone (BZ) to the conduction band minimum (CBM) at the X point, as shown in Figure 5.1 (a). The direct bandgap is instead of much higher energy (3.4 eV). The phonon spectrum of Si reflects the symmetry of its diamond lattice, resulting in a particularly simple phonon band structure (see Figure 5.1 (c)). First-order Raman scattering produces a single prominent peak at 520 cm^{-1}, corresponding to the excitation of zone-centre optical phonons, while weaker features arise from second-order processes involving phonons at other points of the Brillouin zone. Since the optical mode at Γ is triply degenerate, depending on the scattering geometry the peak can be associated with the longitudinal optical (LO) phonon or with each one of the two transverse optical (TO) phonons [22].

One of the main goals of the research on semiconductive materials is the ultimate understanding and the possibility to tailor the electric and optical properties of the materials. It goes without saying, that achieving this requires a thorough understanding of the electrons/holes de-excitation pathways, which in turn depend strongly on the coupling with the phonon subsystem, the primary reservoir with which the free carriers exchange energy. In this sense, semiconductors are a primary and immediate class of materials to be studied by TRRS, which allows direct tracking of phonon populations following photoexcitation and, in many cases, indirect insight into carrier dynamics via fine analysis of the phonon spectra.

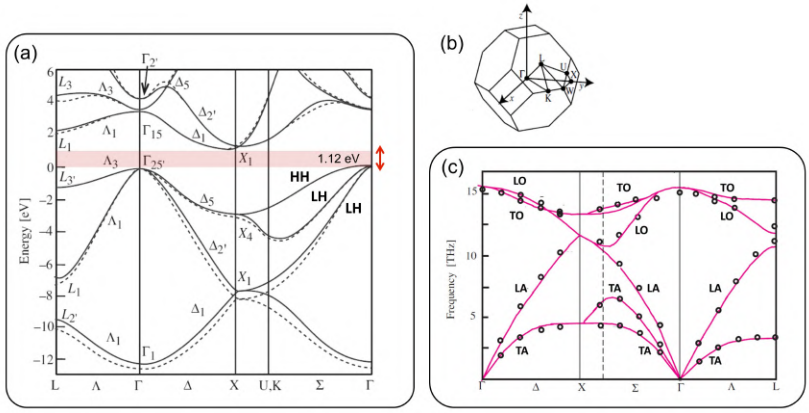

Figure 5.1: Structural and electronic properties of Si. (a) Calculated electronic band structure along the high symmetry directions. The indirect band gap is highlighted. The heavy-holes (HH) and light-holes (LH) valence bands are marked near the Γ point. (b) First BZ for the Si lattice, displaying the high-symmetry points position in reciprocal space. (c) Calculated phononic band structure along the high symmetry directions. Experimental data points are displayed on top of the calculated bands. Plots are adapted from [22].

Silicon, in particular, offers a paradigmatic case for such studies: its simple phonon band structure makes it ideal to explore lattice dynamics and phonon-phonon relaxation processes, and its electronic properties give rise to a density of excited carriers with lifetime of the order of ns, therefore essentially constant at the ps timescale, allowing the interplay between the electronic and phononic subsystems to be conveniently studied by TRRS.

For these reasons, and given the availability of a previous TRRS study by Zhu et al. [44], we selected silicon as the first test case for the newly developed setup, with the dual goal of reproducing the known observations and extending the investigation to different fluences and temperatures. Indeed, measuring the combined influence of fluence and temperature provides valuable information to understand non-equilibrium dynamics and the underlying microscopic mechanisms governing it.

5.2 Experimental

In order to investigate the effects of a transient photodoping on Si and their dependence on the external temperature and on the exciting fluence, four TRRS experiments were conducted in similar conditions. Pump pulses of 633 nm central wavelength were used to excite above bandgap an intrinsic (100) oriented Si wafer. Two pump fluences were explored: $F^{L}_{pump} = 4.9\ \mathrm{mJ/cm^2}$ and $F^{H}_{pump} = 9.8\ \mathrm{mJ/cm^2}$ (to which I will refer in the following as "low fluence" and "high fluence" respectively), corresponding to a photoexcited carrier density of $n_L = 8 \cdot 10^{18}\ \mathrm{cm^{-3}}$ and $n_H = 1.6 \cdot 10^{19}\ \mathrm{cm^{-3}}$ for the two cases. The carrier density values were estimated from the optical absorption coefficients reported in literature [45]. A small difference in the pump pulse duration was also present between the two sets of measurements, with the low fluence data being obtained with a 0.6 ps pump duration and the high fluence ones with 0.3 ps. The Raman signal was probed with 513 nm pulses of 15 $\mathrm{cm^{-1}}$ bandwidth (FWHM) and 1 ps duration, yielding

an overall temporal resolution of 1.2 and 1.1 ps for the low and high fluence datasets respectively. The probe laser was polarized along the (001) direction and the scattered radiation was collected with no polarization selection. The probe fluence used in the two cases was the same, namely $F_{probe} = 1.6\ \mathrm{mJ/cm^2}$. The experiment was carried out both at room temperature and at cryogenic temperature of ~ 85 K (precisely at 83 K for the low fluence dataset and 87 K for the high fluence one).

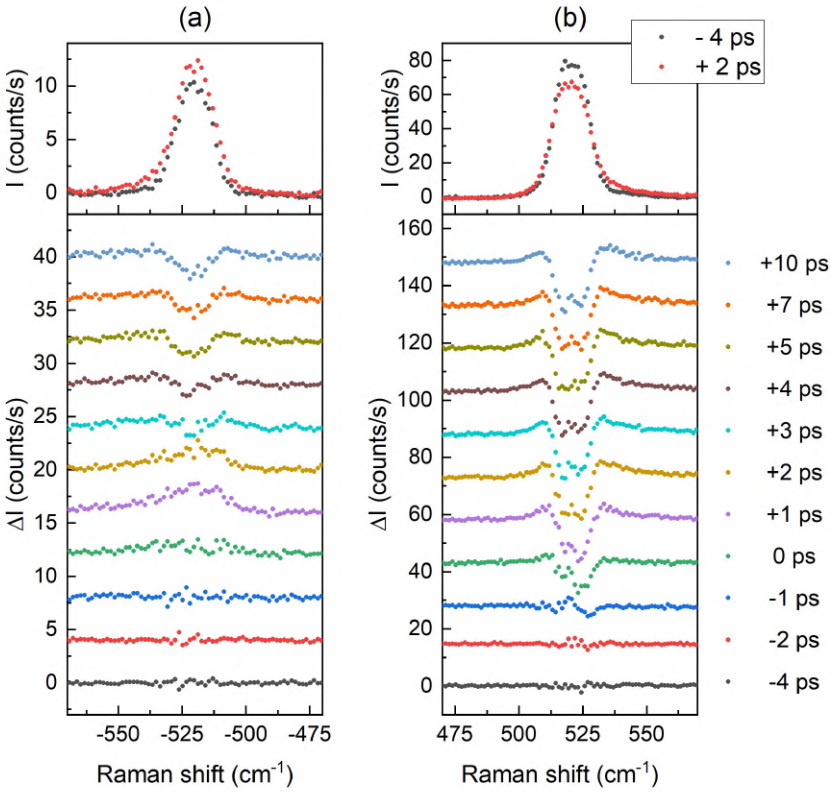

Figure 5.2: Photoinduced evolution of the Raman spectrum of Si for (a) antiStokes and (b) Stokes scattering, at room temperature in the high fluence regime ($n_H = 1.6{\cdot}10^{19}$). A negative (black data, $\Delta t = -4$ ps) and a positive pump probe delay (red data, $\Delta t = +2$ ps) are shown in the top panels. Bottom panels show difference spectra obtained subtracting the average of spectra collected at negative pump-probe delays ($t < -1.5$ ps) from the spectra recorded at positive delays.

Stokes and antiStokes spectra measured at two different pump-probe delays are displayed in Figure 5.2 (top panels), showing the peak corresponding to the zone-centre optical phonon at 520.7 $\mathrm{cm^{-1}}$. Given the excitation geometry, with most of the transferred momentum along the (100) direction (see Figure 4.5 in Chapter 4), the peak is associated mainly with the LO phonon. The reported data are obtained at room temperature in the high fluence regime. Bottom panels of the same figure show the difference spectra obtained subtracting the average of spectra collected at negative pump-probe delays (between -5 and -1.5 ps) from the spectra recorded at positive delays. From the reported data, the main pump-induced variations of the Raman signal appear to be: a transient increase in the antiStokes scattering intensity, followed by a decrease for $t \gtrsim 3$

ps, a long-lived decrease of the Stokes intensity, and a modification of the phonon profile towards a broader and asymmetric lineshape. As detailed in the following, the first effect is associated with the creation of an additional phonon population, while the others are a direct consequence of changes in the electronic state occupancies.

5.3 Dynamical Fano interference

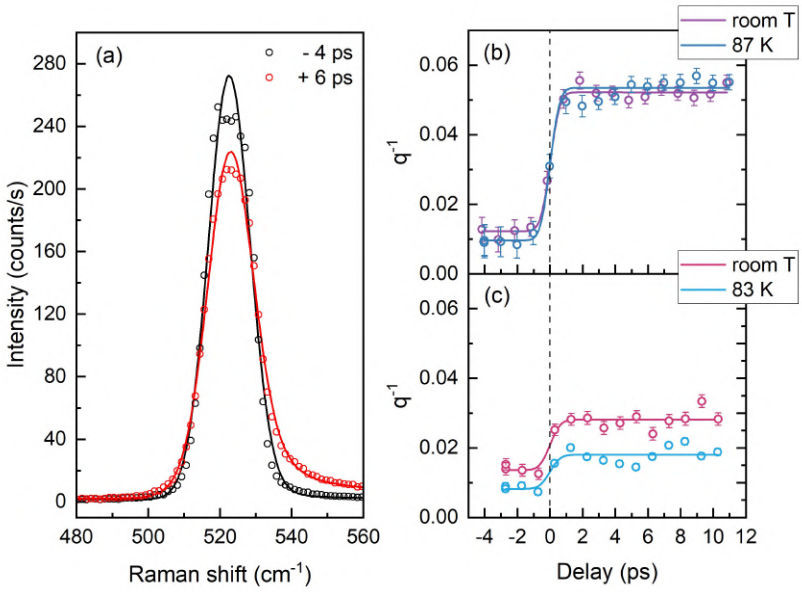

Figure 5.3: Photoinduced Fano interference on Si. (a) Stokes spectra at 87 K for two different pump-probe delays. Continuous lines mark the results of the fitting with a Fano lineshape. (b), (c) Fitted inverse Fano parameter q^{-1} (see text) as a function of the pump probe delay for the high-fluence (b) and low-fluence (c) datasets, at room temperature and ~ 85 K. Continuous lines mark the results of the fitting with a step function.

The asymmetry of the LO Raman peak at positive pump-probe delays is illustrated more clearly in Figure 5.3 (a), in which we compare Stokes spectra acquired at -4 ps and +6 ps under high pump fluence and low temperature conditions. It is evident a reduction of the maximum intensity of the peak accompanied by an increase of spectral weight in its high-frequency tail.

An asymmetric lineshape of the LO phonon peak in the Raman spectrum of Si has long been reported in literature, associated to measurements on heavily p-doped samples. Such observation is ascribed to a Fano interference phenomenon, which occurs whenever there is a resonance between the energy of a discrete state (such as a phonon) and a continuum of states (such as electronic excitations, here creating a background in the Raman spectrum) [46]. This effect has been reported in a wide variety of spectroscopic investigations of atomic and condensed matter systems [47]. In detail, when such a resonance occurs, the peak corresponding to the discrete state acquires an asymmetric profile described by the Fano function:

$$I = \frac{(q+\epsilon)^2}{1+\epsilon^2} \tag{5.1}$$

where q is the so-called Fano parameter, controlling the asymmetry and inversely proportional to the spectral density of the continuum, and $\epsilon = 2(\omega - \omega_\nu)/\Gamma$ with ω_ν the discrete state frequency (the phonon frequency in the present case) and Γ its linewidth. The latter, besides the bare phonon part, acquires an additional contribution from the Fano interference, proportional to the spectral density of the electronic continuum.

In the case of the LO phonon in heavily p-doped silicon, the Fano interference arises from the presence of a continuum of allowed electronic transitions between valence bands. Indeed at the Γ point of the BZ, corresponding to the VBM, silicon exhibits several bands close in energy: an upper light-hole band and two lower heavy-hole bands (see Figure 5.1). When a sufficiently high hole density is induced ($p > 2 \cdot 10^{18}\ \mathrm{cm}^{-3}$), more than one valence band becomes partially depopulated, allowing electrons to be excited from the two lower valence bands into the empty states of the upper one. The energies of this continuum of Raman-allowed transitions overlap with the phonon frequency, giving rise to the interference phenomenon [48, 49].

In the present experiment, performed on an intrinsic sample and employing a 513 nm probe wavelength, the Fano interference is expected to be very weak [49, 50]. However, in this case, the hole density is generated by the above-bandgap pump pulse, and the Fano resonance is therefore induced transiently in the system, as previously demonstrated by Kato et al. [51] using time-resolved reflectivity, and by Zhu et al. [44] in a TRRS experiment similar to ours.

All spectra from the four datasets were fitted using a phonon lineshape given by the Fano function, convolved with a Gaussian function to account for the spectral resolution (fixed to the FWHM of the measured probe laser line). Stokes and anti-Stokes sides were fitted simultaneously. The results of the fit are shown along with the spectra in Figure 5.3 (a). The fit allowed to extract the characteristic parameters q and Γ, as well as the areas of the Stokes and antiStokes peaks. The inverse of the Fano parameter q^{-1}, is reported in Figure 5.3 as a function of the pump-probe delay for the high-fluence (panel (b)) and low-fluence data (panel (c)). The data show how at negative delays the measured spectra are well reproduced by lineshapes with $q^{-1} \sim 0.01$. While nonzero values of q^{-1} signal the presence of a slight asymmetry before the pump arrival, such small value could arise from ambient noise or different scattering from the sample. This is confirmed by the fact that the spectra at negative delays can be well reproduced also by fitting with Lorentzian lineshapes (the limit of equation 5.1 for $q \to \infty$, *i.e.* $q^{-1} \to 0$). Thus, the Fano interference is negligible at negative delays and small differences between q^{-1} values obtained from the different datasets are not considered physically relevant.

After the pump arrival, q^{-1} undergoes a step-like increase in all datasets, corresponding to an increased asymmetry, which is a consequence of the dynamical enhancement of the Fano interference. With our temporal resolution, such increase is nearly istantaneous, and the temporal trends can be properly reproduced by a step function:

$$f(t) = q^{-1}_{t<t_0} \cdot \theta(t - t_0) \; + \; q^{-1}_{t \gg t_0} \tag{5.2}$$

$f(t)$ was convolved with a Gaussian function providing the appropriate temporal resolution. The $q^{-1}_{t \gg t_0}$ values extracted from the fit are reported in Table 5.1. Since q^{-1} is directly proportional to the spectral density of the electronic continuum, we can inter-

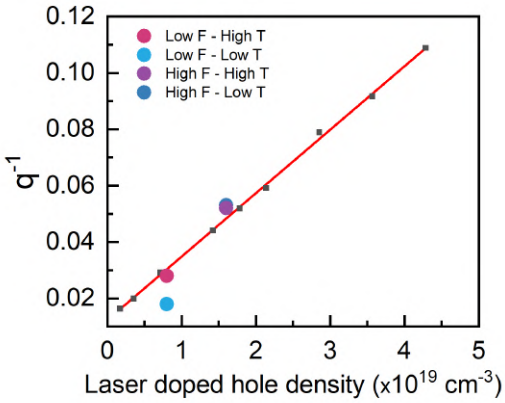

Figure 5.4: Dependence of the inverse Fano parameter on the photoexcited hole density. Black squares mark the q^{-1} values obtained by Zhu et al. [44] at room temperature in different excitation conditions, and a red line shows the result of a linear fit. The data corresponding to our measurements are shown as coloured dots with the same colour association used throughout the chapter. The points at high fluence are almost superimposed.

pret its temporal dependence as that of the photoexcited hole population [44]. Thus, the zero-delay time measured with the BBO crystal was corrected adjusting to zero the t_0 extracted from the fit of the q^{-1} trends.

The observed dynamics reveals the formation of a long-lived hole population, which remains essentially constant over the investigated timescale owing to the indirect band gap of silicon. At high fluence, regardless of the temperature, q^{-1} reaches after pumping a maximum value of ~ 0.053, which, according to the calibration reported by Zhu et al. [44], corresponds to a hole density of $n = 1.8 \cdot 10^{19}$ cm^{-3}, in excellent agreement with the estimation for our experimental conditions. When pumping with a lower fluence, however, a discrepancy emerges between the values obtained at the two temperatures. As shown in Figure 5.4, which compares our data with that of Zhu et al., the value of $q^{-1}_{t \gg t_0}$ obtained at room temperature agrees well with the density estimated at low fluence, whereas the corresponding value at low temperature is smaller than expected. This difference could arise from the fact that at a lower pump fluence the temperature-dependence of the dynamics observed in the system becomes more apparent, since part of pump-induced modifications mirror changes that can also be induced thermally. However, we warn that this effect may also result simply from an overestimation of the fluence in this particular dataset. Indeed since the fluence measurement depends critically on the spatial overlap and spot sizes of the pump and probe beams, it is generally prone to experimental uncertainty. This is especially true in the configuration used for low temperature measurements, with the sample hosted inside the pyrex glass of the UHV chamber. In the acquisition of the dataset, the pump–probe overlap or the spot size on the sample may not have been optimized correctly according to the procedure described in Chapter 4.1, leading to a lower effective pump fluence on the probed sample.

Apart from the absolute values reached, the hole dynamics does not exhibit any significant temperature dependence within the probed timescales. This observation further supports the electronic origin of the asymmetry. Indeed, given the carrier lifetime in silicon is of the order of nanoseconds [52], no temperature effect altering the excitation and recombination processes is expected to be measurable on a ps timescale.

An analogous trend to that observed for the Fano parameter is also found in the temporal evolution of the phonon linewidths, reported in Figure 5.5. At negative pump–probe delays, the linewidths extracted from the datasets measured at the same temperature

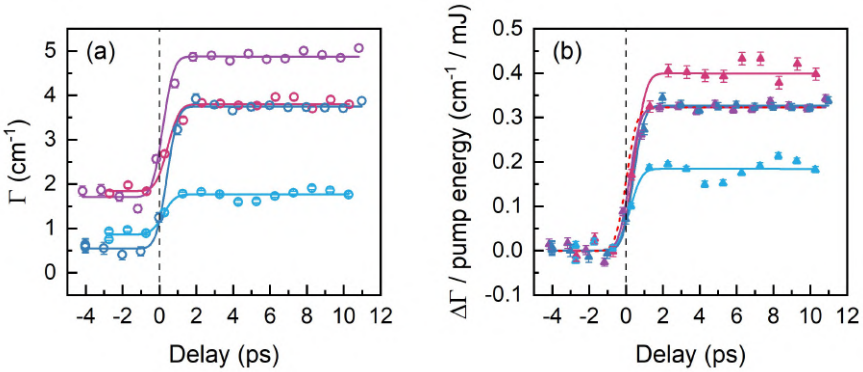

Figure 5.5: Temporal dependence of the linewidth parameter Γ. (a) Γ values extracted from the peak fit. (b) Variation of Γ at positive delays, normalized on the pump fluence. In both panels the four dataset are plot in the same color code used in Figures 5.3 and 5.4. Continuous lines mark the results of fitting with a step funcion. A dashed red line in panel (b) marks the evolution of q^{-1} for the high-fluence room-temperature dataset, rescaled on the y axis to fit into the plot.

have comparable values; lower Γ values are observed at lower temperatures, consistent with the typical temperature dependence of phonon peak widths in static Raman measurements [53]. Upon photoexcitation, the linewidth undergoes a pronounced step-like increase, which was fitted using the same functional form as in equation 5.2. The extracted parameters $\Gamma_{t<t_0}$, $\Delta\Gamma_{t\gg t_0}$, and t_0^{Γ} are summarized in Table 5.1.

As previously discussed, the width of the Fano lineshape comprises two contributions: a phononic term and a term proportional to the hole density. While both components could vary upon photoexcitation, a variation of the phononic component is expected to follow the increase in the phonon population, and thus to display a dynamics similar to that observed in the phonon temperature trends discussed in section 5.4. Thus, the fact that the broadening exhibits a clear step-like profile, closely mirroring that of q^{-1} (see dashed line in Figure 5.5 (b)), indicates that the pump-induced change is dominated by the electronic contribution.

The negligible modification of the phononic term is also evident from Figure 5.5 (b), where the variation ΔΓ, normalized to the exciting fluence, are shown. At high fluence the relative increase ΔΓ is indeed identical at both measured temperatures, with the difference in $\Gamma_{t\gg t_0}$, matching the one in $\Gamma_{t<t_0}$, ascribed solely to the phononic part. The normalized data also show that, as was the case for q^{-1}, in the low-fluence low-temperature dataset the pump-induced effects are proportionally weaker. In this case, contrary to what observed for the inverse Fano parameter, a mismatch is also visible between the normalized linewidth variations extracted from the low-fluence room-temperature dataset and from the high-fluence data. Given the nearly perfect match obtained for q^{-1} and that both quantities should be representative of the dynamics of the photoinduced hole population, the origin of this discrepancy remains unclear. Determining whether this observation reflects a genuine physical difference, indicative of distinct fluence dependencies of q^{-1} and ΔΓ, would require performing additional measurements over a broader range of pump fluences.

	$q^{-1}_{t\gg t_0}$	$\Gamma_{t<t_0}$ (cm^{-1})	$\Delta\Gamma_{t\gg t_0}$ (cm^{-1})	t_0^{Γ} (ps)
Low F Room T	0.028	1.8	2.0	0.4
Low F Low T	0.018	0.9	0.9	0.2
High F Room T	0.052	1.7	3.2	0.2
High F Low T	0.053	0.6	3.2	0.4

Table 5.1: Relevant parameters extracted from the fitting of the temporal trends of q^{-1} and Γ with a step function. t_0^{Γ} values are calculated with respect to $t_0^{q^{-1}}$.

5.4 Tuning anharmonic interactions by temperature

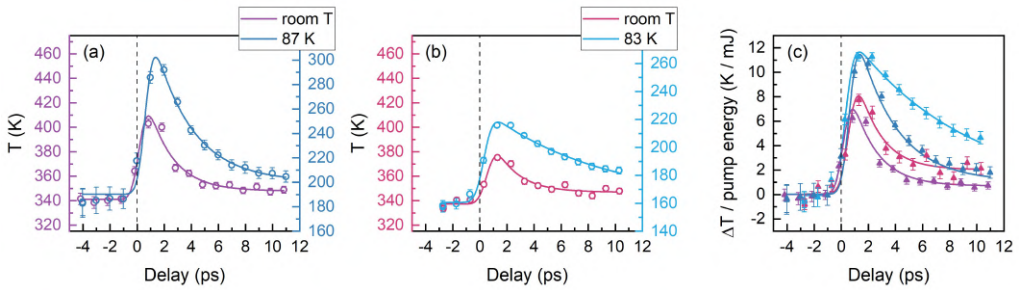

Figure 5.6: Temperature of the LO phonon peak as a function of the pump-probe delay for (a) the high-fluence and (b) the low-fluence datasets. (c) Phonon temperature variations normalized on the pump exciting fluence. Continuous lines in all panels display the results of the time trends fittings.

The measurement of both sides of the Raman spectrum, and their fitting with the Fano function, allowed to retrieve the integrated intensities of the Stokes and antiStokes Raman peaks I_S, I_{AS} and thus the equivalent temperature T of the LO phonon as a function of the delay (from $\frac{I_{AS}}{I_S} \approx \frac{(\omega_L+\omega_\nu)^3}{(\omega_L-\omega_\nu)^3} \cdot \frac{n_B+1}{n_B} = \frac{(\omega_L+\omega_\nu)^3}{(\omega_L-\omega_\nu)^3} \cdot e^{-\frac{\hbar\omega_\nu}{k_B T_\nu}}$, as illustrated in Chapter 3). T is plotted in Figure 5.6 (a) and (b) for the high-fluence and low-fluence datasets respectively.

We note that the measurement, at negative pump-probe delays, of phonon temperature values exceeding the temperature sensor reading more than 50 K is not to be ascribed to an actual increased temperature on the sample. Indeed, measurements performed with a continuous-wave source in analogous cooling conditions yielded antiStokes/Stokes intensity ratios in excellent agreement with Bose-Einsten statistics (see Figure 4.11 in Chapter 4). The observed discrepancies are therefore attributed to the effects of using a pulsed probe source, as discussed in Section 3.2.

As visible from the figure, in all datasets T has a prompt rise after the pump arrival, followed by a rapid decrease towards a plateau slightly higher than the initial value. In order to extract the relevant parameters from the observed dynamics, the temperature trends were fitted with an exponentially decaying function

$$f(t) = T_{t<t_0} + \theta(t-t_0)\,(Ae^{-(t-t_0)/\tau} + T_{t\gg t_0}) \tag{5.3}$$

which was convolved with a Gaussian function to account for the proper temporal res-

olution. The relevant parameters extracted from the fit of the four datasets are reported in Table 5.2, where ΔT_{max}, by subtracting the temperature value obtained at negative delays to the maximum of the fit.

	$T_{t<t_0}$ (K)	ΔT_{max} (K)	τ (ps)	t_0^T (ps)
Low F Room T	337	39	1.8	0.6
Low F Low T	161	57	8.6	0.3
High F Room T	341	68	1.9	0.2
High F Low T	190	112	2.9	0.6

Table 5.2: Relevant parameters and decay constants extracted from the fitting of the temporal trends of the phonon temperature with function 5.3 (see text). t_0^T values are calculated with respect to $t_0^{q^{-1}}$.

The results of the fits reveal that, across all datasets, the phonon population rises with a delay of a few hundred femtoseconds after the photoinduced holes creation, before decaying with a picosecond timescale. This behaviour is consistent with the characteristic dynamics expected for the transient creation of optical phonons via electron–phonon coupling and their subsequent decay via phonon–phonon anharmonic interactions. The delay between hole creation and the onset of the phonon population increase shows no clear dependence on fluence or temperature; given the limited number of sampled delay points in our measurements, the small differences observed across datasets are not considered physically meaningful. By contrast, the decay time constant τ exhibits a clear dependence on both fluence and temperature. At room temperature, the obtained τ values are essentially identical for the two excitation fluences, with $\tau = 1.8\,\mathrm{ps}$ and $\tau = 1.9\,\mathrm{ps}$ for the low- and high-fluence datasets, respectively. These values are in excellent agreement with the $1.7\,\mathrm{ps}$ timescale reported by Zhu et al. [44] for an excited carrier density of $1.8 \cdot 10^{19}\,\mathrm{cm}^{-3}$, comparable with the one achieved in our high-fluence regime. It is worth noting that Zhu et al. report a smaller increase in phonon temperature at comparable carrier densities; this is reasonably explained by their use of a longer pump wavelength (740 nm), which provides carriers with less excess energy relative to the CBM/VBM to dissipate via the creation of zone-centre phonons, and possibly by their lower temporal resolution, which would tend to smear the apparent maximum phonon temperature.

When the lattice temperature is reduced to $\sim 85\,\mathrm{K}$, the relaxation dynamics become noticeably slower at both fluences. This is an evidence of the reduction of the phonon-phonon anharmonic interactions, which is expected at lower temperatures due to a smaller equilibrium population of all lattice modes [54]. In this low temperature regime, τ also acquires a pronounced fluence dependence, being estimated at $2.9\,\mathrm{ps}$ for the high-fluence data compared with $8.6\,\mathrm{ps}$ for the low-fluence one. This difference is even more apparent in the temporal dependence of the normalized temperature variations shown in Figure 5.6 (c). Such behaviour can be ascribed to the variation of phonon–phonon interactions too: at high fluence, the pump generates a larger initial optical phonon population, enhancing the phonon–phonon scattering probability at short delays and thus shortening the relaxation time compared with a not (or slightly) perturbed system.

In addition to the differences in the relaxation times, the data in Figure 5.6 clearly reveal that the pump-induced increase in phonon temperature depends strongly on the initial lattice temperature. At both excitation fluences, the phonon temperature rise is substantially larger at low sample temperature, with maximum variations of $\Delta T_{max} = 112$

K at 87 K compared to 68 K at room temperature for high fluence, and 57 K at 83 K versus 39 K at room temperature for low fluence. This pronounced temperature dependence is particularly evident in the normalized trends shown in panel (c), where the room temperature curves are quite similar and remain well below the low temperature ones which, despite having clearly different decay rates, reach similar maxima.

We note that this effect cannot be attributed to electronic modification of the system: given that the bandgap of silicon increases at lower temperatures, leading to a reduction in the excess energy of the excited carriers relative to the CBM/VBM, this would result in the decrease of the photoexcited phonon population in the low temperature data [55], opposite to what observed. On the other hand, the reduction in phonon–phonon anharmonic scattering at ~ 85 K may underlie also the larger ΔT_{max} observed. Indeed, the resulting extended relaxation time, produces a bottleneck effect that allows optical phonons to accumulate. From this perspective, the similarity of the maximum phonon temperatures reached at low and high fluence for the ~ 85 K data is somewhat unexpected, given the much longer relaxation time in the low-fluence case. However, this dataset shows evidence, based on the q^{-1} and Γ parameters, of a lower effective photoexcited carrier density, suggesting that the actual excitation fluence was below the nominal value. An even higher ΔT_{max} would therefore be reasonably expected if the effective carrier density matched that of the low-fluence room-temperature dataset.

A similar bottleneck effect in the electronic system could also account for the fact that, at room temperature, the relative phonon temperature rise seems proportionally larger at low fluence. When optical phonons are heavily populated, indeed, the electron cooling rate can be reduced due to an increased probability of phonon reabsorption, effectively saturating the optical phonon population [56].

Although far from exhaustive, these results demonstrates that even in a seemingly simple material such as silicon, the dependence of the phonon excitation and relaxation times on temperature and fluence is far from trivial. It highlights the need for systematic investigations that could give new insights into the different coupling mechanisms at play and their tunability through ultrafast optical excitation.

5.5 Scattering strength dependence

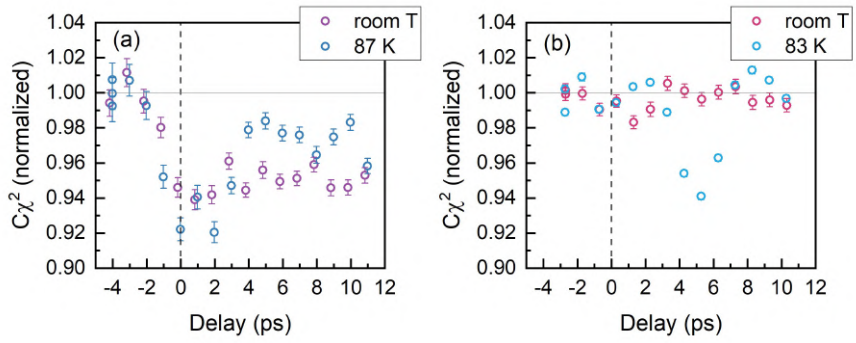

Figure 5.7: Temporal dependence of the Raman scattering strength of the LO phonon peak for (a) the high-fluence and (b) the low-fluence datasets. Data are normalized on the average value of the scattering strength at negative delays ($t < -1.5$ ps).

Finally, we address the reduction of the Raman signal observed on both the Stokes side and, at long delays, on the anti-Stokes side, as clearly visible in the difference spectra of Figure 5.2. From the expressions for the Stokes and antiStokes intensities discussed in Chapter 2, it follows that by measuring both sides of the Raman spectrum it is possible to extract, in addition to the phonon temperature, the Raman scattering strength of a specific phonon mode according to:

$$C\chi^2 \approx \frac{I_S}{(\omega_L - \omega_\nu)^3} - \frac{I_{AS}}{(\omega_L + \omega_\nu)^3} \tag{5.4}$$

where χ is the bilinear product of the Raman tensor with the electric field polarization vectors for incident and scattered radiation, and C is a factor containing the incident intensity and the optical constants.

The values of $C\chi^2$ extracted from the four different datasets are shown in Figure 5.7 as a function of the pump–probe delay. Since the absolute scattering intensity depends on the sample and on the specific alignment conditions, the data are normalized to the average value of $C\chi^2$ at negative delays ($t < -1.5$ ps). A clear reduction of the scattering strength, by about 5%, is observed only for the high-fluence datasets, whereas no significative variation is measured at low fluence. At high fluence, the temporal evolution shows a clear difference between the two temperatures: at room temperature, the decrease is almost step-like, reaching a nearly constant value at $t > 0$, while at low temperature a pronounced drop appears only near the pump-probe overlap and partially recovers to about half of its initial value at longer delays.

A reduction in scattering strength under high-fluence, room-temperature conditions was also reported by Zhu et al. [44], who observed an even larger decrease. They relate this observation to the increase of the hole population, explaining it by the quenching of the resonant conditions of the Raman process. Indeed, the use of an above-bandgap probe energy, as in the present case, allows for an enhancement of the Raman cross section proportional to the number of real electronic transitions that can be excited with the specific probe energy chosen. The photoexcitation of a carrier density by the pump can then result in a ground state bleaching/excited state filling effect for these transitions and lead to a reduction of the Raman scattering strength. While this explanation is plausible and consistent with their data, it would lead us to expect a visible reduction of $C\chi^2$ also in our low-fluence datasets, where the trends of q^{-1} and Γ described in section 5.3 indicate the presence of a significant photoexcited hole population. Moreover, it would predict a temporal profile of $C\chi^2$ mirroring that of the hole population (*i.e.* step-like), which is clearly not the case for the high-fluence low-temperature dataset.

Moreover, although the probe energy lies above the Si bandgap and is close to an indirect transition between the VBM at Γ and the CBM at L points in the BZ, the resulting enhancement of the Raman cross-section does not appear to be particularly significant [57]. The stronger effect seen by Zhu et al., and its close correlation with q^{-1}, Γ, and the excited hole population dynamics, may partly arise from a different calculation of the peak areas. While here we extracted them from the lineshape fitting with the Fano function, their calculation uses the integrated area over a ~ 60 cm^{-1} spectral range centered around the peak maximum. By excluding part of the peak tails, this approach could lead to interpret as a reduction of the area the redistribution of some spectral weight to higher frequencies by the Fano effect, thereby amplifying the apparent decrease when the peak becomes asymmetric.

While a reduction of the Raman scattering intensity is indeed observed in some of the

measured datasets, a satisfactory explanation that accounts for its dependence on both temperature and fluence still appears to be lacking.

CHAPTER 6

Transient photodoping and phonon dynamics in bulk and monolayer MoS_2

In the previous chapter, presenting the investigation on silicon, we focused on the dynamics of a single phonon peak and the information that can be retrieved from the photoinduced evolution of its lineshape and intensity. We now turn our attention to more complex semiconducting materials of lower symmetry and dimensionality, prototype of the currently defined "quantum materials": the transition metal dichalcogenide MoS_2. In this case a richer phonon density of states hosting optical modes with different symmetries allows for new phenomena to emerge. In particular, we show how photoexcitation in such systems can drive imbalances in the phonon mode occupancies and the renormalization of their frequencies that cannot be thermally induced. These imbalances not only provide insights into electronic relaxation pathways and the mode-specific electron-phonon coupling, but may lead to envision new ways to optically manipulate the material properties via the selective excitation of specific vibrational modes [58]. Furthermore, comparing samples of different thicknesses, we explore how changes in the electronic structure influence the ultrafast dynamics of carrier relaxation and the strength and character of the electron–phonon coupling.

Part of the results presented in this chapter have been published in [59].

6.1 Overview

Since the first mechanical exfoliation of graphene, in 2004, a considerable research interest has been attracted by quasi-two-dimensional layered materials, offering a vast playground for fundamental science studies while paving the way for realising flexible and miniaturised (opto)electronic devices. Among these materials, Transition Metal Dichalcogenides (TMDs) have emerged as particularly attractive owing to their semiconductive nature, strong light-matter interactions in the near infrared and visible range, and the presence of tightly bounded excitons, giving rise to potential novel applications [60, 61].

TMDs have a general formula MX_2, where M denotes a transition metal (such as Mo or W) and X is a chalcogen element (S, Se, Te). In their bulk form, TMDs are composed of stacked layers formed by covalently bound atoms, held together by weak Van der Waals interactions, as shown in Figure 6.1 (a). Each individual layer consists of a hexagonally packed plane of metal atoms sandwiched between two planes of chalcogen atoms. This layered configuration allows for easy mechanical or chemical exfoliation of bulk crystals to monolayer (1L) thickness, or for direct growth of atomically thin sheets. The specific

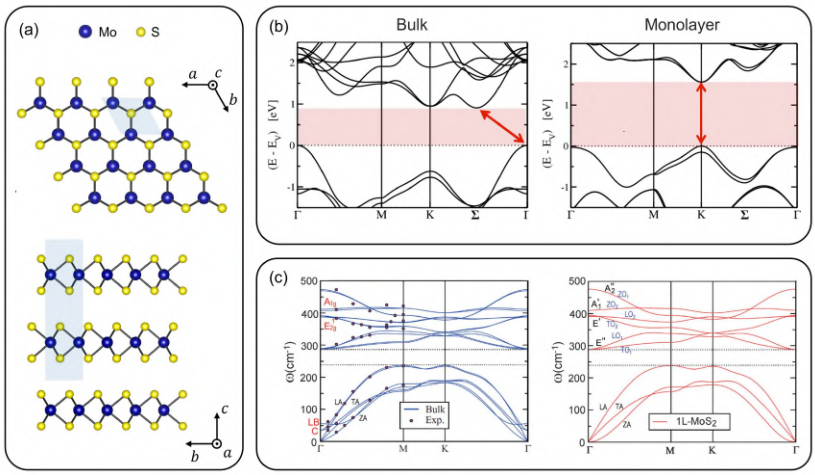

Figure 6.1: Structural and electronic properties of a 2H-MoS_2 crystal. (a) Crystal structure as seen from different lattice directions. In the view along the c direction (top) only one layer is represented. The crystal unit cell is highlighted in light blue. The structure was designed using VESTA [63]. (b) Calculated electronic band structure along the high symmetry directions for the bulk and 1L systems. The band gap is highlighted and a red arrow signals the corresponding electronic transitions. Adapted from [64]. (c) Calculated phononic dispersion along the high symmetry directions for the bulk and 1L systems. For the bulk sample, experimental data points are displayed on top of the calculated bands. Adapted from [62].

stacking of the layers determines the overall crystal symmetry, which is hexagonal in the most common polytype (2H).

Our work focused on MoS_2, a prototypical member of the TMD class, whose main electronic and phononic properties are summarized in Figure 6.1 (b) and (c). As visible from panel (b), reporting the calculated electronic band structure projected along the high symmetry directions, MoS_2 is characterized by an indirect bandgap in the bulk and a direct bandgap in the isolated single layer form. Indeed, the bulk has an indirect bandgap of ~ 1.2 eV corresponding to transitions from the Γ to the Σ points of the Brillouin Zone (BZ), while the 1L has a ~ 1.8 eV direct bandgap at the K point of the BZ. In the bulk, the local conduction band minimum (CBM)/valence band maximum (VBM) at the K point gives however rise to the lowest optical transition at ~ 1.93 eV [60]. The phononic degrees of freedom are instead less affected by the variation of the dimensionality: as shown from the calculated band structure in Figure 6.1 (c), the main differences between bulk and 1L consist in the disappearance of low energy optical modes (interlayer shear C and breathing LB) in the latter and in small variations in the other modes energy [62]. In particular, the energy difference between the A_{1g}/A_1' and E^1_{2g}/E' modes is progressively reduced from its ≈ 25 cm^{-1} bulk value in thinner samples, up to ≈ 18 cm^{-1} in the 1L; the measurement of this difference by Raman spectroscopy, as well as the C and LB modes, is routinely used in Raman studies to determine the thickness of few layer TMD samples.

A significant body of studies is available on semiconducting transition metal dichalcogenides, and in particular on MoS_2. So far, time-resolved experiments on MoS_2 have mainly focused on electron dynamics, demonstrating the photoinduced renormalization

of exciton and bandgap energies. The crucial role of the coupling with the phonon subsystem in determining the hot carrier relaxation dynamics has emerged from transient absorption measurements [65, 66]. However, the phonon dynamics remains largely unexplored, with indirect information obtained by studying the time-dependence of the exciton energy [67] and few recent ultrafast electron diffraction studies exploring electron-phonon coupling anisotropies at the BZ edges [68, 69].

This strongly motivates a TRRS investigation, providing direct access to the incoherent phonon relaxation, as well as electron-phonon coupling dynamics with mode specificity [34].

6.2 Experimental

In the following I report on a comprehensive TRRS study carried out on bulk and 1L MoS_2, aimed at monitoring the Raman spectrum after nearly resonant photoexcitation at the K point of the BZ.

Figure 6.2 shows the structure of the investigated systems: bulk MoS_2, where no substrate effects are expected; 1L MoS_2/ITO, i.e. single-layer MoS_2 on an indium tin oxide substrate, which is thermally insulating and electrically conductive; 1L MoS_2/Au, i.e. single-layer MoS_2 on a gold substrate, which is both thermally and electrically conductive. The measured bulk and 1L samples MoS_2 crystals were purchased from 2D Semiconductors Inc. (Scottsdale, AZ). For the 1L case, the epitaxially grown samples, transferred on flat gold and ITO substrates, were measured without further pretreatment. For the bulk, the measured sample was obtained by exfoliating a ~ 10 μm-thick flake (lateral size of some hundreds of μm) onto a diamond window. Diamond was selected as substrate because of flatness and because of the high thermal conductivity, minimizing sample damaging and enabling repeated measurements on the same spot.

The samples were characterized by measuring the equilibrium Raman signal under continuous wave (CW) excitation at 532 nm. The obtained spectra are reported in Figure 6.2 (a), (b), (c) for the bulk, the 1L MoS_2/ITO, and the 1L MoS_2/Au respectively. As visible from the figure, the Raman spectrum of MoS_2 in the considered frequency range comprises two main phonon modes: one is of symmetry E^1_{2g} in the bulk (measured at $\tilde{\nu} = 383\ \mathrm{cm}^{-1}$) and E' in the 1L (measured at $\tilde{\nu} = 384\ \mathrm{cm}^{-1}$ on Au), herein indicated as E mode; one is of symmetry A_{1g} in the bulk ($\tilde{\nu} = 407\ \mathrm{cm}^{-1}$) and A'_1 in the 1L ($\tilde{\nu} = 404\ \mathrm{cm}^{-1}$ on Au), herein termed A mode [62]. A redshift of about $1\ \mathrm{cm}^{-1}$ is observed on ITO as compared to Au, and ascribed to substrate effects, i.e. strain or intrinsic doping [70–73]. The spectrum also includes a two-phonon feature at about $450\ \mathrm{cm}^{-1}$, whose main component is ascribed to the combined excitation of two longitudinal acoustic modes ($2LA$) [74].

The pump-probe results summarized here were obtained through a series of experiments carried out over two years, all employing $\lambda = 633$ nm (~ 1.96 eV) pump pulses and $\lambda = 513$ nm (~ 2.41 eV) probe pulses. The pump energy is resonant with the system optical bandgap, providing photoexcitation at the K point of the BZ.

In the first set of experiments, all three of the above-mentioned systems were investigated in a high photodoping regime, employing pump fluences just below the assessed damaging threshold. In details, the used laser fluences were: $15\ \mathrm{mJ/cm^2}$ and $2.4\ \mathrm{mJ/cm^2}$ for the pump and probe respectively on the bulk sample, $4.5\ \mathrm{mJ/cm^2}$ and $1.4\ \mathrm{mJ/cm^2}$ on the 1L/ITO sample, $2.3\ \mathrm{mJ/cm^2}$ and $0.9\ \mathrm{mJ/cm^2}$ on the 1L/Au sample. In the last case,

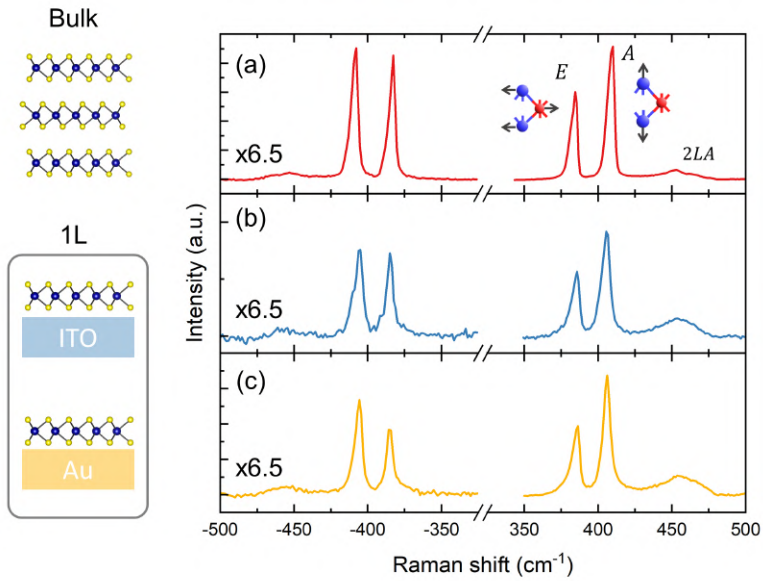

Figure 6.2: antiStokes and Stokes Raman spectra collected with CW excitation ($\lambda = 532$ nm). of (a) bulk MoS_2, (b) 1L MoS_2/ITO and (c) 1L MoS_2/Au. antiStokes spectra (left side) are multiplied by a factor 6.5 to enable the comparison with the Stokes spectra (right side). Peak assignment to the E-symmetry, A-symmetry and $2LA$ phonon modes is shown for the bulk, together with normal displacements of the two optical modes (represented only for one layer).

due to the high reflectivity of the Au substrate at the pump wavelength, the effective fluence on the 1L sample is given by almost twice the impinging fluence, leading to a similar value for the pump to the one employed for the 1L/ITO. These pump fluences result in excited carrier densities of 10^{14} cm^{-2} in the 1L samples and 10^{21} cm^{-3} in the bulk. We note that the latter value corresponds to an areal density of carriers of 10^{14} cm^{-2} for each layer, consistent with the 1L samples. The estimated charge density produced by optical pumping are calculated based on the optical properties of MoS_2 and, in the case of the 1L samples, of the substrates, as detailed in Appendix A.1 [75, 76]. Since the high-fluence measurements were performed just below the damage threshold, in this case each pump-probe acquisition was immediately followed by a reference spectrum taken without the pump. This procedure ensured that any pump-induced changes could be distinguished from potential sample degradation, which was carefully monitored throughout the experiment.

After we accomplished the upgrade of the OPA from 50 kHz to 200 kHz, the new working conditions enabled us to access a lower fluence regime without loosing the statistical value of the measurements. Under these new conditions, we acquired additional datasets on the bulk sample at 5 mJ/cm^2 and 10 mJ/cm^2 pump fluences (and $\sim$ 0.5 mJ/cm^2 and $\sim$ 1 mJ/cm^2 probe fluence).

In all measurements, Stokes and anti-Stokes signals were acquired simultaneously and we monitored the evolution of the A,E and $2LA$ phonon peaks. In order to resolve the A and E phonons, separated by about 20 cm^{-1}, the probe pulse duration was set

with the pulse shaper to $\Delta t = 1$ ps, granting a spectral resolution of $\Delta\tilde{\nu} = 15$ cm^{-1}. The pump pulse duration was set to $\Delta t = 0.6$ ps in the first high-fluence experiments, and to $\Delta t = 0.3$ ps in the low-fluence measurements. This affected only slightly the overall temporal resolution, largely governed by the probe pulse duration, which was obtained from the pump-probe cross correlation as $\Delta t = 1.2$ ps in the first case, and $\Delta t = 1.1$ ps in the latter case. These small variations are accounted in the data analysis by setting the proper resolution in the fitting functions.

6.3 Photodoping-induced phonon renormalization in bulk and 1L

TRRS spectra in the high-fluence regime in the pump-probe delay interval -3 – 500 ps are presented in Figures 6.3, 6.4 and 6.5 for the three investigated systems. The structure of the figures is the same, with data relative to bulk, 1L MoS_2/ITO and 1L MoS_2/Au samples, respectively. In panels (a), data for both Stokes and antiStokes signals are shown as an intensity map. In order to highlight the pump-induced spectral modifications, in panels (c) we show the difference spectra, obtained by subtracting the response in absence of the pump to each pump-probe trace. Spectra and differences at selected delays are presented in panels (b) and (d).

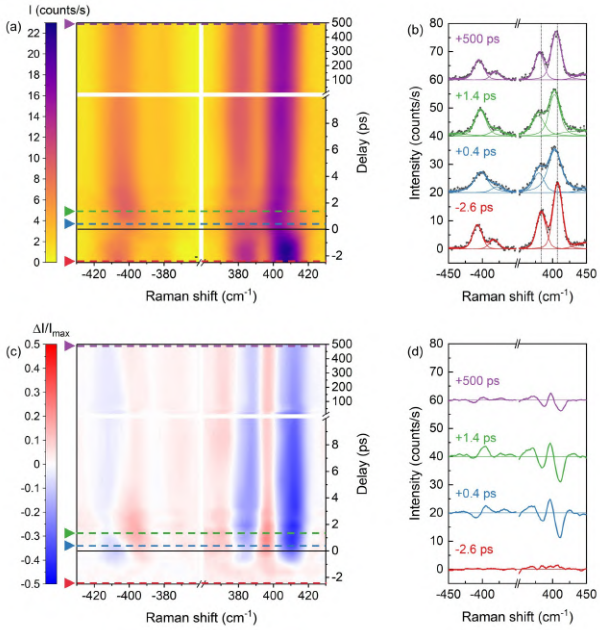

Figure 6.3: Time-resolved Raman scattering spectra and differences for bulk MoS_2 in the high fluence regime. (a) Intensity map of the spectra (after a linear background subtraction and a 5-points smoothing) versus pump-probe delay. A and E phonons are clearly visible on both the Stokes (right) and antiStokes (left) sides. Dashed lines mark the selected spectra presented, with their multipeak fitting, in panel (b). (c) Intensity map of the relative difference between the spectra obtained with and without the pump. Intensity differences are normalized to the maximum intensity in panel (a). (d) Selected difference spectra (same delays as in (b)).

In all three systems, the pump excitation induces a phonon mode softening along with a peak broadening within the first ps interval. This is particularly evident on bulk and 1L MoS_2/ITO from Figures 6.3 (a,b) and 6.4 (a,b). While both frequencies and linewidths relax towards their pre-pump values at longer delay times, significant differences between the bulk and 1L systems emerge. Indeed, panels (c) and (d) of the three figures show that the relaxation dynamics in the 1L samples is completed within the probed delay window, since only a negligible difference signal is detectable after ~ 100 ps. By contrast, in the bulk sample, pump-induced effects persist over the whole 500 ps

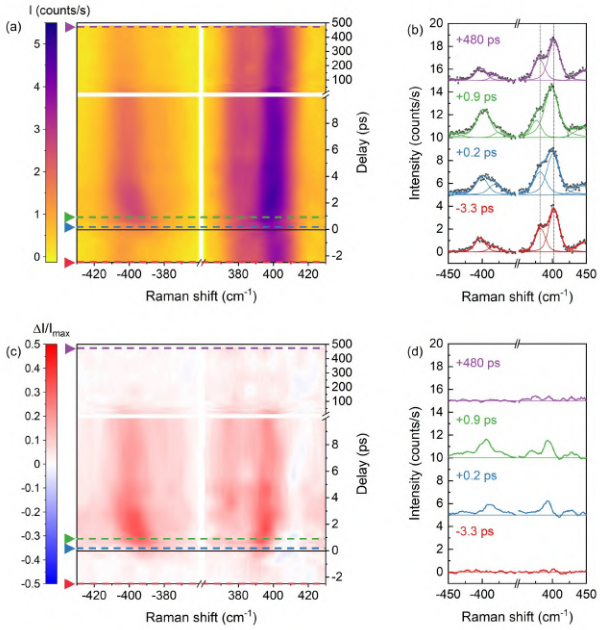

Figure 6.4: Time-resolved Raman scattering spectra and differences for 1L MoS_2/ITO in the high fluence regime. (a) Intensity map of the spectra (after a linear background subtraction and a 5-points smoothing) versus pump-probe delay. A and E phonons are clearly visible on both the Stokes (right) and antiStokes (left) sides. Dashed lines mark the selected spectra presented, with their multipeak fitting, in panel (b). (c) Intensity map of the relative difference between the spectra obtained with and without the pump. Intensity differences are normalized to the maximum intensity in panel (a). (d) Selected difference spectra (same delays as in (b)).

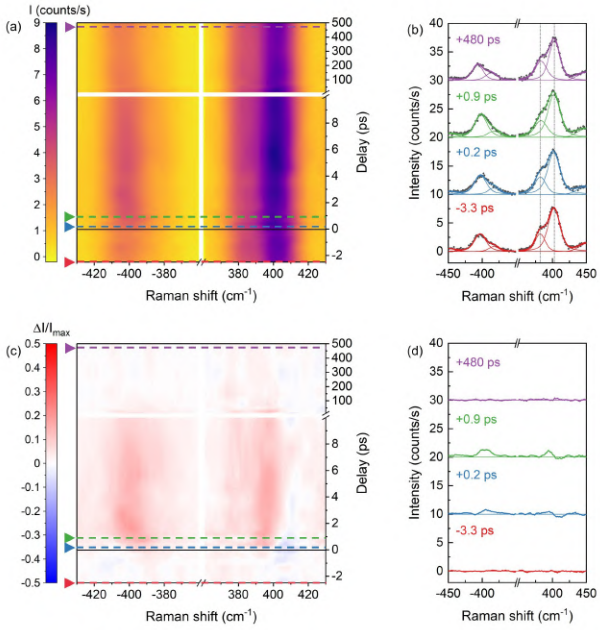

Figure 6.5: Time-resolved Raman scattering spectra and differences for 1L MoS_2/Au in the high fluence regime. (a) Intensity map of the spectra (after a linear background subtraction and a 5-points smoothing) versus pump-probe delay. A and E phonons are clearly visible on both the Stokes (right) and antiStokes (left) sides. Dashed lines mark the selected spectra presented, with their multipeak fitting, in panel (b). (c) Intensity map of the relative difference between the spectra obtained with and without the pump. Intensity differences are normalized to the maximum intensity in panel (a). (d) Selected difference spectra (same delays as in (b)).

window, with still clearly red-shifted peak positions. Another difference resides in the pump-induced variations of the Raman signal intensity. It can be noticed that photoexcitation in the 1L determines an overall enhancement of the signal, appearing as a positive trace (red area) in Figures 6.4 and 6.5 (c); in the bulk, instead, the signal is reduced, as particularly evident on the Stokes side (blue area in Figure 6.3 (c), accompanied by a red area arising due to peak frequency shift). We believe this observation to be related to the partially resonant nature of Raman scattering in the present conditions, discussed in Appendix A.3. On the other hand, for both bulk and 1L samples, the antiStokes-to-Stokes intensity ratios show qualitatively similar dynamical changes although developing over rather different timescales.

To enable a quantitative analysis of the data, we performed a standard fitting of the spectra. A multiple peak deconvolution was carried out as follows: the background was fitted with two different lines for the Stokes and antiStokes sides and subtracted; the probe laser line was acquired and fitted with a Gaussian function to determine spectral resolution; the A and E phonon peaks were fitted with Voigt profiles (*i.e.* the convolution of a Lorentzian and a Gaussian) with the Gaussian FWHM fixed at the measured spectral resolution, while the two-phonon peak at 450 cm^{-1} was fitted with a single, broad Gaussian function. For each peak, Stokes and antiStokes sides were fitted simultaneously, with the same parameters describing the distance from the laser line and the FWHM. The fit results on selected spectra are presented along with the data in panels (b) of the three figures. Having measured an additional spectrum without the pump after each pump-probe measurement, we were able to partially correct the possible effect of laser intensity fluctuations in the parameters extracted from the multipeak fitting. All parameters related to the high-fluence measurements presented in the following are indeed obtained subtracting the values extracted from unpumped spectra to the corresponding quantities derived from the pump-probe spectra, then summing back the average value of all unpumped spectra.

In the following we focus, as main objects of our investigation, on the time dependence of the frequencies $\tilde{\nu}_v$ and effective temperatures T_v for both the A and E lattice modes.

As thoroughly described in Chapter 3, the equivalent phononic temperature of each mode was obtained as:

$$T = \frac{\hbar\omega_\nu}{k_B} \frac{1}{ln\left(\frac{I_S}{I_{AS}}\left(\frac{\hbar\omega_l+\hbar\omega_\nu}{\hbar\omega_l-\hbar\omega_\nu}\right)^3\right)} \tag{6.1}$$

where in the present case I_S and I_{AS} are the integrated intensity of the peaks obtained from the data fitting. We note that we have neglected here the possible effect of a wavelength dependence of the sample optical constants. This is discussed in Appendix A.2, where it is shown that, even if this dependence could affect the temperature values extracted for the bulk sample, it would not have any effect on the measured dynamics.

In order to extract the characteristic time constants of the observed dynamics, the data were fitted with the function

$$f(t) = \alpha\,\theta(t-t_0)(e^{-(t-t_0)/\tau_1} + \delta e^{-(t-t_0)/\tau_2}) + k_{eq} \tag{6.2}$$

which was used for all the time dependent quantities. It is characterised by a step rise

centred at t_0 and a biexponential decay with time constants τ_1 and τ_2, with $\tau_1 < \tau_2$. α indicates the amplitude of the faster time trend (negative for the phonon frequencies), δ is the relative weight of the slower time trend. k_{eq} indicates the equilibrium value of the fitted quantity. Function 6.2 was convoluted with a Gaussian accounting for the temporal resolution (see Section 6.2). The time constants extracted from the data fit are reported in Table 6.1. As routinely done in pump-probe experiments, the zero-delay time measured with the BBO crystal was corrected adjusting to zero the fastest dynamics observed in the temporal scan, which coincides with the frequency shift in MoS_2 bulk and in the 1L MoS_2/Au (measured in the same alignment conditions as the 1L MoS_2/ITO).

	$\tilde{\nu}_A$			$\tilde{\nu}_E$			T_A			T_E			
	t_0	τ_1	τ_2	t_0	τ_1	τ_2	t_0	τ_1	τ_2	t_0	τ_r	τ_1	τ_2
Bulk	0	2.5	$\gg 500$	0	2.0	$\gg 500$	0.6	5.4	$\gg 500$	0.6	5.5	3.5	$\gg 500$
1L on ITO	0.2	1.0	31	0.2	2.3	28	0.4	5.3	81	-	-	-	-
1L on Au	0	-	17	0	-	40	0.5	2.0	10	-	-	-	-

Table 6.1: Time constants extracted from the fitting of the temporal trends on bulk and 1L MoS_2 in the high fluence regime. Time delays are expressed in ps. The t_0 values are obtained as a shared fitting parameter for the two phonon modes, both for the frequencies and the temperatures.

In Figure 6.6, we show the evolution of the measured A mode frequencies $\tilde{\nu}_A(t)$ and effective temperatures $T_A(t)$ for all the three samples as a function of pump-probe delay. Solid lines are the best fit curve obtained from Equation 6.2. The behaviour already visible from the intensity maps in Figures 6.3, 6.4 and 6.5 is clearly appreciated here: a prompt redshift of the phonon modes occurs right after the pump arrival, followed by a slow and sample-dependent relaxation dynamics. In all systems, we also observe a marked increase of the phononic temperature after photoexcitation: that reflects the expected rise in phonon population due the dissipation of the excess electron energy via electron-phonon coupling.

In Figure 6.6 (a) the bulk sample shows a nearly instantaneous drop ($t_0^{\tilde{\nu}_A} \sim 0$ ps) of $\tilde{\nu}_A(t)$, reaching the maximum softening of $\Delta\tilde{\nu}_A^{max} \sim -7$ cm^{-1} (extracted from the fit with function 6.2). That is followed by a fast recovery dynamics ($\tau_1^{\tilde{\nu}_A} \sim 2$ ps) and a consequent very slow one, exceeding the accessible delay window ($\tau_2^{\tilde{\nu}_A} \gg 500$ ps). The phonon softening $\Delta\tilde{\nu}_A(t)$ is accompanied by an increase of the phonon temperature, $\Delta T_A(t)$, with $\Delta T_A^{max} \sim 490$ K. The subsequent relaxation dynamics is well reproduced with a fast decay time constant $\tau_1^{T_A} \sim 5$ ps and a longer one $\tau_2^{T_A} \gg 500$ ps as occurred for the frequency shift. Remarkably, the rise of $T_A(t)$ is delayed of $t_0^{T_A} \sim 0.6$ ps with respect to the phonon frequency shift. This observation occurs in all three samples (insets of Figure 6.6) and plays a relevant role in rationalizing the origin of the phonon softening.

Although the softening of phonon frequencies can be due to lattice thermal expansion [53, 77–81], in the present case phonon softening occurs before the increase of T_A, *i.e.* before the energy transfer from electron to phonon bath. That suggests the observed phonon redshift in the early time range to be primarily electronic in origin. Phonon frequency renormalization has been indeed observed in gated samples of MoS_2 and other TMDs [82–84], where it has been associated to the effect of the electron-phonon screening induced by carrier injection [84, 85]. A similar, even stronger effect was predicted theoretically to occur following photodoping, leading to a large, expected, phonon softening in ultrafast non-equilibrium measurements [86]. Girotto et al. estimated an expected frequency shift in the order of 10 cm^{-1} upon an initial excited carrier density of 10^{14}

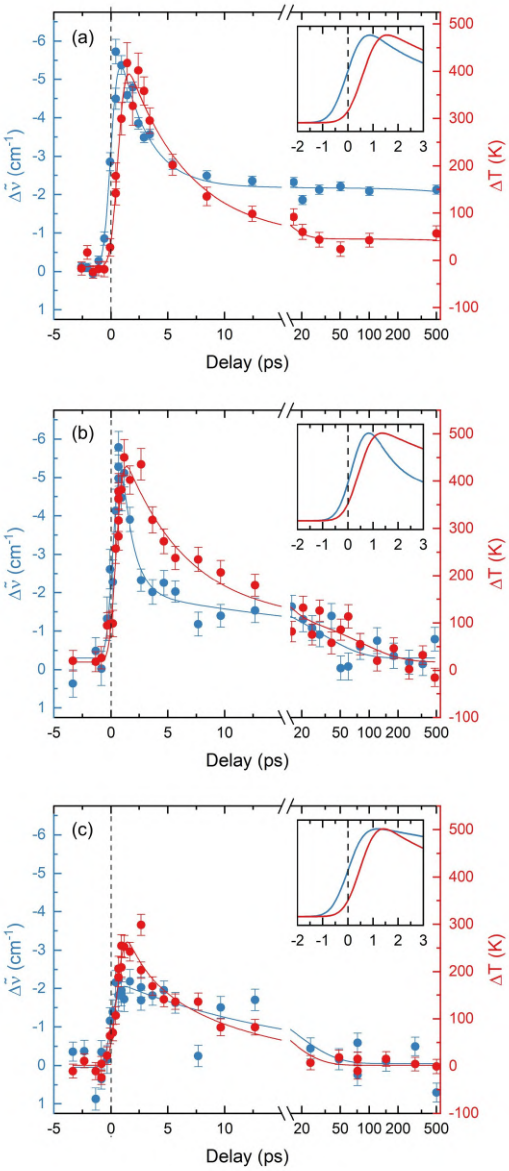

Figure 6.6: Temporal evolution of the A phonon frequency and equivalent temperature for (a) bulk, (b) 1L on ITO and (c) 1L on Au samples. The variation of the phonon peak positions, from multipeak fitting, are displayed as blue dots, and the variation of the temperatures extracted from Equation 6.1 as red dots. Continuous lines show the best fit curves. A dashed vertical line marks $t_0 = 0$ ps. In the insets, we compare the fitting curves of frequency shift and temperature at short times, normalised to the maximum value, evidencing a clear delay between the rise of the two quantities.

cm^{-2} for 1L MoS_2. Such values are compatible with the present experimental conditions (see Section 6.2). We thus ascribe the prompt frequency shift in the early ps range to the enhanced screening induced by the resonant pump-driven transient doping of the system at the valleys. Moreover, we can expect the redistribution of both electron and hole excited carrier densities to be responsible for the short time relaxation dynamics. The fast decay can be most likely associated to non-radiative processes [87], rather than radiative recombination, typically occurring on a longer timescale [88–91].

6.4 Substrate effects on renormalization dynamics

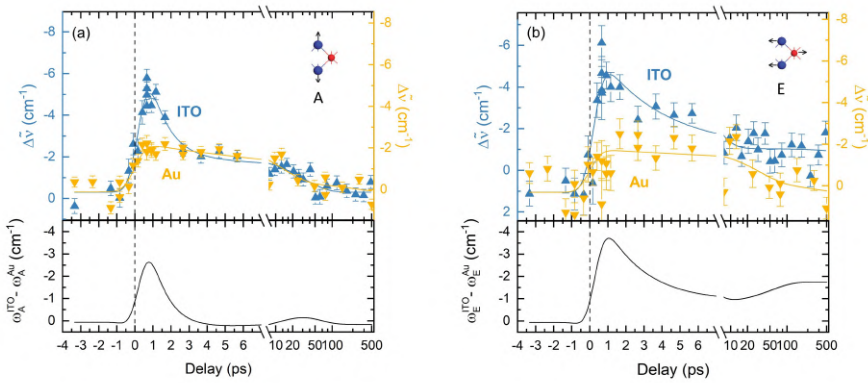

Figure 6.7: Effects of the substrate, ITO (blue) or Au (yellow), on the frequency shifts on 1L MoS_2 for (a) A out-of-plane mode and (b) E in-plane mode. Continuous lines display the best fit curves. Bottom panels: differences between fitting curves on ITO and Au, rigidly shifted to a null difference at negative delays (thus, excluding pump-independent differences). At short delays, the difference is evident in both modes, whereas at long time delays a mismatch remains only for the E mode.

Within this context, further insights can be retrieved from the comparison between the bulk system and 1L samples on substrates. The behaviour observed for 1L MoS_2/ITO appears rather similar to the bulk in the early ps range, showing actually the same frequency shift and phonon temperature ($\Delta\tilde{\nu}_A^{max} \sim -8\ \mathrm{cm}^{-1}$, $\Delta T_A^{max} \sim 480$ K) and a slightly smaller fast decay time after photoexcitation ($\tau_1^{\tilde{\nu}_A} = 1.0$ ps), possibly reflecting the higher electrical conductivity of ITO compared with MoS_2 itself. As to the slower delay constants τ_2, 1L MoS_2/ITO shows a striking difference with the bulk sample, since both $\tilde{\nu}_A(t)$ and $T_A(t)$ undergo a complete relaxation in the order of tens of ps (see Table 6.1). The time-dependent phonon response in 1L MoS_2/Au shows further differences to be connected with a prominent role of the substrate. Even in this case, similarly to the sample on ITO, the relaxation dynamics is fully completed within 500 ps, for both $\tilde{\nu}_A(t)$ and $T_A(t)$. However, the frequency shift here is much smaller than in the 1L MoS_2/ITO case and, more importantly, the relaxation dynamics does not show the fast decay component. This is particularly evident from Figure 6.7 (a), where the A mode frequency shifts, $\Delta\tilde{\nu}_A(t)$, of the two 1L samples are compared. A strong influence of the substrate on 1L systems is not unexpected [62, 70, 71, 92]. The work function of Au is greater

than that of MoS_2 implying that the band alignment of the MoS_2-Au interface favours electron transfer from MoS_2 to Au. Hence, the substrate provides a very efficient dissipation channel (sink) for the excited carriers on timescales of about 10-100 fs [93–95]. We argue that this quenches the photodoping-induced phonon renormalization faster than our temporal resolution. At longer time delays, as shown in Figure 6.7 (a), the $\Delta\tilde{\nu}_A(t)$ trend for 1L MoS_2/Au is basically superimposed to that of 1L MoS_2/ITO, suggesting the slower relaxation dynamics being little affected by the substrate. This is quantitatively verified by the similar values of $\tau_2^{\tilde{\nu}_A}$ obtained by fitting on both samples.

Data and best fit curves on the time evolution of the E mode frequency renormalization $\Delta\tilde{\nu}_E$ for the two 1L samples are also compared in Figure 6.7 (b). It is apparent that, in this strong photodoping regime, the renormalization of the E mode takes place to the same extent and with the same time dependence as that of the A mode. This is the case also for the bulk sample (see Figure 6.15), for which, however, a more detailed discussion on the fluence dependence of the renormalization of the two modes has been developed and presented in Section 6.7. The temporal evolution of the E mode frequency shifts confirms the observations made on the bulk, not completing the relaxation towards equilibrium in the studied time delay windows, and that on the 1L MoS_2/Au, lacking the first fast decay component. This results in comparable values of $\tau_1^{\tilde{\nu}_v}$ and $\tau_2^{\tilde{\nu}_v}$ estimated for each sample (see Table 6.1).

The comparison of E mode frequency shifts for the two 1L samples evidences however a further difference between the two substrates. On Au, the E mode shift is basically the same as the A mode in terms of both amplitude and temporal dependence. In 1L MoS_2/ITO, instead, the E mode shifts more than the A and does not return to equilibrium within 500 ps (Figure 6.7 (b)). This asymptotic offset in the time decay of $\Delta\tilde{\nu}_E$ is estimated by fitting as $-1.9\ \mathrm{cm}^{-1}$. We interpret the observation as a marker of strain. Indeed, lattice expansion of the substrate due to pump-induced heating can generate a tensile strain on 1L MoS_2 which, acting along the in-plane directions, affects the E phonon frequency much more than the A [96–98]. This effect is more pronounced on ITO because of its thermal conductivity (5 $\mathrm{W/mK}$), much lower than that of gold (317 $\mathrm{W/mK}$) and of MoS_2 itself (35 $\mathrm{W/mK}$) [77, 99]. Remarkably, only in the 1L on ITO, the frequency shift appears delayed with respect to time zero (see insets of Figure 6.6), as caused by a substrate-induced strain component in the observed shift.

6.5 Mode-dependent electron-phonon coupling

We now concentrate on the temperature dynamics of the A and E modes, as obtained from the antiStokes-to-Stokes intensity ratio. Out-of-equilibrium studies are often interpreted in the framework of two-temperature models, considering two different temperatures for the weakly-coupled electronic and lattice subsystems in a transient configuration [100]. However, this picture has proven to be unsatisfactory in several materials [101–103]. This emerges clearly also from our present data. The temperatures extracted from equation 6.1 for the A and E phonons in the three samples are shown in Figure 6.8. The behaviour of the two modes appears dramatically different, regardless of the specific sample. The A mode temperatures are much higher than ambient temperature even at negative time delays and have a prompt and marked increase of $\sim 300 - 400$ K after the pump arrival. On the other hand, the temperatures of the E mode are only slightly higher than room temperature (~ 290 K) at $t < 0$, and display a slow and smooth increase of only $\sim 100 - 150$ K at positive delays.

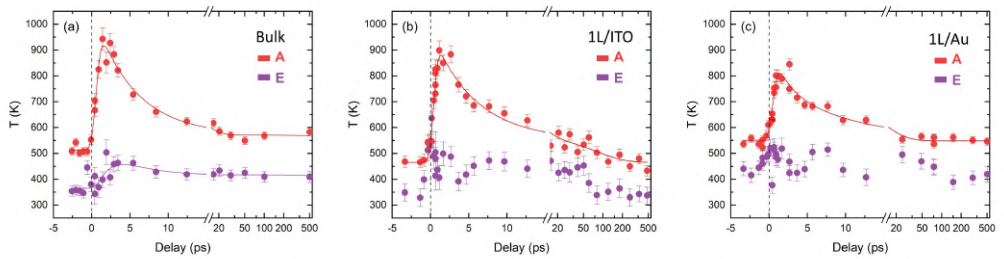

Figure 6.8: Phonon temperatures for the two phonon modes in bulk (a), 1L on ITO (b), 1L on Au (c) MoS_2 estimated from the ratio between antiStokes and Stokes intensities from data fitting. Continuous lines display the results of the time trends fittings.

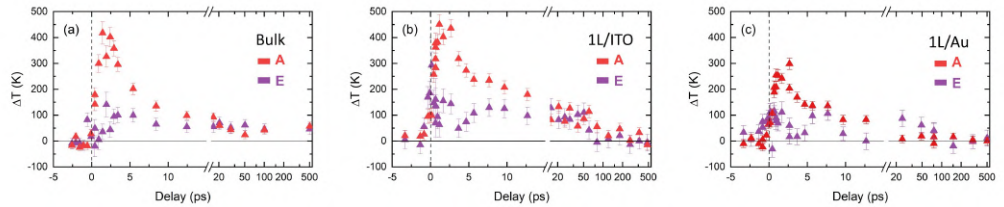

Figure 6.9: Temperature variations in bulk (a), 1L on ITO (b), 1L on Au (c) MoS_2. Red (purple) points represent the difference between the A (E) phonon temperatures obtained from the antiStokes-to-Stokes intensity ratio (equation 6.1) of spectra acquired with and without the pump.

The observation of a difference between the modes before time zero is remarkable per se. It is known from literature that electronic resonances can alter the antiStokes-to-Stokes intensity ratio, rendering equation 6.1 inapplicable. Some of these apparent temperature anomalies seem to arise from the different relative position of the antiStokes and Stokes transitions with respect to an electronic resonance, *i.e.* a peak of the joint density of states; that was also observed in $MoTe_2$ [104]. Another possible reason for a failure of the simple hypothesis of equation 6.1 might arise from symmetry-related differences in the resonant Raman cross sections for the two phonon modes [105]. In both these cases, the anomalies should be observed also in the equilibrium Raman spectra, acquired with the same probe wavelength. The spectral shape measured with a standard 532 nm CW probe (see Figure 6.2 in Section 6.2) is however fully compatible with room temperature conditions and the extracted temperature appears on the contrary slightly enhanced (< 40 K) for the E mode, as already observed in similar experimental conditions [106]. The difference in the mode temperatures appears only using a pulsed laser source, implying it is a non-equilibrium effect: we argue that the observation is a signature of a stronger coupling of the A phonons with the electronic degrees of freedom, as discussed in Chapter 3.

Given the probe wavelength is weakly resonant with the electronic transitions in MoS_2 (both bulk and 1L), the relaxation of the small electron population excited by the probe itself creates an excess population of optical phonons within the probe duration. That is expected to contribute to the measured antiStokes intensity resulting in an increased effective local temperature in time. Electron-phonon coupling can thus be responsible for the imbalance in the initial ($t < 0$) population of A and E phonons. Since

the enhancement of the base temperature of the A phonons is independent on the pump, this effect does not impair the interpretation of the pump-induced increase in phonon population and its relaxation dynamics, which are encoded in the observed variation ΔT with respect to the measurement without the pump, reported in Figure 6.9.

The time evolution of $\Delta T(t)$ confirms that the A mode is more strongly coupled with the electron reservoir than the E mode, representing a prevalent electron-phonon scattering channel. Indeed, the increase in the E temperature is slower and we found that a smooth rise, modelled with an extra term $\left(1 - e^{-\frac{t-t_0}{\tau_r}}\right)$ in the fitting function 6.2, provides a better fit to the data than a step-like increase. The result of the fitting for the bulk, with $\tau_r \sim 5.5$ ps, is shown on the data in Figure 6.8 (a). The electron de-excitations via creation of E phonons thus result to occur at a lower rate than de-excitations involving A phonons and possibly E phonons are created at a later stage via anharmonic phonon-phonon relaxation. In the 1L samples, the low intensity of the E antiStokes peak and the overlap with the A peak result in a lower accuracy of the fitted intensity and antiStokes-to-Stokes ratio. Thus, no fitting was performed on the T_E temporal trends, which in any case clearly follow, at short delays, the behaviour described for the bulk (see Figures 6.8 (b) and (c)).

By looking at the time trends of ΔT_A, ΔT_E (Figure 6.9), we can see how the population of the two modes becomes equal only at $t \gtrsim 20$ ps in all samples. This value can thus be taken as an estimate of the time after which a single temperature can adequately describe the entire phonon bath (or at least the optical phonons). It is evident that, at smaller delays, describing the phonon dynamics with less than two temperatures is not possible. Indeed, the A and E modes exhibit a "hot phonon" and a "cold phonon" behaviour, respectively, which necessarily derive from a very different symmetry-dependent coupling with the electrons [102, 103]. Theoretical works reported in the literature have suggested that the out-of-plane atomic displacement, induced by the A phonons, modulates significantly the electronic band dispersion [107], and particularly the conduction band minima at the K point of the BZ. The in-plane distortion induced by E phonons is expected to have a minor effect on the electronic states [84].

Overall, the presented data represent an evidence of the creation of a non-thermal phonon distribution, which by definition cannot be observed under equilibrium conditions, surviving at least up to 20 ps. A timescale of tens of ps for the thermalization of the phonon subsystem is consistent with the findings of Caruso [108] and Britt et. al [68] which, however, describe the inhomogeneous excitation of the phonons across the BZ without appreciating a substantial difference between the A and E at Γ.

6.6 Relaxation dynamics

Based on the considerations above, we attempt to rationalize the consequent steps in the system relaxation dynamics, involving both electronic and phononic degrees of freedom.

We interpret the phonon renormalization at short delays as a signature of the transient, pump-driven photoexcited electron population. After ultrafast internal thermalization of the electrons to a pump-dependent temperature T_{el}, the carrier relaxation proceeds, determining the observed short time dynamics in the phonon frequencies. At the early ps scale, we can expect the carrier density to be depleted mainly via non-radiative processes (e.g. Auger, scattering by defects, charge transfer to the substrate in 1L samples, etc.), whereas electron-phonon scattering provides a dissipation channel decreasing

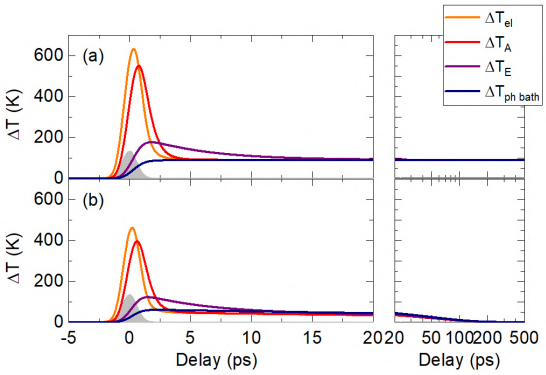

Figure 6.10: Sketch of the evolution of the internal temperature of the various subsystems interacting in the relaxation dynamics of: (a) bulk MoS_2; (b) 1L MoS_2 on substrate. The pump temporal profile is displayed as the shadowed grey area. The time dependent temperature variations of the electrons, A and E symmetry phonons, and the phonon bath are displayed in solid lines with colours according to the legend.

the effective electron temperature T_{el}. This goes along with an increase of the population of selected phonon modes, coupled to the photoinduced electron and hole charge pockets. In TRRS spectra, the dynamics of frequency shift and effective phonon temperature provide two independent useful channels for tracing these different physical processes, i.e. charge redistribution and energy transfer. In both, the influence of the substrate on the 1L samples is evident. Concerning the carrier depletion (and associated frequency shift), we observe stronger deviations from the bulk behaviour for more efficient MoS_2-substrate charge transfer [93–95]. It is safe to assume that the transient phonon populations produced by electron relaxation do not contribute to any substantial modifications to the phonon spectrum at this timescale. Indeed, as expected from literature [68, 108, 109] and clearly observed in our measurements, at time delays shorter than 20 ps the phonon distribution is highly non-thermal, with a marked difference in the population of different modes. Selectively populating some of the phonon modes does not inherently alter the equilibrium positions of the ions in the same way as thermodynamically increasing the temperature does, thus leaving the bond strength and phonon frequencies unperturbed.

As shown in the previous section, the electron-phonon driven increase in the effective lattice temperatures is highly mode-selective. We here introduce a multi-temperature model to describe the overall system relaxation dynamics, noting that reproducing the observed phenomenology requires the use of at least 3 different temperatures for the phonon subsystem. The model, developed by E. Cappelluti following [102], is detailed in the Appendix A.4. The result of its application to the bulk sample of this experiment is sketched in Figure 6.10 (a). At the pump arrival, its energy is deposited in the electron subsystem, as visible from the increase in the electron temperature T_{el}. As the electron relaxation proceeds, with a ps delay with respect to the rise of T_{el}, the strongly coupled A phonon mode is first populated, then the equivalent temperature of the E mode grows, to reach a maximum at a few ps delay. The thermalization of the two modes with the phonon bath (*i.e.* all other phonon modes) occurs within 20 ps. In the model, the electron-phonon coupling strengths and the modes specific heats are selected to closely follow the observed dynamics, in terms of kinetics and observed temperature variations. The experimental trends are properly reproduced by setting an electron-phonon coupling of the A phonon 10 times greater than the one of the E phonon. Overall, if an independent experimental assessment of the photoexcited electron temperature was present, the model would allow a direct measurement, based on TRRS data, of the mode-dependent electron-phonon coupling strength.

At longer timescales, thermal and charge diffusion outside the scattering volume could be at work. In that case, the restoring of the initial charge/temperature conditions would be expected. Our findings suggest, however, that such diffusion processes are only weakly operative in the bulk system. Indeed, in the experiment conducted on the bulk, both the phonon frequencies and the phonon temperatures display a plateau behaviour for $t > 20$ ps, with a residual frequency shift $\Delta\tilde{\nu}$ greater than 2 cm^{-1} and an excess of 55 K in the phononic temperature of both modes at $t = 500$ ps. Given this excess temperature does not explain the measured phonon shift [77–81] (see Figure 6.11 (a)), we conclude a finite transient doping is still present in bulk compounds at $t = 500$ ps. That can be ascribed to long-lived excitons or trapped states [110]. Overall, the pump-driven excess energy is not fully dissipated, thus resulting in asymptotic temperatures exceeding the starting values for all the system degrees of freedom, as depicted in the right panel of Figure 6.10 (a).

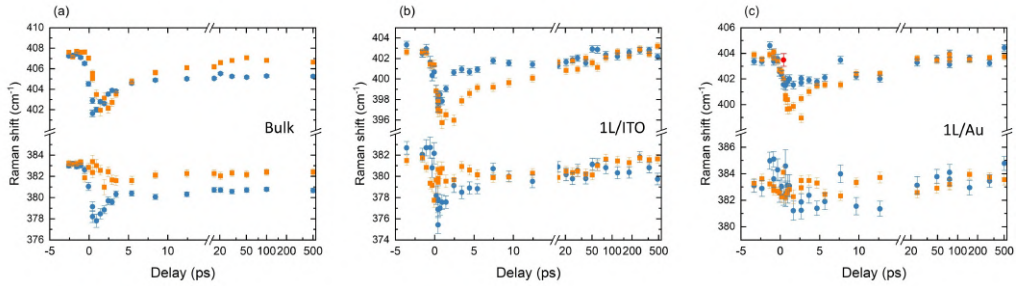

Figure 6.11: Comparison between measured phonon frequency shifts and values expected if the measured dynamical ΔT was reached under equilibrium conditions, for (a) bulk, (b) 1L on ITO and (c) 1L on Au samples. Blue dots mark the phonon peaks positions extracted from the multipeak fitting, while orange squares are calculated from the temperature data using $d\omega/dT$ values obtained from [78].

In both 1L samples, the short timescale evolution of the phonon temperatures is similar to the bulk case. Here as well, at $t > 20$ ps, lattice thermalization has occurred. The timescale is compatible with the (indirect) measurements of Chi et al. [67]. Interestingly, by calculating the phonon softening $\Delta\tilde{\nu}$ expected if the measured transient ΔT was reached under equilibrium conditions (reported in Figure 6.11 (b) and (c)) one finds that for $t > 20$ ps the thermal contribution can fully explain the observed frequency shifts: contrary to what is observed in the bulk, electronic effects on the phonon spectrum in the 1L appear negligible after a few tens of ps. This implies that the electronic relaxation processes in 1L samples promptly damp the photodoping below the threshold needed to appreciate its effect on the phonon spectrum. Beside the possible charge transfer to the substrate, carrier de-excitation is indeed expected to be faster in 1L samples, where the direct bandgap allows for radiative recombination, than in the bulk, where it is entirely phonon-mediated and thus less efficient. In addition, a crystal surface typically contains a higher concentration of defects than the bulk, leading to a possible increase in defect-mediated non-radiative recombination in 1L samples [111]. The difference between the 1L on ITO and Au resides is in the efficiency of electron population depletion and thermal dissipation by the substrate, both higher in Au: coherently, in the 1L/Au sample, both the $\tau_1^{T_A}$ and $\tau_2^{T_A}$ result smaller as compared to the 1L on ITO. Instead, one can expect a similar phonon de-excitation pathway in the 1L/ITO and bulk samples, given

they are both governed by the in-plane heat diffusion inside MoS_2 (ITO has a very poor thermal conductivity). The fact that the long timescale relaxation in the phonon population on ITO differs from that of bulk MoS_2 further corroborates our interpretation on the role of the residual transient doping in keeping the bulk sample out of equilibrium. The loss of the pump-driven photoinduced charge/energy due to all these combined effects in 1L samples on substrates can be also considered in the multi-temperature model, as discussed in Appendix A.4. The qualitative theoretical behaviour is displayed in Figure 6.10 (b), showing the complete relaxation of the 1L system, in substantial agreement with the experimental scenario.

6.7 Fluence dependence and nonlinear phonon renormalization

Measurements performed at reduced excitation (pump) fluence allow us to explore the behaviour of bulk MoS_2 in weaker doping regimes. This is particularly relevant in TMDs, where the presence of a multivalley electronic band structure and of strongly bound excitons give rise to distinct phenomenology depending on the excited carrier density. In particular, populating more than one valley has been shown to impact the validity of the adiabatic approximation and alter the phonon energies [84, 85], while exceeding the so-called Mott density leads to a transition from an excitonic regime to one characterized by unbound carriers (electron-hole plasma/liquid) [112–114]. These transitions can significantly modify both the carrier-induced screening and the electron-phonon coupling, that we probe via TRRS by monitoring the time evolution of phonon temperatures and frequency renormalizations.

Figure 6.12 shows the TRRS spectra (a) and the difference spectra (b) as a function of the pump-probe delay measured at the lowest excitation fluence of 5 $\mathrm{mJ/cm^2}$, corresponding to an excited carrier density of $\sim 7.3 \cdot 10^{20}$ $\mathrm{cm^{-3}}$. For comparison, the excited carrier density were estimated to be $\sim 1.5 \cdot 10^{21}$ and $\sim 2.2 \cdot 10^{21}$ $\mathrm{cm^{-3}}$ for the datasets obtained with 10 and 15 $\mathrm{mJ/cm^2}$ pump fluences, respectively (the detailed calculation is provided in Appendix A.1). The probed delay range spans from -3 to 100 ps. The difference spectra were obtained in this case by subtracting the average response at negative delays (between -3 and -1.5 ps).

As expected, the pump-induced effects observed in Figure 6.12 are less pronounced than those seen at higher fluence in Figure 6.3. Nevertheless, the main qualitative features remain consistent: the pump induces a softening and broadening of the phonon peaks, an increase in the antiStokes intensity and a decrease in the Stokes intensity. These effects are notably long-lived, as evidenced by the absence of a complete return to equilibrium within the 100 ps time window of our measurements. One difference can however be noted: the softening of the E mode near the pump-probe coincidence time is significantly less visible in this case. This is evidenced, in the difference maps in panel (c), by the lack of a marked red (positive) region to the left of the Stokes equilibrium position of the E mode, indicating a weaker shift of the peak.

To analyze these spectra and the spectra obtained with 10 $\mathrm{mJ/cm^2}$ pump fluence, we applied the same multiple peak deconvolution procedure described in Section 6.3 for high-fluence data. Repeating the same analysis, we extracted the phonon temperatures and peak shifts as a function of the pump-probe delay, and fitted the resulting dynamics using the model function 6.2. The extracted time constants for all three fluence values are reported in Table 6.2.

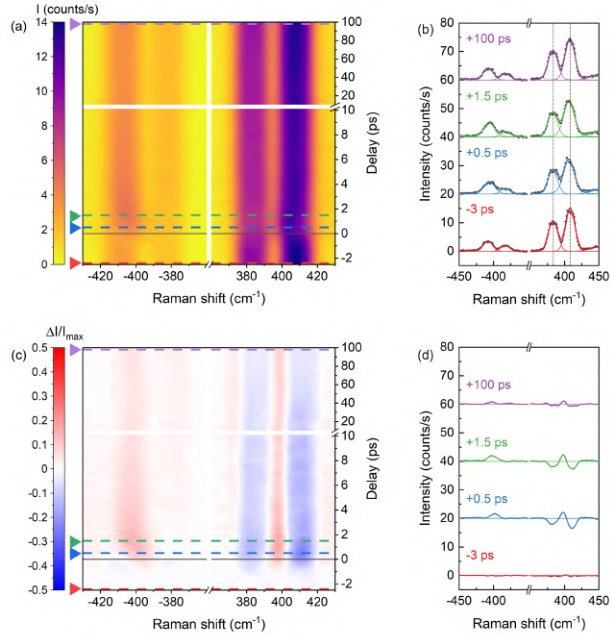

Figure 6.12: Time-resolved Raman scattering spectra and differences for bulk MoS_2 with 5 mJ/cm^2 pump fluence. (a) Intensity map of the spectra (after a linear background subtraction and a 5-points smoothing) versus pump-probe delay. A and E phonons are clearly visible on both the Stokes (right) and antiStokes (left) sides. Dashed lines mark the selected spectra presented, with their multipeak fitting, in panel (b). (c) Intensity map of the relative intensity variation of the spectra after the pump arrival, obtained subtracting to the spectra the average response at negative delays. Intensity differences are normalized to the maximum intensity in panel (a). (d) Selected difference spectra (same delays as in (b)).

	$\tilde{\nu}_A$			$\tilde{\nu}_E$			T_A			T_E			
	t_0	τ_1	τ_2	t_0	τ_1	τ_2	t_0	τ_1	τ_2	t_0	τ_r	τ_1	τ_2
15 mJ/cm^2	0	2.5	$\gg 500$	0	2.0	$\gg 500$	0.6	5.4	$\gg 500$	0.6	5.5	3.5	$\gg 500$
10 mJ/cm^2	0	2.3	$\gg 500$	0	-	$\gg 500$	0.4	6.3	$\gg 500$	0.4	-	-	$\gg 500$
5 mJ/cm^2	0	2.1	$\gg 500$	0	-	$\gg 500$	0.3	6.6	$\gg 500$	0.3	-	-	$\gg 500$

Table 6.2: Time constants extracted from the fitting of the temporal trends on bulk MoS_2 for different exciting fluences. Time delays are expressed in ps. The t_0 values are obtained as a shared fitting parameter for the two phonon modes, both for the frequencies and the temperatures.

Figure 6.13 shows the phonon frequency shifts for both the A and E modes at each pump fluence. As expected, the magnitude of the shifts decreases with decreasing fluence. However, beyond this general trend, a striking qualitative difference between fluence regimes also emerges. At high fluence, both phonon modes display nearly identical renormalization amplitudes ($\Delta\tilde{\nu}^{max} \sim 5$ cm^{-1}) and similar characteristic decay times (see Table 6.2). In contrast, at lower fluences, the A mode exhibits a significantly larger shift than the E mode. Moreover, the E mode appears to lack the fast decay component entirely, instead displaying a step-like temporal evolution. This behaviour was obtained in the fitting as the limit of function (6.2) when $\delta = 0$, thus the second decay component is lacking, and $\tau_1 \to \infty$. The contrasting behaviour of the two phonon modes becomes even more evident when the frequency shifts are normalized to the value of the excitation fluence, as shown in Figure 6.14. For the A mode, the normalized trends are superimposed almost perfectly, indicating a linear dependence of the renormalization on the pump fluence. Conversely, the E mode shows a clear deviation from linearity at all time delays, most notably exhibiting a strong enhancement of the maximum frequency shift at the highest fluence.

The observation in the high fluence regime of the same phonon softening dynam-

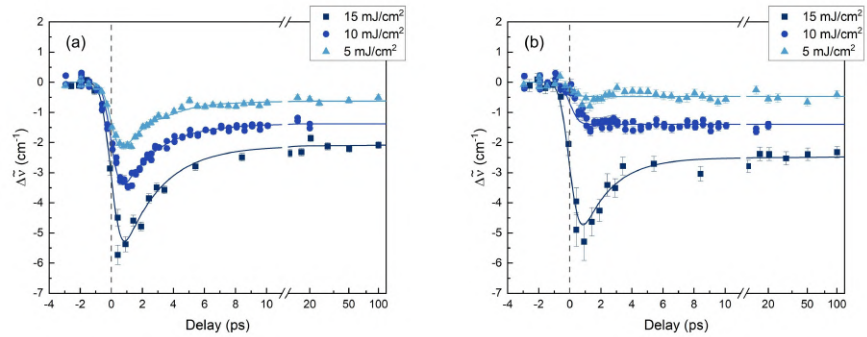

Figure 6.13: Temporal evolution of the phonon frequency shifts as a function of the pump fluence for the (a) A and (b) E modes. Continuous lines display the results of the time trends fittings.

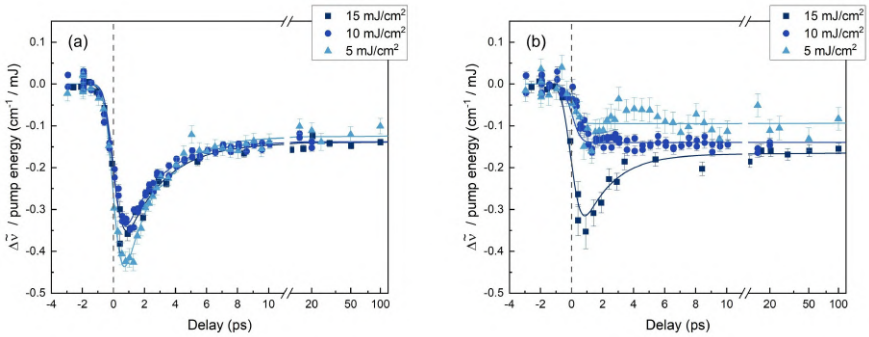

Figure 6.14: Temporal evolution of the phonon frequency shifts normalized on the pump fluence for the (a) A and (b) E modes. Continuous lines display the results of the time trends fittings.

ics for the A and E mode is actually rather unexpected, given their different electron-phonon coupling strengths. This result is also at odds with the available literature: equilibrium measurements on electrostatically doped samples show a much larger redshift for the A phonon compared to the E phonon [82, 84], and theoretical calculations likewise predict a stronger effect of transient photodoping on the A phonon frequencies [86]. However, the described behaviour of the frequency shifts points to the presence of a threshold in the fluence, beyond which the E mode seems greatly affected by the presence of a photoexcited carrier density .

We now turn to the effect of different fluences on the two phonon modes temperatures dynamics, reported in Figure 6.15. Figure 6.16 shows the phonon temperature variation ΔT normalized on the value of the excitation fluence. These data clearly show that the enhanced dynamical population of the A mode, along with the presence of a nonthermal phonon distribution, is maintained at all fluence levels. Moreover, the thermalization timescale of the two modes, determined by the decay constant $\tau_1^{T_A}$ appears largely unaffected by the initial photoexcited carrier density. Small differences can however be noted: for both modes, the normalized phonon temperature variations show a small decrease when increasing the fluence, and the delay between the frequency renor-

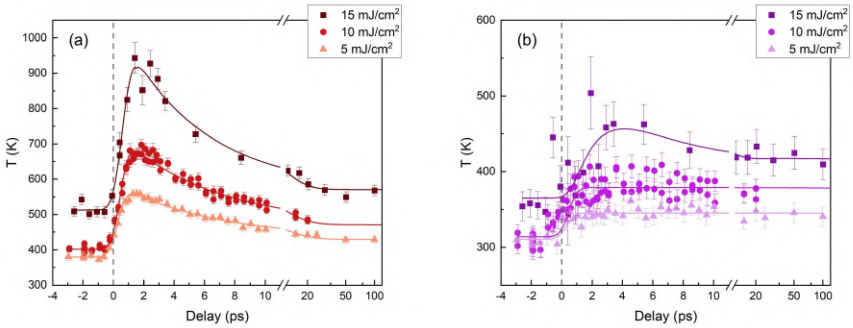

Figure 6.15: Temporal evolution of the phonon temperatures as a function of the pump fluence for the (a) A and (b) E modes. Continuous lines display the results of the time trends fittings.

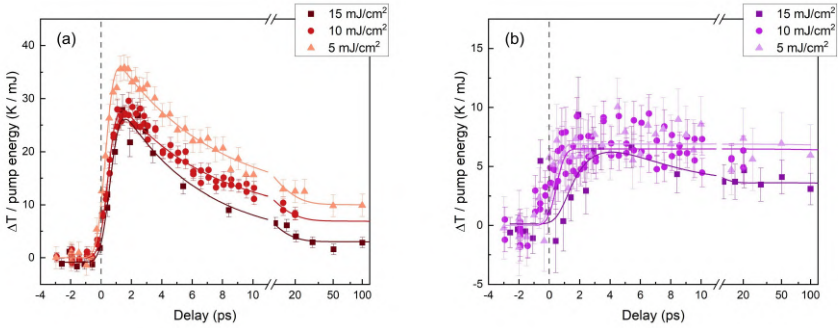

Figure 6.16: Temporal evolution of the variation of phonon temperatures normalized on the pump fluence for the (a) A and (b) E modes. Continuous lines display the results of the time trends fittings.

malization and the rise of the phonon temperatures displays a slight reduction (see Table 6.2). Moreover, the slow rise of T_E is not evident in the low fluence data.

Based on literature values, the excitation fluences used in this study place the system well above the estimated Mott density ($\sim 10^{13}$ cm^{-2} for a MoS_2 1L [112–114]), within a free-carrier regime. In this regime, an increase of the fluence, and consequently of the photoexcited free carrier density, is generally expected to enhance the screening, resulting in a reduction of the electron-phonon coupling strength. As reported by Pan et al. [69], this screening is predicted to be particularly effective for long-wavelength phonons close to the Γ point, leading to a reduced population of these modes and a slower excitation dynamics. This is consistent with our observations on the phonon temperatures: T_A (and, to a minor extent, T_E) increases sub-linearly with fluence, and the population of the two modes is increasingly delayed at higher fluences. The difference in electron-phonon coupling strengths due to the specific symmetry of the two phonon modes, with mode A being a "hot phonon" and mode E being a "cold phonon", seems instead preserved regardless of fluence.

On the other hand, the frequency shift of the E mode exhibits a much more pronounced dependence on fluence, showing a super-linear response to increasing excitation power, and possibly indicating the crossing of a threshold at the highest fluence.

This is also supported by the evolution of the $2LA$ mode, which, at the highest fluence, shows a qualitatively different temporal profile compared to the lower fluence conditions (see Figure 6.17 (a) in the next Section). These findings suggest the presence of distinct phonon renormalization mechanisms that emerge in different doping regimes.

As discussed above, discontinuities in the system response with increasing carrier density may arise from either (i) surpassing the Mott density, beyond which excitons dissociate into free carriers, or (ii) the population of different valleys in the BZ, leading to an abrupt change in the Fermi surface, *i.e.* a so-called Lifshitz transition. Although the estimated Mott densities place it below all the fluence values used here, the fact that this transition is still poorly explored in bulk systems and under non-equilibrium conditions prevents us from fully ruling out the first scenario. However, if a transition from exciton to free carrier regimes does occur, it would be expected to enhance screening efficiency and thereby suppress the degree of phonon renormalization. Nonetheless, resonant Raman scattering measurements have shown that excitons couple to the phonon modes in a highly symmetry-dependent manner, with mode A coupling predominantly to A and B excitons, and mode E being sensitive to the C exciton, in which the electrons have both Mo d_{z^2} and S p_x, p_y (in-plane) orbital character [74]. In this context, a transition from an excitonic to a free-carrier regime could relax symmetry constraints on the coupling, potentially leading to more similar dynamics of the two phonon modes.

Even considering all the explored fluences as lying outside the excitonic regime, the stronger coupling of the E mode with electronic orbitals with in-plane components could underlie the observed differences. Indeed the strong electron-phonon coupling of the A mode is thought to be rooted in the specific band modulation induced by the A phonon near the conduction band minima. Carrier injection into regions of the conduction band far from these minima, as expected for strong photodoping, may enhance the carrier-induced renormalization of the E phonon and reduce the contrast between the two modes.

How this reconciles with the lack of a significant increase of T_E, signalling that the creation of E-symmetry phonons remains a marginal channel for electronic de-excitation, remains an open question. To deepen our understanding of the phenomenon and explore its generality, we plan on extending our study to other TMDs, such as WS_2. Given its analogous structure but different valley energy separations and exciton binding energies, WS_2 may provide critical insight into the interplay between symmetry, band structure, and phonon dynamics, helping to reach a comprehensive interpretation of the current observations.

Moreover, a direct characterization of the photoexcited electron population at different fluences (for instance through time-resolved reflectivity or time- and angle-resolved photoemission measurements) would be desirable, as it could directly identify the transition between distinct photodoping regime.

6.8 Strongly coupled longitudinal acoustic phonons

As a final point, we now discuss the response of the Raman peak observed at ~ 450 cm^{-1} to the system photoexcitation. As mentioned in Section 6.2, this peak arises from second-order Raman processes involving the simultaneous creation/annihilation of two phonons. Its broad linewidth, larger than the experimental resolution, is justified by the presence of multiple spectral components, as revealed by resonant Raman measurements [62]. The assignment of these components is nontrivial, due to the large overlap

of the peaks and the dependence of their relative intensities on the probe photon energy. The dominant contribution is generally attributed to the creation of two longitudinal acoustic ($2LA$) phonons with wavevectors either $q = \pm K$ or $q = \pm M$. Since the two are nearly degenerate in energy, distinguishing between them is challenging. Although resonant Raman measurements at different energies suggest a predominance of the $2LA(K)$ component with a $513\ \mathrm{nm}$ probe, this assignment may not hold under out-of-equilibrium conditions [74].

As discussed in Chapter 2, second-order Raman processes provide access to phonons with wavevectors far from the centre of the BZ, including acoustic modes. This is particularly relevant in MoS_2 and TMDs, where acoustic phonons, and especially the LA mode at the K, M, or Q points, are believed to mediate inter-valley scattering processes [74, 86, 115]. Furthermore, electron scattering experiments [69] suggest that electronic relaxation in these materials proceeds primarily via the creation of acoustic phonons in the early stages, with optical phonons being populated at later times. This contrasts with the canonical picture in which optical phonons are more strongly coupled to electronic excitations and acoustic phonons are generated subsequently via phonon–phonon scattering.

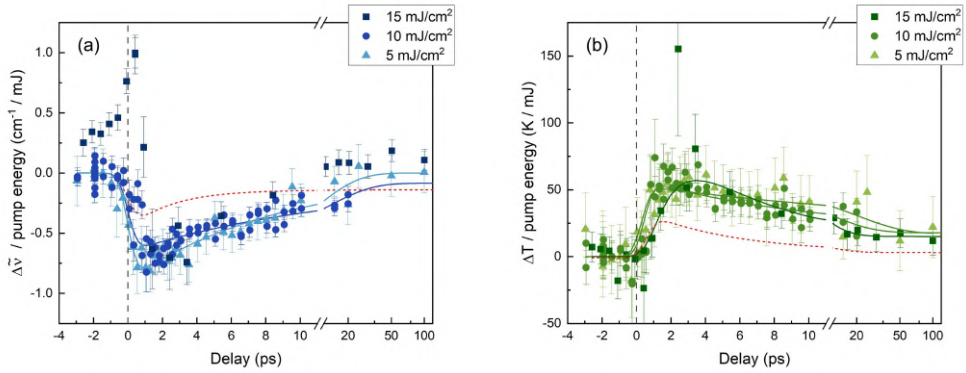

Figure 6.17: Temporal evolution of (a) the phonon frequency shift and (b) the variation phonon temperature of the LA mode. Data are normalized on the pump fluence. Continuous lines display the results of the time trends fittings. Dashed red lines mark the result obtained from the fit of the temporal evolution of the same quantities for the A mode with $15\ \mathrm{mJ/cm^2}$ fluence.

To investigate this behaviour, we extracted from the multipeak fitting of our data both the frequency renormalization and the effective phonon temperature of the two-phonon peak. The latter was obtained with a modification of Equation 6.1 appropriate for second-order Raman processes involving two identical phonons (see Chapter 2). The obtained values, normalized on the pump fluences, are reported in Figure 6.17 along with the result of the corresponding fit with function 6.2. In the trends obtained from the high-fluence dataset, some points are clearly outliers (originating from a low intensity of the antiStokes peak compared with the background) and were excluded from the fitting. The time constants extracted from the fitting are reported in Table 6.3.

From the trends reported in 6.17 (a), it is evident that the $2LA$ phonon peak undergoes at positive delays a strong frequency renormalization, almost twice as large as that observed for the two optical modes at the highest pump fluence. The pronounced response of the acoustic mode to photoexcitation is further confirmed by the temperature

	$\tilde{\nu}_2$			T_2			
	t_0	τ_1	τ_2	t_0	τ_r	τ_1	τ_2
15 $\mathrm{mJ/cm^2}$	-	-	-	0.6	2.1	4.6	$\gg 500$
10 $\mathrm{mJ/cm^2}$	0	12	$\gg 500$	0.4	-	10.3	$\gg 500$
5 $\mathrm{mJ/cm^2}$	0	8.9	-	0.3	-	20	$\gg 500$

Table 6.3: Time constants extracted from the fitting of the temporal trends on the $2LA$ peak for different exciting fluences. Time delays are expressed in ps.

trends in panel (b): at positive delays the LA phonon population has a remarkable increase, again nearly double that of the A mode. Notably, as for the A mode, the absolute values T of the temperature extracted at negative delays and in absence of the pump are significantly higher than room temperature, in the range $500 - 700$ K (data shown in Appendix A.5). Altogether, these observations indicate a strong coupling of the electrons with the LA modes, overcoming the one with zone-centre optical modes. This is consistent with the predictions of Caruso [108] and Girotto et al. [86], which foresee a strong photoinduced population of zone-edge LA phonon and the renormalization of their frequencies of several tens of $\mathrm{cm^{-1}}$ in 1L MoS_2. At the highest fluence, the LA mode appears to be populated faster than the E mode, but with a slight delay with respect to the A mode. This seems at odds with the results of Pan et al. [69], arguing that optical phonons in Γ are populated with a delay of several ps with respect to the zone-edge acoustic modes, but their electron diffuse scattering measurement are little sensitive to the phonon modes inducing out-of-plane modulations (like the A mode) [68]. Thus the electronic de-excitation pathways are likely not determined just by the phonons momentum or their symmetry, but rather by a complex combination of the two properties.

The temporal evolution of the two-phonon peak also reveals further differences between excitation fluence regimes. As shown by the overlap of the trends in Figure 6.17 (b), the LA phonon temperature displays a linear increase with the fluence. However, similarly to the A and E phonons, its rise is progressively delayed from t_0. For the two optical phonons, such behaviour can be explained by an enhanced carrier screening, which, however, should be less effective for zone-edge modes [69]. The frequency renormalization displays instead a more complex behaviour. Its onset is progressively delayed from t_0 (defined from the A and E mode frequency shifts), and at the highest fluence it exhibits a clear non-monotonic evolution with pump-probe delay, displaying and initial hardening of the peak followed by softening after ~ 1 ps. It should be noted that, given the composite nature of the $2LA$ peak, this non-monotonicity could arise from changes in the relative spectral weights of different components, rather than from a proper shift of their phonon energies. While the magnitude of the peak softening scales linearly with the fluence, the overall trend of the frequency shift suggests the existence of a fluence threshold above which photodoping induces a qualitatively different renormalization behaviour. Combined with the results presented in the previous section, this points to the presence of different screening and/or electron-phonon coupling regimes accessible at different excitation fluences, definitively worth of further investigations.

CHAPTER 7

Phonon dynamics across the Verwey transition in magnetite

This chapter presents the experimental investigation carried out on magnetite, a strongly correlated material whose physics is dominated by the complex interplay between structural, electronic, and magnetic degrees of freedom, giving rise to the metal-insulator and structural Verwey transition. By combining temperature-dependent and pump-probe Raman measurements in the low-temperature phase, we are able to detect a photoinduced lattice-symmetry change mimicking the Verwey transition. The ability of TRRS to simultaneously probe different degrees of freedom allows to reveal a dynamical decoupling between structural distortions, phonon spectral anomalies, and the excitation of different phononic and electronic modes. These results provide new insight into phonon dynamic processes associated with the Verwey transition.

7.1 Overview

Magnetite (Fe_3O_4) is the oldest known magnetic material, and yet, despite decades of research, it continues to stand out as a remarkably complex and puzzling condensed matter system. Like many strongly correlated oxides, its ground state is shaped by the intricate interplay between electronic and lattice degrees of freedom, making even seemingly basic questions - such as whether magnetite should be classified as a semiconductor or a semimetal at room temperature, or what mechanism governs its transport properties - difficult to answer [116–118]. Consequently, magnetite has been the subject of extensive experimental and theoretical investigations, and still attracts continuous attention from both a fundamental and an applied perspective.

The most striking manifestation of the competition between electronic correlations and electron–phonon interactions is the so-called Verwey transition. Below a critical temperature of about 120 K, magnetite undergoes a discontinuous change of both the electronic and ionic ordering, which gives rise to a metal-to-insulator transition (MIT) marked by a two order of magnitude increase in the resistivity, and, contextually, a structural distortion that lowers the crystal symmetry from cubic to monoclinic (as shown in Figure 7.1 (a)) [117, 118, 121]. Despite being one of the most studied phase transition in transition metal oxides, the microscopic mechanism underlying its critical dynamics, as well as the nature of the charge and lattice ordering in the two phases are still investigated by researchers. Significant progress has been achieved in the past two decades, allowing to associate the onset of the low-temperature phase with the creation of a coupled charge–lattice long-range ordering, stabilized in a complex arrangement of three-site polarons, known as trimerons (see Figure 7.1 (b)) [122]. Furthermore, in very recent

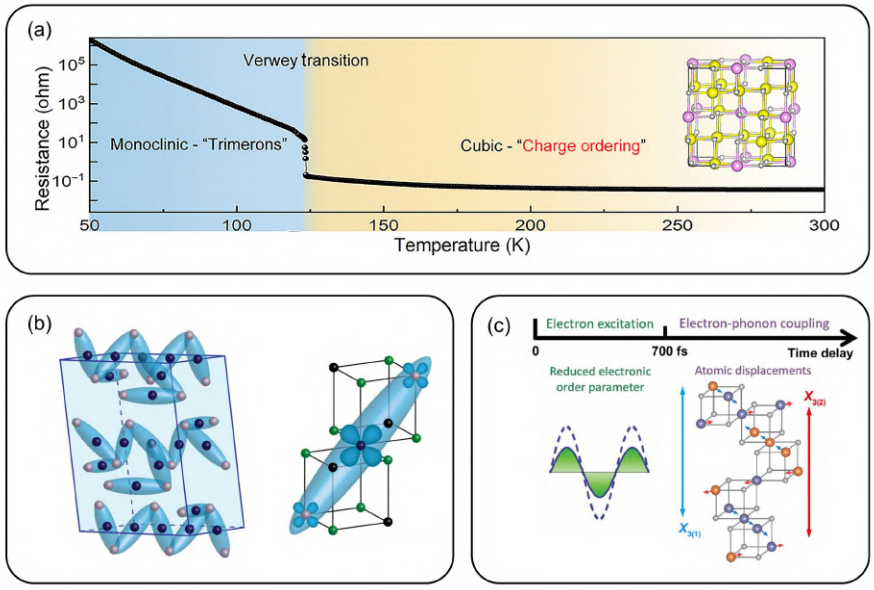

Figure 7.1: Magnetite structural and electronic properties across the Verwey transition. (a) Resistance measurement on magnetite, displaying the characteristic sharp increase corresponding to the Verwey transition at $T_V \sim 123$ K, associated with a change in the lattice symmetry. Adapted from [119]. (b) The three-site polaronic unit (trimeron - right side) and its disposition inside of the unit cell (left side), constituting the charge ordering in the low-temperature monoclinic phase. Blue (grey) sites represent Fe^{2+} (Fe^{3+}) atoms, green sites O atoms. Adapted from [120]. (c) Schematic process of a Verwey transition photoinduced by 1.55 eV photons as observed by pump-probe UED measurements. Adapted from [119].

years, it has been shown that even the high-temperature phase displays charge ordering in the form of unconventional electronic nematicity [119].

Many insights were made possible largely thanks to time-resolved experiments, addressing a photoinduced, non-equilibrium version of the Verwey phase transition (see Figure 7.1 (c)). Ultrafast studies have investigated the dynamics of the photoinduced transition, decoupling on a temporal scale the breakdown of the charge ordering from the modification of the lattice symmetry and the macroscopic MIT [123, 124]. Moreover, they allowed to attribute the stabilization of two ordered phases and the bridging between them through the Verwey transition to the strong electron-phonon coupling with specific low-frequency modes (above all the X_3 transverse-optical mode) [119, 125]. Lastly, it was recently revealed the possibility of either suppressing or reinforcing the monoclinic distortion depending on the photoexcitation energy, thus granting access to hidden metastable phases [126].

There is thus a clear motivation to investigate phonon populations and their dynamical evolution across the Verwey transition. So far, this has been explored only indirectly, with ultrafast electron and x-ray diffraction studies tracking lattice distortions associated with specific modes. Time-resolved Raman spectroscopy instead offers a more direct probe of these dynamics.

Raman spectrum of magnetite across the Verwey transition

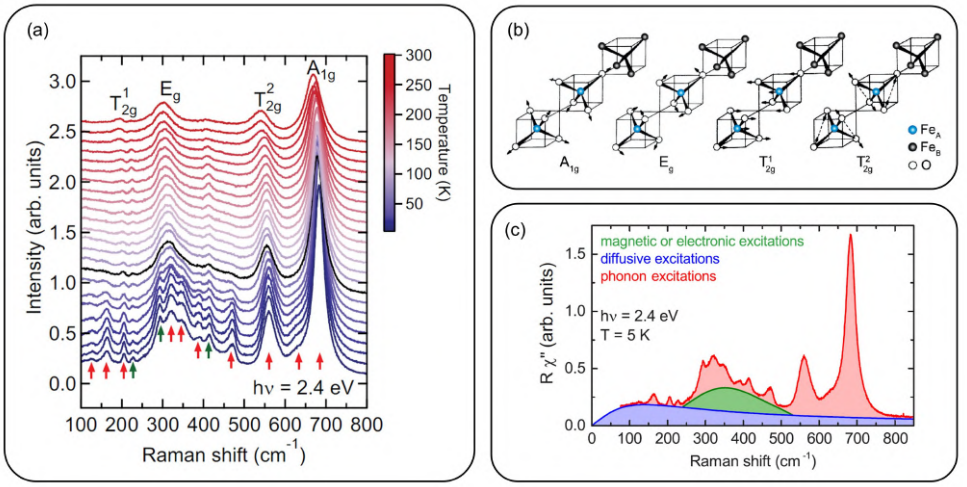

Figure 7.2: Raman spectroscopy study of magnetite. (a) Raman spectra as a function of temperature for 2.4 eV excitation. Red (Green) arrows indicate magnetite (hematite) phonon modes in the monoclinic phase. Black color denotes the spectrum at the Verwey transition (occurring here at a seemingly lower temperature due to laser heating). (b) Pictorial representation of the normal vibrations induced in the primitive cell of magnetite by the four Raman-active modes clearly visible in the spectra. (c) Pictorial representation of the different contributions to the Raman response function of magnetite from phonons, magnons and electrons. All panels are adapted from [127] and [128].

The Raman spectrum of magnetite as a function of temperature, measured by Borroni et al. [127] with a 2.4 eV CW probe, is reported in Figure 7.2 (a). At room temperature four main peaks are visible, which, according to the assignment of Shebanova and Lazor [129] correspond to the T^1_{2g} ($\sim 193\ \mathrm{cm}^{-1}$), E_g ($\sim 306\ \mathrm{cm}^{-1}$), T^2_{2g} ($\sim 540\ \mathrm{cm}^{-1}$), A_{1g} ($\sim 670\ \mathrm{cm}^{-1}$) phonon modes, associated with the normal vibrations of the unit cell illustrated in Figure 7.2 (b). A fifth Raman-active phonon of T_{2g} symmetry is expected from calculations, but it has not been unambiguously identified experimentally.

Upon the cooling of the sample, the Raman spectrum undergoes significant modifications beyond the typical hardening of the phonon frequencies and narrowing of their linewidths. Indeed, the monoclinic distortion leads to a four-fold increase in the dimension of the unit cell and a corresponding folding of the Brillouin zone (BZ), which results in a quadruplication of the normal modes of vibration. The resulting phonon spectrum is thus of remarkable complexity [130]. New modes appear at 125, 160, 470, and 628 cm^{-1} and in the 300-400 cm^{-1} frequency range. Among these, the features at 160 and 470 cm^{-1} display a temperature dependence resembling a partial phonon softening when approaching the Verwey transition from a lower temperature, as well as lineshape anomalies, suggesting a particularly strong coupling to the electronic degrees of freedom. While the former is attributed to the folding to the BZ center of a phonon of Δ_2 symmetry, the latter remains unassigned to a specific mode or symmetry [127].

The Verwey transition has therefore a clear manifestation in the Raman response. Besides the new modes, the temperature dependence of the frequency and linewidth of the

A_{1g} phonon, present in both phases, also show anomalies at the transition temperature [127, 131, 132].

Beyond the phonon features, the spectral lineshape is also influenced by additional contributions. In particular, a background arising from diffusive electronic excitations and a broad mode centered between 300 and 500 cm^{-1}, attributed to either electronic or magnonic origins [133], significantly shape the overall Raman response, as schematically illustrated in Figure 7.2 (c). Both contibutions depend on the temperature and display significant variations at the Verwey transition [127].

7.2 Temperature dependent measurements

7.2.1 Experimental

A 1μm-thick magnetite film oriented along the (001) crystallographic direction was grown by pulsed laser deposition on a MgO substrate at the APE-NFFA laboratory [134]. The thickness was chosen to guarantee bulk-like behavior (thinner films can display a broadened or no structural transition [135]) and to ensure sufficient Raman signal, given the relatively large penetration depth of optical radiation inside the sample ($\sim 0.5\ \mu\mathrm{m}$).

The Raman spectrum as a function of temperature was measured using the continuous-wave (CW) 532 nm laser with an average power of 2.5 mW. The CW source was preferred to the pulsed ones for equilibrium measurements because of its narrower linewidth and the possibility to employ higher average power (thus achieving a higher signal-to-noise ratio) without risking damaging the sample. Temperature control was provided by the cryogenic system described in Chapter 4.

Because of the need for realignment of manipulator upon changing temperature, and since these measurements were performed before the implementation of stability improvements for the operation with the cryostat, the absolute intensities of the spectra collected at different temperatures are not directly comparable. All spectra were therefore normalized to their integrated intensity over the full measured spectral range prior to the analysis. Finally, the employed notch filter limited the accessible spectral window to Raman shifts above 340 cm^{-1}.

7.2.2 Results and marker of the Verwey transition

The results of temperature-dependent measurements are summarized in Figure 7.3. The Raman spectra, shown in the top part of panel (a), exhibit a behavior consistent with the one reported by Borroni et al. [127], namely a frequency shift and narrowing of the phonons present in the cubic phase (T_{2g}^2 and A_{1g}), together with the appearance of additional peaks at $T \sim 120$ K. As highlighted in the bottom part of panel (a), which displays the difference spectra with respect to the one obtained at 80 K, this evolution is accompanied by a pronounced modification of the background below 550 cm^{-1}. This reflects both an reduction and a redistribution of the spectral weight in the electronic background and of the broad electronic or magnonic feature indicated in green in Figure 7.2 (c).

Among the new phonon modes emerging at low temperature, the 470 cm^{-1} peak (identified by Borroni et al. as exhibiting critical behaviour) was the most intense and was therefore selected as a marker of the structural phase transition. The limited accessible low-frequency spectral range, however, complicates the subtraction of the underlying electronic/magnonic background, whose strongly temperature-dependent shape

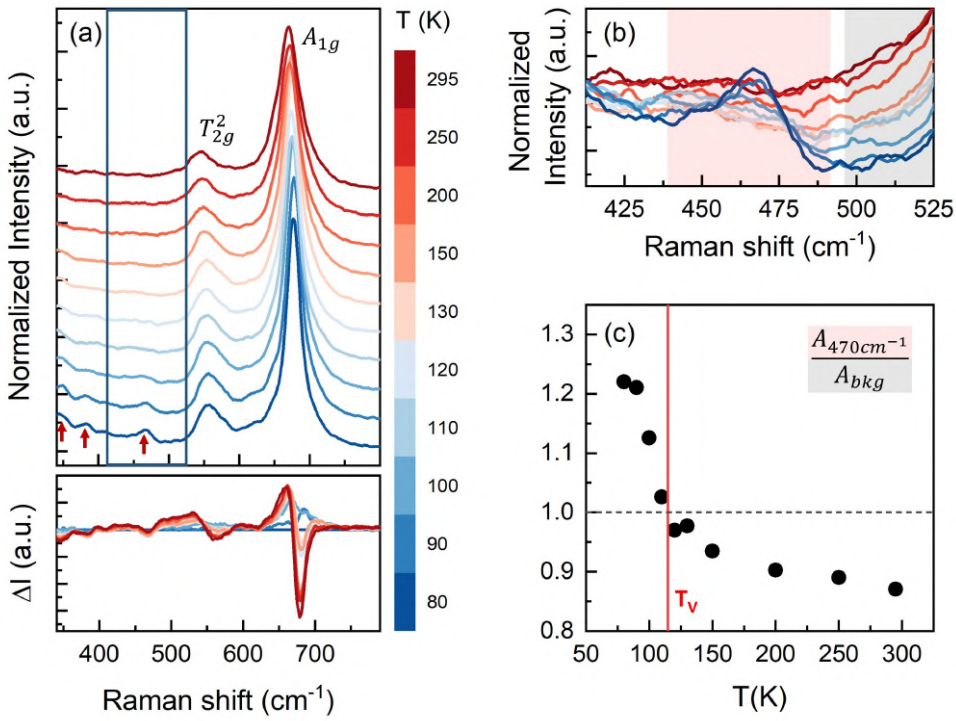

Figure 7.3: Temperature-dependent Raman measurements on magnetite with a 532 nm (2.33 eV) CW laser. (a) Raman spectra as a function of temperature, vertically shifted for clarity. Spectra are shown after a 7-point smoothing and the normalization on the integrated intensity of the whole spectrum. Red arrows indicate phonon modes appearing in the monoclinic phase. Bottom panel: difference between the spectra and the spectrum at 80 K. (b) Raman spectra as a function of temperature in the frequency range around the mode at 470 cm^{-1} (shown as a blue rectangle in panel (a)). Pink and grey area mark the region integrated to extract a marker of the Verwey phase transition (see text). (c) Temperature trend of the marker of the phase transition extracted from the ratio of the two integrated areas. The value 1 of the marker corresponds to the Verwey transition, found at a temperature of ~ 115 K (marked by a red line).

and intensity make this step critical for a reliable peak fit. This aspect is even more relevant in the pump-probe data presented in the next section, due to lower signal-to-noise ratio. To circumvent this issue, the marker of the phase transition was thus defined as the ratio between the integrated spectral weight of the 470 cm^{-1} mode (435–490 cm^{-1}) and that of the immediately adjacent background (495–525 cm^{-1}), as illustrated in Figure 7.3 (b). The integrated areas were normalized to the width of the corresponding spectral range.

The temperature trend of the extracted marker is reported in Figure 7.3 (c). Given that the disappearance of the peak corresponds to $\frac{A_{470cm^{-1}}}{A_{bkg}} \approx 1$, the marker allows us to identify the Verwey transition temperature between 110 and 120 K. We therefore consider $T_V = 115 \pm 5$ K, in agreement with the values reported in literature [117, 118, 127].

The reliability of the identification of the Verwey transition is further supported by

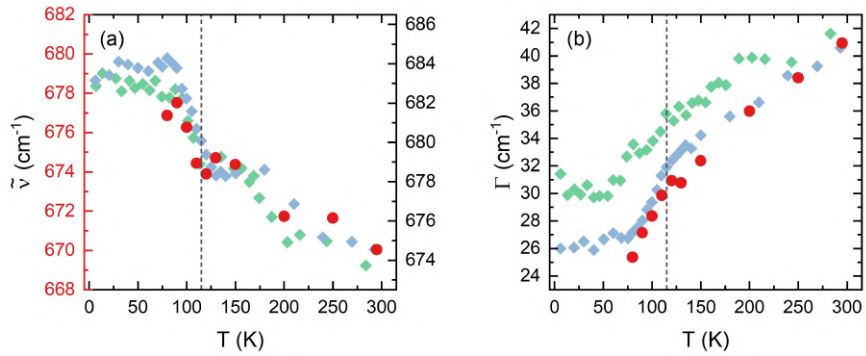

Figure 7.4: Temperature dependence of the (a) frequency and (b) linewidth of the A_{1g} mode. The results of the measurements presented in this thesis are shown as red dots. Violet and green symbols mark the results of Borroni et al. [127], obtained with 3.1 eV and 2.4 eV excitation respectively. A vertical dashed line denotes the Verwey temperature T_{V}.

the temperature dependence of the frequency and linewidth of the A_{1g} phonon, extracted from a Voigtian fit of the spectra. As shown in Figure 7.4, the results are in good agreement with those reported by Borroni et al. [127], displaying the same anomalies (*i.e.* changes in the trend slope) at the same transition temperature T_{V}. Sample-dependent variations of a few cm^{-1} in the phonon frequencies are commonly reported across different magnetite studies, which accounts for the $\sim 4\ \mathrm{cm}^{-1}$ offset observed between the two datasets.

7.3 Time-resolved measurements

7.3.1 Experimental

To investigate the dynamical evolution of the phonon degrees of freedom across the observed Verwey transition, we performed a pump–probe Raman experiment on the same magnetite sample, maintained at a temperature of ~ 83 K, well within the monoclinic phase. The system was brought out of equilibrium by 633 nm pump pulses ($\Delta t = 0.3$ ps) and probed by 513 nm pulses ($\Delta t = 1$ ps, yielding an overall temporal resolution of 1.1 ps from the pump–probe cross-correlation). The employed fluences were $F = 5.6$ $\mathrm{mJ/cm}^2$ and $F = 1.9\ \mathrm{mJ/cm}^2$ for the pump and probe respectively.

Two datasets were collected on consecutive days: the first (herein termed dataset 1) tracking the dynamics up to 50 ps, and the second (dataset 2) focusing on the near-zero-delay region [–4 ps, +6 ps] with finer temporal steps.

During the measurements, small temperature drifts (3–4 K) were observed but they did not seem to significantly affect either the Raman spectrum of the sample or its pump-induced response. This and other effects of instabilities of the experimental conditions were controlled and minimized by repeating short acquisitions that were later summed during analysis, and by recording a negative-delay reference spectrum every 4–5 acquisitions.

7.3.2 Result overview

The results of the TRRS experiment are shown in Figure 7.5 for the dataset 1. The top panels present the antiStokes and Stokes spectra (panels (a) e (c), respectively) at three selected pump-probe delays, while the bottom panels display the difference spectra relative to the average spectrum acquired at negative delays (*i.e.* prior to the pump arrival).

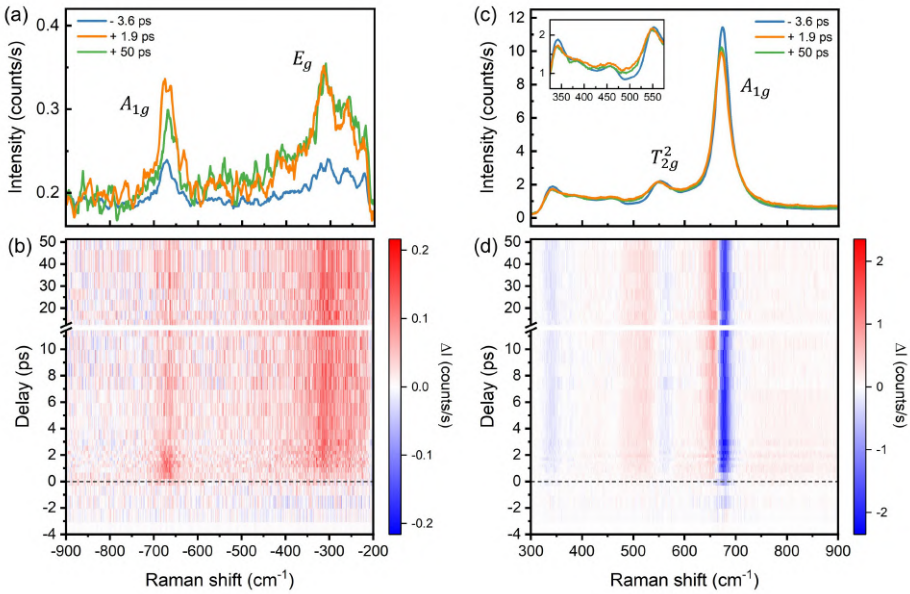

Figure 7.5: Time-resolved Raman scattering measurements on magnetite at 83 K. (a) antiStokes and (c) Stokes spectra at selected pump-probe delays after a 7-points smoothing. (b,d) Differences of the spectra with the average response at negative delays ($\Delta t = t_{pump} - t_{probe} < -1$ ps), displayed as an intensity map.

On the Stokes side, the Raman spectrum obtained with a 513 nm probe has essentially the same structure as that measured with the 532 nm CW laser, displaying only a slight broadening due to the larger spectral width of the pulsed excitation. On the antiStokes side, the A_{1g} phonon is clearly visible, as is the E_g mode, which only on this side of the spectrum lies within the accessible spectral region due to the asymmetric notch filtering. We can notice that the antiStokes peaks are already present at negative delays, even though, based on the Stokes intensity and detailed balance at 83 K, they should lie below the background noise level. Indeed, as shown in Appendix B.1, they are not observed with the 532 nm CW probe at the same temperature. As discussed in Chapter 3, this effect arises from the use of a pulsed probe and signals that the system is measured in presence of a small additional phonon population created by the probe itself. This, together with the broader spectral width and the lower average power, could underlie the slightly reduced visibility of the peaks of the monoclinic phase (shown in the inset of panel (c)) with respect to the CW measurements.

The spectra in panel (a) and the difference map in panel (b) clearly show that the antiStokes side exhibits a pronounced enhancement of the intensity after photoexcitation, consistent with a pump-induced increase of the population of the observed modes. The

A_{1g} peak is strongly enhanced immediately after the pump-probe coincidence time, before relaxing towards a positive plateau within a few picoseconds. The low-wavenumber region also shows a marked intensity increase that persists throughout the observed time window with no visible reduction, as does the E_g peak, leading to a stronger differential signal at $\sim 310\ \mathrm{cm}^{-1}$. The latter contribution appear to rise with slight delay compared to the others.

On the Stokes side, more complex pump-induced spectral modifications are evident. Both the A_{1g} and T_{2g}^2 modes undergo a redshift and broadening. In the 350-520 cm^{-1} range (inset of panel (c)), both a modification of the background, flattening and increasing especially around 500 cm^{-1}, and a reduction in the intensity of monoclinic-phase peaks can be observed. In particular for the mode at $\sim$ 470 cm^{-1}, this results in an almost constant intensity against an increased background, as visible from the white band between red regions in the difference map. These changes are in close correspondence with those observed across the thermally driven Verwey transition. In addition, the Stokes spectra display a small pump-induced enhancement of the high-wavenumber background ($\tilde{\nu} > 750\ \mathrm{cm}^{-1}$).

None of the observed spectral modifications on either the antiStokes or Stokes side returns fully to equilibrium within the 50 ps time window explored in our experiment.

7.4 Photoinduced phase transition

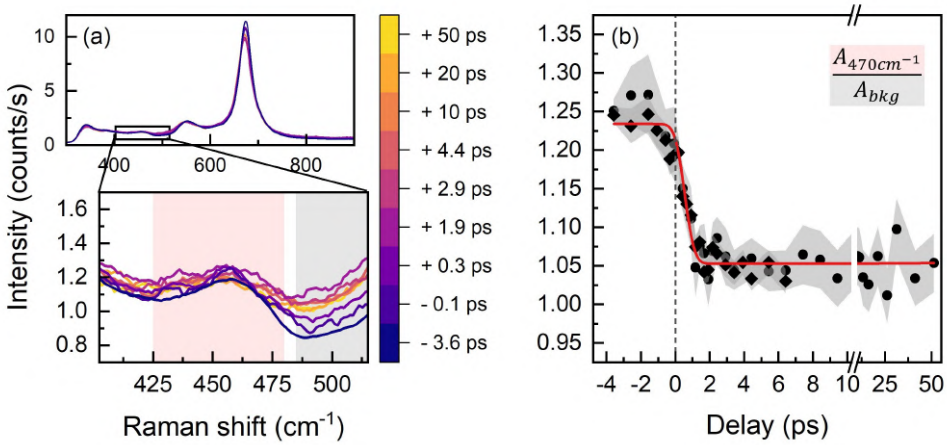

Figure 7.6: Marker of the photoinduced phase transition. (a) Raman spectra at selected pump-probe delays, enlarged in the frequency range around the mode at 470 cm^{-1}. Pink and grey areas mark the regions integrated to extract a marker of the Verwey phase transition (see text). (b) Temporal trend of the marker of the phase transition extracted from the ratio of the two integrated areas. Two types of symbols mark the results obtained from the two independent datasets. A grey region indicates the error at each point, obtained from the standard deviation of the marker across repeated acquisition of the spectrum at –3.6 ps. The result of the fit with a step function is shown as a red line.

To quantitatively analyse the dynamics of the photoinduced phase transition, a marker of the phase transition was extracted from the pump–probe data in the same way as was done for the temperature-dependent measurements, namely from the ratio between the

integrated spectral weight around the 470 cm^{-1} mode (425-480 cm^{-1}) and that of the adjacent background (485-515 cm^{-1}), each normalized to the width of the integration window. The values obtained from the two datasets are reported in Figure 7.6 (b) as a function of pump–probe delay.

As shown in Figure 7.6 (b), the marker exhibits a pronounced step-like decrease after photoexcitation, with no indication of recovery towards the initial value within the measured time window, signalling a strong photoinduced quench of the monoclinic phase. The results obtained from the two datasets are fully consistent within the experimental error (estimated from the standard deviation of repeated acquisitions of the reference spectrum at –3.6 ps) and the trend is well captured by a fit with a step function ($A\theta(t-t_0)+c$), convoluted with a Gaussian accounting for the temporal resolution. The fit was performed on the combined datasets.

From the fit, we extract a marker value at negative delays of 1.23, consistent with the temperature-dependent measurements, and a value of 1.05 at positive delays. The fit also yields the onset time for the transition at of $t_0^{PT} = 0.55 \pm 0.05$ ps. Since the zero-delay time, as routinely done in pump–probe experiments, was adjusted on the fastest response to the pump pulse observed in the system (in this case the increase in intensity of some modes in the antiStokes spectrum, as discussed in Section 7.6), this result highlights a delay between the initial photoexcitation and the quench of the monoclinic phase.

We notice that the marker remains above 1 at positive pump-probe delays, which would suggest a residual presence of the critical phonon mode and therefore an incomplete phase transition. However, the temporal profile points to the rapid establishment of a metastable phase, a scenario consistent with a complete phase transition. This aspect will be further discussed in Section 7.7.

7.5 Evolution of the A_{1g} mode

To map the photoinduced evolution of the A_{1g} mode, which, as mentioned above, exhibits a clear broadening and a shift towards lower energies, the peak was fitted with a Lorentzian lineshape convoluted with a Gaussian with FWHM $= 15$ cm^{-1}, corresponding to the spectral width of the pulsed probe. The fit was performed only on the spectral region above 635 cm^{-1}, as shown in Figure 7.7 (a). Indeed, while a global fit of the entire spectrum as a function of pump–probe delay would in principle be more desirable, it would require a modelling the delay-dependent electronic/magnonic background, which is difficult to achieve reliably without access to wavenumbers below 350 cm^{-1} [127]. Given the much higher intensity of the A_{1g} peak relative to the other modes and the absence of spectral features at higher energies, restricting the fit to this limited spectral window is not expected to significantly affect the results.

The obtained variations of the A_{1g} phonon energy and linewidth are reported in Figure 7.7 (b) and (c) as a function of the pump-probe delay. The plotted values represent the difference between the fitted parameters and their average at negative delays ($\Delta t < -1$ ps). The values extracted from the two datasets are perfectly consistent, showing a redshift of approximately 2 cm^{-1} and a linewidth broadening of about 4 cm^{-1} after photoexcitation, without any recovery towards the initial values within the 50 ps time window. Both variations are comparable in magnitude to those observed in the temperature-dependent data between 80–90 K and 110-120 K, *i.e.* close to the Verwey transition (Figure 7.4).

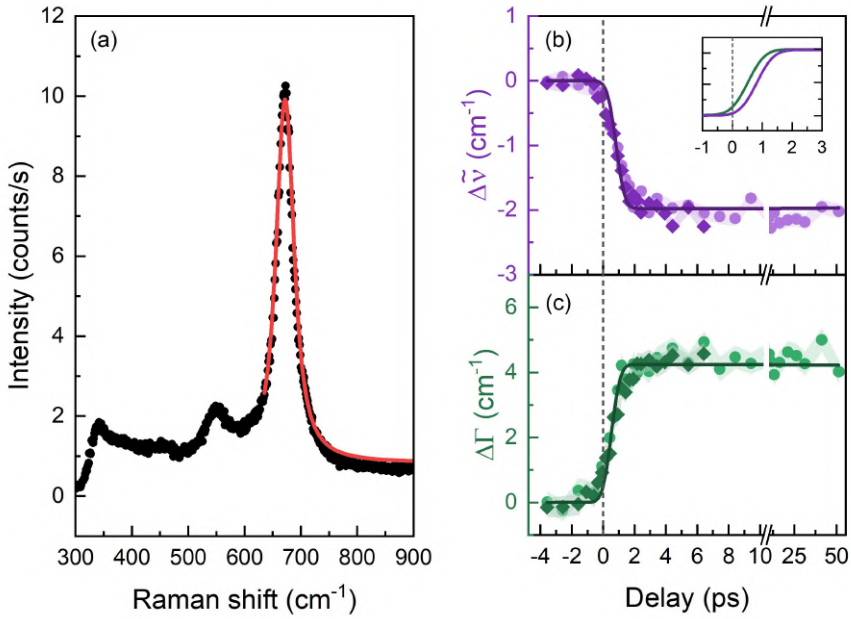

Figure 7.7: Temporal evolution of the A_{1g} phonon mode. (a) Example of the fit performed on the A_{1g} peak of the Stokes spectrum. The result of the fit with a Lorentzian lineshape convolved with a Gaussian accounting for the probe spectral width is shown as a red line superimposed to the data. The fit was performed on the spectral region above 635 cm^{-1}. (b,c) Temporal evolution of the frequency shift and linewidth broadening. Two types of symbols mark the results obtained from the two independent datasets. Shadowed regions indicate the error at each point. The results of the fit of the trends with step functions are shown as solid lines. In the inset, the fitting results are compared (in absolute value and normalised to the maximum), evidencing a clear delay between the rise of the two quantities.

Interestingly, the onset of these spectral changes is not simultaneous. A fit of the two trends with a step function analogous to the one described in the previous section allows to retrieve onset times of $t_0^{\Delta\tilde{\nu}} = 0.82 \pm 0.04$ ps for the energy shift and $t_0^{\Delta\Gamma} = 0.52 \pm 0.04$ ps for the broadening, revealing a delay of about 300 fs between the two processes (see inset of Figure 7.7 (b)). Further insights into the origin of this delay can be obtained by comparing these onset times with those of the other pump-induced spectral modifications, as discussed in Section 7.7.

Lastly, it can be noticed that at long delays the experimental points seem to trend away from the flat plateau assumed by the step-function model. This suggests the presence of a slow, residual evolution of both the redshift and the broadening.

7.6 Phonon populations dynamics

In order to extract the temporal evolution of the phonon populations, the antiStokes spectra were fitted using three Lorentzian peaks (convolved, as done for the A_{1g} Stokes peak, with a Gaussian of fixed width providing the probe spectral resolution), corresponding to the A_{1g} and E_g phonons, and to the broad feature observed at wavenumbers

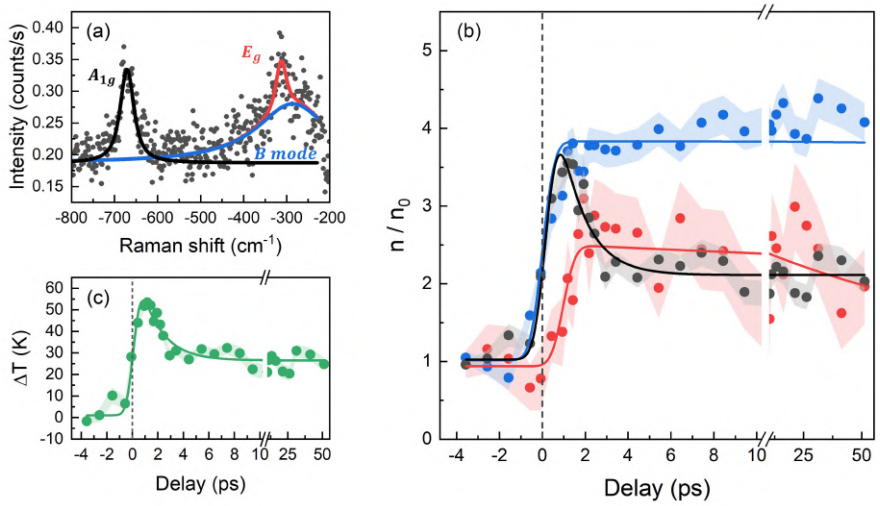

Figure 7.8: Temporal trends of the phonon population. (a) Example of the fit performed on the antiStokes spectra. The three components corresponding to the A_{1g} and E_g phonon modes and to the "B" mode (electronic/magnonic excitations) are shown with black, red and blu solid lines respectively. (b) Temporal dependence of the variation of the phonon population extracted from the antiStokes intensities (see text), plotted in the same color code as panel (a). Shadowed regions indicate the error at each point. (c) Equivalent phonon temperature of the A_{1g} mode extracted from the antiStokes/Stokes intensity ratio. In (b) and (c) only results obtained from dataset 1 are shown.

below $450\ \mathrm{cm}^{-1}$, hereafter referred to as the "B" mode.

Given the low signal-to-noise ratio of the antiStokes measurements, several constraints were imposed during the fitting procedure. Specifically, the frequency and linewidth of the A_{1g} mode at each pump-probe delay were fixed to the values obtained from the corresponding Stokes spectrum. The central frequency of the broad B mode was kept at a fixed distance of $385\ \mathrm{cm}^{-1}$ from the A_{1g} peak, while the frequency separation between the A_{1g} and E_g peaks, as well as the linewidth of the E_g were left as free fitting parameters but constrained to remain constant across all delays. Under these conditions, the peak areas were left as the only delay-dependent free fitting parameters.

As shown for the other case studies, the phonon population at a given pump-probe delay can be retrieved from the antiStokes/Stokes intensity ratio $\frac{I_{AS}(t)}{I_S(t)}$ (see equation 3.1 in Chapter 3). In the present case, however, this method can only be applied to the A_{1g} mode, since both the E_g mode and B modes lie outside the accessible spectral range on the Stokes side of the spectrum. Nevertheless, from equation 2.24 the relative variation of the phonon population at positive delays can be directly determined from the antiStokes spectrum alone, according to:

$$\frac{I_{AS}(t)}{I_{AS\,0}} = \frac{C'\chi^2(t)n(t)}{C'_0\chi^2_0 n_0} \approx \frac{n(t)}{n_0} \tag{7.1}$$

where the label 0 marks quantities obtained at negative delays and the second equality is valid provided that the factors C' (containing all the optical constants appearing in the

Raman cross section) and χ^2 (the bilinear product of the Raman tensor and the polarization vectors) do not display a strong dependence on the pump-probe delay. The latter assumption was verified for the A_{1g} mode, by comparing the values of $\frac{n(t)}{n_0}$ obtained from equation 7.1 with those obtained from the standard formula involving both Stokes and antiStokes intensities (equation 3.1), as shown in Appendix B.2. Since C' and χ^2 are only weakly dependent on the frequency, the result can be extended to the E_g and B modes as well.

The $n(t)/n_0$ values obtained from the fitted areas of the three modes are presented in Figure 7.8 as a function of pump-probe delay. For clarity, only the results from dataset 1 are shown. The data reveal distinct behaviours of the three modes: the population of the A_{1g} and B modes exhibit a prompt and nearly simultaneous rise immediately after photoexcitation, whereas the E_g phonon population increases only after a certain delay. Moreover, the two phonon modes display qualitatively different temporal evolution of the population, with the one of the A_{1g} mode rising sharply and then decaying exponentially towards a plateau, and the one of the E_g mode undergoing an almost step-like increase with little to no subsequent decay. The population variations obtained from dataset 2 follow the same dynamics, with only minor differences in the values, and are reported in Appendix B.2. To quantify these observations, the temporal traces were fitted with the function:

$$f(t) = \alpha\, \theta(t - t_0)(e^{-(t-t_0)/\tau} + C) + f_0 \tag{7.2}$$

where t_0 represents the onset of the variation, τ a characteristic decay time, C the relative weight of a long-delay plateau and f_0 the value at negative delays (left as a free parameter, but converging to unity within error for all fitted trends). In the limit $\tau \to \infty$, $f(t)$ reduces to a step function. $f(t)$ was convolved with a Gaussian to account for the finite temporal resolution.

A global fit of the trends from the two datasets was performed, with shared t_0 and τ for each mode. The resulting time constants are reported in Table 7.1. Since the population of the B mode displays the fastest response to the pump among all the spectral changes observed in the experiment, the zero-delay time was set to the onset of its increase.

	t_0 (ps)	τ (ps)
A_{1g}	0.21 ± 0.05	1.2 ± 0.2
E_g	0.97 ± 0.14	122 ± 80
B mode	0 ± 0.06	-

Table 7.1: Characteristic time constants extracted from the fit of the phonon population dynamics. t_0 values are given with respect to the onset of the B mode population variation, which displays the fastest response to the pump observed in the experiment.

The fit reveals a slight delay between the rise of the B mode and that of the A_{1g} mode, and a delay of 1 ps for the E_g mode.

Considering that the B mode is generally assigned to an electronic or magnonic excitation, the observed temporal trends suggest the following picture: the system first responds to photoexcitation through the electronic subsystem, as reflected in the rise of the B mode population. Shortly after, hot phonons strongly coupled to the electronic degrees of freedom are populated (such as the A_{1g} mode), which subsequently decay

via anharmonic phonon–phonon interactions, redistributing the energy to other, more weakly coupled phonon modes. The E_g phonon appears to belong to the latter category, consistent with the fact that its population rises with a delay matching the characteristic time of the fast decay of the A_{1g} phonon population towards its plateau.

Finally, from the A_{1g} population it was possible to estimate the equivalent phonon temperature using equation 3.1. The extracted trend, shown in Figure 7.8 (c), follows the same dynamics as $n(t)/n_0$, with a sharp increase immediately after photoexcitation, followed by a rapid relaxation to a plateau at ~ 25 K above the initial value, which persists for more than 50 ps. Since after several tens of picoseconds it is reasonable to assume that phonons across the BZ have thermalized through anharmonic interactions, this plateau value can be taken as representative of the overall lattice temperature increase.

7.7 Overall dynamics

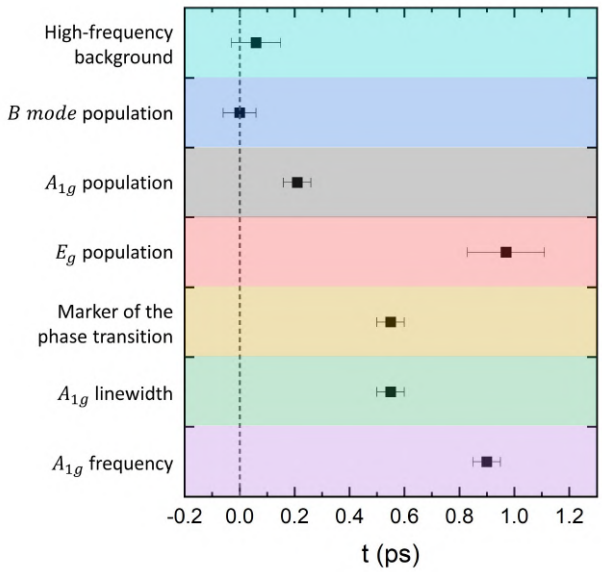

Figure 7.9: Temporal ordering of the pump-induced spectral changes in the Raman spectrum. Data points mark the onset times t_0 extracted from the temporal fit of the variation of the different quantities indicated on the left side of the plot. A dashed line marks the zero-delay time, set on the fastest observed response.

The observation of several distinct, pump-induced spectral changes in the Raman response allows us to compare their respective dynamics and link them to different microscopic processes occurring in the system. In particular, a comparison of the onset of the modifications reveals a clear temporal decoupling: effects that appear simultaneously in temperature-dependent measurements occur at different times following photoexcitation. Figure 7.9 collects the onset times t_0 extracted from the fitted dynamics of the different analysed spectral features. In addition to those discussed in the previous sections, it is here included also the dynamics of the high-wavenumber background (obtained from the integration of the Stokes spectrum), ascribed in the literature to diffusive

electronic scattering [127]. Its temporal dependence, showing a prompt rise and a subsequent decay with $\tau^{bkg} = 7.5 \pm 3.3$ ps, is reported in Appendix B.3. It can be seen how this background rises almost concurrently with the population of the B mode, the other feature associated with electronic degrees or freedom.

The temporal ordering of the observed responses indicates a cascade of processes following photoexcitation, consistent with the following picture. The electrons respond almost instantaneously to photoexcitation, followed by the strongly coupled A_{1g} phonon mode, which is populated following the energy transfer from the electrons within few hundreds of femtoseconds (at the lower limit of the delays measurable with our temporal resolution). The structural phase transition occurs at a later stage, at a delay of more than 500 fs. This is consistent with ultrafast diffraction experiments reported in literature, which show that when inducing a photoinduced Verwey transition, the charge ordering is destroyed within $\sim$ 300 fs from the pump, while structural distortions are detected only later, at $\sim$ 700 fs delay for those associated with X_3-symmetry phonon modes, and after several picoseconds for the Δ_5-symmetry ones [123–125]. We note that while BZ folding brings these modes to the zone centre, making them potentially detectable by Raman spectroscopy, their energies below 15 meV (120 cm^{-1}) put them outside the accesible spectral region in the present experiment [128, 136].

Interestingly, our data indicate that specific optical phonons, such as the A_{1g}, can be populated before the coherent structural distortions characterizing the phase transition are fully established. This suggests the possible presence of an intermediate step in which the incoherent population of strongly coupled phonons mediate the transfer of energy from the electronic subsystem to the modes associated with the structural order parameter. Indeed, while the A_{1g} mode is not directly associated with the Fe atoms involved in the ordered state below T_V, its strong coupling with the Verwey-induced distortion is testified by the anomalies in its frequency and linewidth in both temperature-dependent and time-resolved data [133]. On the other hand, the delayed rise of the E_g population argues against a primary role for this mode in the structural change. We note that the lack of a definite assignment for the critical mode at 470 cm^{-1} prevents us to link it to a specific distortion associated with the phase transition. Nevertheless, the timescale of its quench is comparable to (or slightly faster than) the fastest lattice response observed by diffraction, supporting the conclusion that the increase of the A_{1g} mode population precedes the onset of all coherent lattice distortions.

Figure 7.9 also shows that the changes in the linewidth and frequency of the A_{1g} mode are in temporal correspondence with the structural phase transition and with the rise of the E_g phonon population, respectively. In previous temperature-dependent Raman studies, both variations have been linked to modifications of the charge distribution [127, 137]. In the present pump-probe experiment, however, they appear to correlate with changes in lattice rather than in electronic degrees of freedom. Specifically, the linewidth broadening seems sensitive to early lattice reorganization, possibly reflecting an increase in structural disorder (*e.g.* different domain nucleation) or the activation of additional phonon-phonon or electron-phonon decay channels. By contrast, the frequency renormalization is possibly due to a change in the effective force constants that develops only after a greater extent of the thermalization of the different phonon modes in the lattice.

As a final remark, we note that, as discussed in Section 7.4, the marker of the phase transition remains slightly above 1 at positive delays, which could suggest an incomplete phase transition. This would be supported by the fact that, at long delays, the lattice tem-

perature increase is about 25 K, corresponding to a final temperature of roughly 110 K, just below the estimated T_{V}. However, two considerations argue against this interpretation. First, the employed pump fluence falls within the high-fluence regime reported in the literature, where the electronic phase transition is expected to be induced instantaneously and lead to the complete reorganization of the lattice [123, 124]. The detection of an incomplete phase transition would thus contrast with the results of available studies in similar excitation conditions. Second, previous works indicate that an incomplete phase transition leads to a re-establishment of the original electronic order, reduced only at a small degree by the heating effect of the pump following the equilibration of hot phonon modes [123]. In contrast, several observables in our experiment (the phase transition marker, the A_{1g} phonon linewidth and frequency, the B-mode population) show no recovery towards the initial values, but rather a slow trend further away from them, continuing beyond 50 ps. This behaviour points to a continuing progression of the phase transition, consistent with the dynamics reported by Truc et al. [126].

7.8 Open questions and perspectives

Overall, ultrafast spectroscopies and TRRS have shown their capabilities in separating on a temporal level different microscopic processes occurring at the Verwey transition. However given the complex interplay between lattice, spin, and electronic degrees of freedom, several open questions remain, providing fertile ground for future investigation.

First, the origin of the marker value remaining above 1 in pump-probe data is not fully understood. This could be simply due to the different probe wavelengths used in temperature-dependent and time-resolved measurements, which may induce small variations in the integrated intensities used to define the marker. Measurements by Borroni et al. [127] indeed show that the intensity of the B mode and its temperature dependence differ when using 2.4 eV and 3.1 eV probe energies; while less likely due to the smaller energy separation, a similar variation could occur between 513 nm and 532 nm (i.e. 2.4 eV and 2.33 eV) probes. To clarify this, temperature-dependent measurements using the 513nm probe are planned.

Another possible explanation arises from the observation that the 470 cm^{-1} mode can be detected up to 5–10 K above the electronic transition temperature due to so-called precursor effects [127]. This would imply that the transition temperature T_{V}, corresponding to the disappearance of the 470 cm^{-1} peak, could be overestimated of some K. This scenario will be easily verified obtaining an independent estimate of the Verwey transition temperature by resistivity measurements.

Finally, the comparable penetration depths of pump and probe photons may result in Raman signals excited from less-excited regions, where a lower effective pump fluence could result in only a partial transition. Studying the transition at longer delays and at varying fluence may help clarify this aspect.

Additional open questions regards:

- The long-time behaviour of the B-mode population. Indeed, literature links this mode to electronic or spin excitations across the electronic or spin-density gaps [127, 133], which close during the transition from the monoclinic to the cubic phase. After the initial rise in its population, the B-mode would thus be expected to

quench due to the transition; however, no reduction of the population is observed, and the intensity continues to increase.

- The microscopic origin of the different temporal response of the linewidth and the frequency of the A_{1g} phonon, which appear to be sensitive to different aspects of the structural phase transition.

- The relaxation dynamics of the photoinduced phase toward equilibrium, which is not addressed here since the observed spectral variations appear almost metastable within the measured time window. Given that spectra acquired at negative delays are equal to those obtained without the pump pulse, the photoinduced changes fully recover within the 5 μs time window between two sets of pulses. Investigating the phonon and structural relaxation dynamics would thus likely require probing delays of the order of several hundreds of picoseconds or nanoseconds.

- The response of the electronic degrees of freedom to photoexcitation, which has so far been investigated only in terms of charge-ordering (via ultrafast diffraction) and degree of metallicity (via time-resolved reflectivity). Time-resolved photoemission could provide direct access to the excited electrons, distinguishing increases in metallicity due to photoexcited carriers from a proper MIT associated with a gap closure, and linking lattice modifications to specific electronic transitions, as hypothesized by Truc et al. [126].

Conclusions

In this thesis, I presented the commissioning and characterization of a novel time-resolved Raman scattering (TRRS) setup developed at the NFFA-SPRINT laboratory, and its application to the study of phonon dynamics in photoexcited quantum materials. Three systems were addressed: a prototypical bulk semiconductor (silicon), a bulk and single-layer transition metal dichalcogenide (MoS_2), and a strongly correlated oxide (magnetite). These case studies exemplify the span of physical insights on nonequilibrium states enabled by ultrafast spectroscopies, and in particular highlight the unique information that TRRS can provide on vibrational and electronic degrees of freedom.

In silicon, chosen as a benchmark system to test the capabilities of the setup, TRRS enabled the monitoring of the excitation/deexcitation of the longitudinal optical phonon population as a function of temperature, revealing the low-temperature suppression of anharmonic phonon–phonon interactions. A long-lived hole population, whose dynamics appeared largely insensitive to the sample temperature, is detected through its characteristic Fano interference effect induced on the LO phonon. Furthermore, fluence-dependent measurements suggested the influence of phonon bottleneck effects on the carrier relaxation dynamics.

On MoS_2 bulk and single-layer samples, our study provided the first direct observation of a transient renormalization of phonon energies occurring on a timescale faster than phonon population growth, thus attributed to photodoping-induced effects. Fluence dependent data indicated distinct photodoping regimes, in which the renormalization of the frequency of weakly coupled phonon modes can be either enhanced or suppressed. Mode-resolved phonon population measurements revealed the formation of long-lived non-thermal phonon distributions, persisting for tens of picoseconds, both between zone-centre optical modes of different symmetry and between phonons located at different points of the Brillouin zone. A key difference between bulk and monolayer samples was identified in their relaxation dynamics at long delays, with the one of the bulk significantly influenced by a residual carrier population surviving for hundreds of picoseconds.

In magnetite, TRRS enabled the observation of a photoinduced version of the Verwey transition and the temporal separation of spectral modifications which occur simultaneously when the transition is achieved thermodynamically, via a pathway of equilibrium states. The measurements revealed that electronic modes and strongly coupled phonons are excited prior to the lattice distortion, and that different phonon spectral anomalies (linewidth broadening and frequency shifts) emerge at different delays from the excitation, possibly reflecting steps of the structural phase transition affecting distinct lattice

degrees of freedom. Although further experimental and theoretical work is required for a complete interpretation, the present results strongly motivate future efforts in investigating the energy transfer pathways among different degrees of freedom across photoinduced transitions in magnetite.

Looking ahead, several promising directions emerge from this work. Even in a benchmark system like silicon, systematic TRRS studies as a function of temperature and excitation fluence could yield new insights into microscopic phonon excitation and deexcitation mechanisms, bottleneck effects, and tunable phonon–phonon coupling regimes. In MoS_2 and related transition metal dichalcogenides, currently at the forefront of two-dimensional semiconductor research, TRRS combined with complementary ultrafast probes could enable a detailed mapping of electronic relaxation pathways and energy transfer processes across different degrees of freedom. The ability to track mode-specific phonon properties further opens possibilities to explore how substrates, thickness, or suitably engineered heterostructures can modulate phonon dynamics. From the study on magnetite, TRRS emerged as a tool to disentangle coupled degrees of freedom in a complex phase transition, suggesting further studies at varying pump conditions and initial thermodynamic states aimed to uncover the landscape of photoinduced transient phases, both in magnetite and in other correlated oxides.

More broadly, this thesis, together with other recent experimental studies, demonstrates the versatility of TRRS as a tool for investigating photoinduced states, with sensitivity extending beyond phonons to other low-energy bosonic excitations. Owing to the minimal constraints on pump photon energies, TRRS studies on the above-mentioned and others quantum materials can be readily extended to explore how the excitation of different electronic transitions affect phonon dynamics, or to directly probe phonon–phonon couplings by resonantly driving specific vibrational modes. These capabilities establish TRRS as a powerful and flexible technique, well suited to contribute to the renewed interest in phononics and its use for ultrafast control of the properties of quantum materials.

Appendices

APPENDIX A

Supplementary material on MoS_2

A.1 Computation of fluences and carriers

We report here the computation of the fluences and the excited carrier densities for the experiment on MoS_2 described in Chapter 6.

First of all, when employing a pulsed laser and working in the pump-probe scheme, the relevant quantity determining the degree of the system excitation is the energy per pulse E_p, rather than the average power P. The former can be easily retrieved from P, which is typically measured experimentally, as:

$$E_p(J) = \frac{P(W)}{RR(Hz)} \tag{C.1}$$

where RR is the laser repetition rate.

For a gaussian beam, the fluence F, *i.e.* the energy density impinging on the sample per unit surface, can then be obtained from the ratio between E_p and the beam area A:

$$F\left(\frac{J}{cm^2}\right) = 2 \cdot \frac{E_p(J)}{A(cm^2)} \tag{C.2}$$

Here A was obtained considering as the beam radius the parameter $1/e^2$, that, in an ideal case, delineates an area containing approximately 86.5% of the total power. The factor 2 on the right side of the equation accounts for the fact that for a Gaussian laser beam the power density at the centre of the spot is twice what expected from a circular top-hat shaped beam of diameter equal to $1/e^2$ [138].

While the excited carrier densities can be calculated either from F or E_p (*i.e.* including or not the factor 2), in the following we use the former. Indeed, the probe laser intensity has a Gaussian distribution as well, and thus the majority of the Raman signal is excited from the central part of the beam, with higher peak power density.

The density of photons travelling through the material, can then be calculated as:

$$n_{ph}^{in} = \frac{F}{E_{ph}}(1 - R) \tag{C.3}$$

where E_{ph} is the energy of a single photon (here of wavelength $\lambda = 633\ \mathrm{nm}$) and R is the sample reflectivity. Then, for above-bandgap pumping, the excited carrier density n_c is equal to the absorbed photon density n_{ph}^{abs}.

In the case of a thick bulk sample, photons are absorbed over a scattering volume, and n_c can be obtained as:

$$n_c = n_{ph}^{abs} \approx \frac{n_{ph}^{in} \cdot 0.63}{\delta} \tag{C.4}$$

where $\delta = 1/\alpha$ is the penetration depth of the radiation inside the material and the factor 0.63 takes into account its definition as the length scale over which the intensity of the radiation is reduced to a fraction $1/e$ of its initial value. Note that here we are making the approximation of considering a uniform excitation of the sample inside the scattering volume.

On the other hand, in the case of a thin sample, such as a 1L of MoS_2, the carrier density is determined by:

$$n_c = n_{ph}^{abs} \approx n_{ph}^{in} \cdot \gamma \tag{C.5}$$

where $\gamma = e^{-\frac{\Delta_s}{\delta}}$ is the fraction of the intensity absorbed by a sample of thickness Δ_s.

If a substrate is present, this equation should be modified taking into account the reflection of the beam from the substrate, leading to a second passage inside the material:

$$n_c = n_{ph}^{abs} \approx n_{ph}^{in} \cdot (1 + R_{sub}) \cdot \gamma \tag{C.6}$$

where R_{sub} is the substrate reflectivity.

In the experiments on the bulk described in the main text, considering a reflectivity $R = 0.59$ (at a $\sim 45°$ incidence angle) and a penetration depth $\delta = 55$ nm [75], the resulting carrier densities are found to be:

- $n_c \sim 2.2 \cdot 10^{21}$ cm^{-3} for the dataset with $F = 15$ mJ/cm^2,
- $n_c \sim 1.5 \cdot 10^{21}$ cm^{-3} for the dataset with $F = 10$ mJ/cm^2,
- $n_c \sim 7.3 \cdot 10^{20}$ cm^{-3} for the dataset with $F = 5$ mJ/cm^2.

In the single layer case, considering $R_{sub} \sim 0.96$ for gold and $R_{sub} \sim 0.1$ for ITO [45, 76]), and $R \sim 0.56$, $\gamma = e^{-\frac{\Delta_{1L}}{\delta}} = 0.015$ for a 1L of MoS_2 [45, 75], we obtain:

- $n_c \sim 1.0 \cdot 10^{14}$ cm^{-2} for the 1L/ITO, using a fluence $F = 4.5$ mJ/cm^2,
- $n_c \sim 9.5 \cdot 10^{13}$ cm^{-2} for the 1L/Au, using a fluence $F = 2.3$ mJ/cm^2.

In the last case, due to the high reflectivity of the Au substrate at the pump wavelength, the effective fluence on the 1L sample is given by almost twice the impinging fluence, leading to a similar value of n_c to the one employed for the 1L/ITO. We note that these carrier density values are consistent with the one obtained on the bulk at the highest fluence value, since, given the MoS_2 layer thickness of 0.7 nm, a carrier volume density of 10^{21} cm^{-3} corresponds to a carrier density of $7 \cdot 10^{13}$ cm^{-2} within each layer.

A.2 Correction to temperatures and relative considerations

We discuss here possible effects of the sample optical absorption on the temperature extracted from the antiStokes/Stokes intensity ratio. The optical constants of MoS_2 display indeed a non-flat dependence on the wavelength in the region explored in the present experiment (around the 513 nm probe). More specifically, the absorption is more efficient in the antiStokes region than in the Stokes region (k goes from 1.7 at 2.46 eV to 1.3

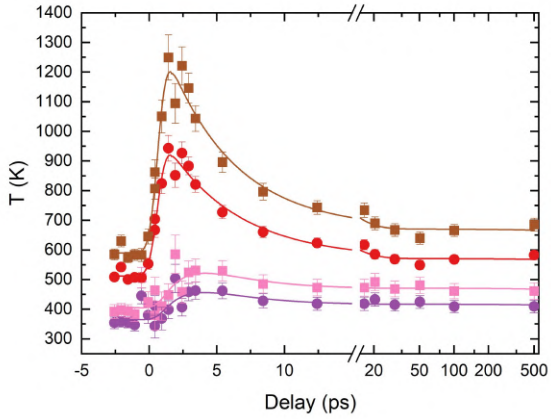

Figure A.1: Corrected phonon temperatures for the two phonon modes in bulk MoS_2. Red and purple dots display the trends for the A and E modes reported in Figure 6.8 in Chapter 6. Brown and pink squares mark the values obtained after the correction based on the absorption coefficients. Continuous lines display the results of the time trend fitting.

at 2.36 eV [45, 75]). This could result in an underestimation of the phonon temperature in the bulk sample. In the monolayer samples, instead, this is not expected to produce any relevant effects, given the very small thickness of the probed region.

Considering the absorption of the Raman scattered photons at different depths inside the sample, the measured antiStokes/Stokes intensity ratio should be corrected by a factor:

$$\frac{\int_0^{+\infty} e^{-(\alpha_L+\alpha_S)x}dx}{\int_0^{+\infty} e^{-(\alpha_L+\alpha_{AS})x}dx} = \frac{\alpha_L+\alpha_{AS}}{\alpha_L+\alpha_S} = 1.16 \tag{C.7}$$

where $\alpha_L, \alpha_S, \alpha_{AS}$ are the absorption coefficients at the laser, Stokes and antiStokes wavelengths respectively and the numerical value was obtained based on data in [45, 75].

The effect of the correction is displayed in Figure A.1, where we compare the extracted temperature trends with and without the correction. The characteristic time constant extracted from the fit of the corrected temperatures are reported in Table S1. It is worth to note that, while the correction introduces a difference in the absolute values of the temperature, it does not affect the assessed system dynamics. Based on this consideration and given the uncertainty in the experimental determination of the optical functions, the present correction was not applied to the data presented in the main text.

	T_A	T_E
t_0	0.6	0.6
τ_1	5.0	3.5
τ_2	$\gg 500$	$\gg 500$
τ_r	-	5.3

Table A.1: Time constants from the fit of the corrected temperature trends. Fitting function and parameters as in the main text. Time delays are expressed in ps. The t_0 values are obtained as a shared fitting parameter for the two phonon modes.

A.3 Resonance Raman effects

We comment here on the reduction of the Raman signal observed only in the bulk sample after photoexcitation.

An increase in the phonon population leads to an enhancement of the Raman intensities on both the Stokes and antiStokes sides. In the following we will show that while in the 1L the temperature dependence reasonably explains the measured intensity trend, this is clearly not the case in the bulk, where a significant intensity reduction is appreciated, with an overall non-monotonic behaviour versus time. We can conclude that the observed signal reduction in the bulk sample originates from the part of the Raman cross section related to electronic resonance, rather than from the phonon population factor. A similar effect has indeed been observed in semiconductor samples measured by TRRS when the probe energy matches an electronic transition of the system, leading to a resonant enhancement of the Raman cross section. In pump-probe TRRS, depopulating (populating) the VB (CB) via photoexcitation can reduce the probability of Raman transitions from the ground electronic state and thus dynamically quench the resonance [34, 44]. In our case, the 2.4 eV probe energy is greater than the MoS_2 band gap and can induce electronic transitions. Both in 1L and in bulk, however, the probe energy does not match a peak in the joint density of states and is thus considered only weakly resonant with the system. Therefore, it is difficult to adopt the same straightforward interpretation as for resonant experiments conducted on Si and WS_2 [34, 44].

More in details, as reported in Chapter 2, the intensity of the Stokes and antiStokes Raman signals associated to a specific phonon mode can be written respectively as:

$$I_S = F \cdot (n_B + 1) \cdot (\hbar\omega_l - \hbar\omega_\nu)^3 \qquad I_{AS} = F \cdot n_B \cdot (\hbar\omega_l + \hbar\omega_\nu)^3 \tag{C.8}$$

where $\hbar\omega_l$, $\hbar\omega_\nu$ are the laser and phonon energies respectively, n_B is the Bose-Einstein distribution describing the phonon population, and F contains all factors common to the Stokes and antiStokes processes. Since the Raman process is electron-mediated, F contains the coupling of the impinging photons with the electrons and can be thus strongly modified by the presence of resonances or changes in the electronic state of the system [53]. As described in the main text, our data show a clear decrease of the Stokes peaks intensities after photoexcitation in the bulk sample. This is not observed in the 1L samples, where we observe an opposite behaviour. When retrieving the phonon population from the antiStokes/Stokes intensity ratio, the trend obtained is qualitatively the same for all samples. This points towards the factor F in being the origin of the signal reduction in the bulk, as its variation affects the Stokes and antiStokes processes in the same way, with no effect on the calculated phonon population.

We can quantify the variation of F in the following way. From the data obtained without the pump we extract the F value at equilibrium as

$$F^{eq} = \frac{I_S^{eq}}{(n_B^{eq} + 1) \cdot (\hbar\omega_l - \hbar\omega_\nu^{eq})^3} = \frac{I_{AS}^{eq}}{n_B^{eq} \cdot (\hbar\omega_l + \hbar\omega_\nu^{eq})^3} \tag{C.9}$$

We then use it to calculate the expected $I_S(t)$ and $I_{AS}(t)$ values, if n_B and ω_ν were the only pump-dependent parts of the Raman cross section:

$$I_S(t) = F^{eq} \cdot (n_B(t) + 1) \cdot (\hbar\omega_l - \hbar\omega_\nu(t))^3 \qquad I_{AS}(t) = F^{eq} \cdot n_B(t) \cdot (\hbar\omega_l + \hbar\omega_\nu(t))^3 \tag{C.10}$$

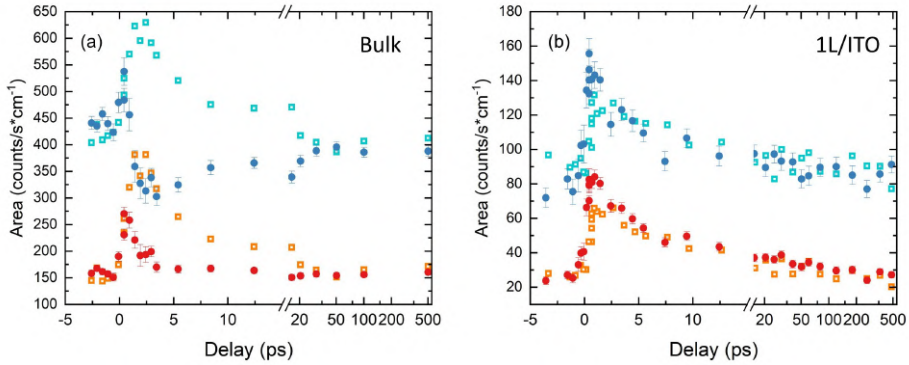

Figure A.2: Photoinduced intensity variation of the A phonon in the (a) bulk, (b) 1L on ITO samples. Filled blue (red) dots mark the measured area of the Stokes (antiStokes) peaks extracted from the multipeak fitting. Empty light blue (orange) squares mark the corresponding values expected considering the change of the Raman cross section due to n_B and ω_ν (see text).

where $n_B(t)$ and $\omega_\nu(t)$ where obtained from the multipeak fitting of the pump-probe spectra. The trends calculated for the A phonons are shown along with the actually measured ones ($I_S^{PP}(t)$,$I_{AS}^{PP}(t)$) in Figure A.2 (a) and (b). We can see how in the bulk for ~ 1 ps the measured intensities increase following the expected trends, then show a sudden drop both in the Stokes and antiStokes sides. On the other hand, in the 1L/ITO the two trends are in much better correspondence.

It is clear how, in the bulk system, the factor F has a strong dependence on the pump-probe delay. By writing $F = F^{eq} \cdot C(t)$, we obtain the varying component as:

$$C^S(t) = \frac{I_S^{PP}(t)}{F^{eq} \cdot (n_B(t)+1) \cdot (\hbar\omega_l - \hbar\omega_\nu(t))^3} \qquad C^{AS}(t) = \frac{I_{AS}^{PP}(t)}{F^{eq} \cdot n_B(t) \cdot (\hbar\omega_l + \hbar\omega_\nu(t))^3} \tag{C.11}$$

The result for $C^S(t)$ is displayed in Figure A.3. An analogous trend is followed by $C^{AS}(t)$, with larger experimental errors due to the smaller antiStokes intensities. From the plot, it is evident how the minimum of $C^S(t)$ is delayed with respect to the pump-probe overlap and the phonon frequency shift, which is associated to the photoinduced transient doping of the system.

As mentioned above, a photoinduced reduction of the intensity has been observed in semiconductors when the Raman process is resonant with an electronic transition which is quenched by the pump. While our 515 nm probe is not usually considered to be in resonant conditions, its energy is above the MoS_2 band gap. Moreover, it is on the low energy tail of the so-called C exciton, a peak at 2.6 eV in the JDOS associated with the nested section of the electronic bands between the Q and Γ points of the BZ. In the bulk, the Q and Γ points are the minimum of the conduction band and the maximum of the valence band respectively, thus the BZ positions where the photoexcited carriers relax after few tens of fs. However, since the variation of $C(t)$ seems to happen on a timescale much longer than electronic relaxations, it is difficult to directly link the two phenomena, and the different behaviour of the Raman intensity of the bulk and 1L samples remains puzzling.

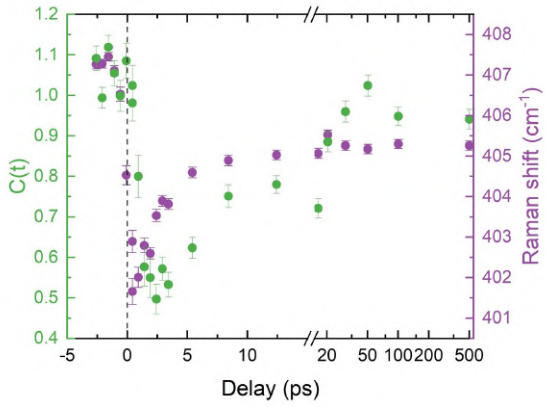

Figure A.3: Comparison between the variation of C(t) (green) and the frequency shift (purple) of the A phonon in the bulk sample.

A.4 Multi-temperature model for hot phonon real-time dynamics

Here we provide details on the model which mimics the time dependence of the effective phonon temperatures for the modes A_{1g} and E_{2g} in bulk MoS_2 estimated by the ratio of the Stokes-antiStokes peaks. We consider an electron system coupled with three lattice baths: the $\nu = A_{1g}$ and $\nu = E_{2g}$ modes at the zone center, and the ν=ph bath that accounts of all the other phonon modes in the whole BZ. The temperature of each electron and lattice subsystem T_e, T_ν is ruled by the energy transfer between the different degrees of freedom described by the set of equations:

$$C_e(T_e)\frac{\partial T_e}{\partial t} = S(t) - \sum_\nu G_\nu(T_e - T_\nu), \tag{C.12}$$

$$C_\nu \frac{\partial T_\nu}{\partial t} = G_\nu(T_e - T_\nu) + \sum_{\nu'} \alpha_{\nu,\nu'}(T_\nu - T_{\nu'}), \tag{C.13}$$

Here $S(t)$ described the energy absorbed by the electronic degrees of freedom due to the pumping process with a typical Gaussian profile, $C_e(T) = \gamma T$ and C_ν are heat capacities of the electronic and lattice degrees of freedom, and G_ν are the electron-phonon relaxation rates governed by the electron-phonon coupling. The parameters $\alpha_{\nu,\nu'}$ account for anharmonic coupling.

In Figure 6.10 (a) in the main text, we show the time evolution of T_e, $T_{A_{1g}}$, $T_{E_{2g}}$, C_{ph} with a choice of parameters that mimic the experimental observed behavior for bulk MoS_2. In particular we set: $G_{A_{1g}}/C_e^0 = 12\ \mathrm{ps}^{-1}$, $G_{E_{2g}}/C_e^0 = 1.2\ \mathrm{ps}^{-1}$, $G_{ph}/C_e^0 = 42\ \mathrm{ps}^{-1}$, $C_{A_{1g}} = C_{E_{2g}} = 6C_e^0$, and $C_{ph}/C_e^0 = 510$, where $C_e^0 = C_e(300\,\mathrm{K})$. In order to reduce the number of free fitting parameters, we neglect here the anharmonic terms $\alpha_{\nu,\nu'}$.

Note that in such modelling, with no dissipative channels, the total energy absorbed from the pumping process is completely stored in the electron+lattice system, and the electron-phonon coupling leads to a final internal thermalization among the different degree of freedom towards a final state with higher energy than before pumping. In order to model dissipative and/or charge transfer processes from the sample to the substrate in single-layer MoS_2 compounds, we evaluate the energy of each subsystem, $E_{el}(t)$, $E_{A_{1g}}(t)$, $E_{E_{2g}}(t)$, $E_{ph}(t)$, and we add in Eq. C.12 a dissipation term for the excess energy in the electronic system $-\Delta E_{el}(t)/\tau_{diss}$, where $-\Delta E_{el}(t) = E_{el}(t) - E_{el}(t = -\infty)$. The resulting time dynamics of the different effective temperatures is shown in Figure

6.10 (b), representative of single-layer MoS_2 on a substrate. We find a qualitative agreement with the experimental behaviour with a microscopical dissipation rate $\tau_{diss} \sim 0.5$ ps. Note that such fast parameter is not directly reflected in a short-time decay of the effective temperature. The fast dynamics might in fact be compensated by backflow energy transfer from the lattice mode "ph", carrying the dominant heat capacity of the total system. The resulting effective exponential decay of $T_e(t)$ is thus much longer (abous 50 ps for $\tau_{diss} \sim 0.5$ ps), due to the balance between these two processes.

A.5 Additional data on the longitudinal acoustic mode

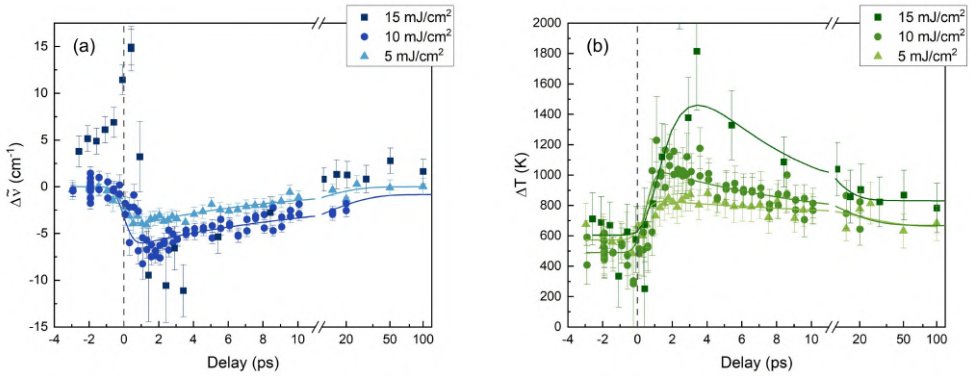

Figure A.4: Temporal evolution of (a) the phonon frequency shift and (b) the variation phonon temperature of the LA mode. Continuous lines display the results of the time trends fittings

APPENDIX B

Supplementary material on magnetite

B.1 Additional temperature-dependent measurements

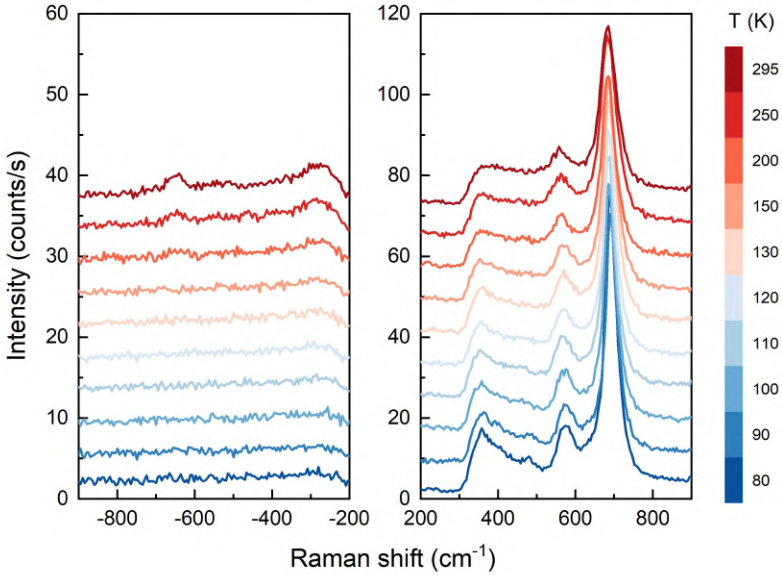

Figure B.1: Temperature-dependent Raman measurements on magnetite with a 532 nm (2.33 eV) CW laser. The data were acquired with the 600 rows/mm grating, providing lower spectral resolution but enabling the simultaneous acquisition of the Stokes and antiStokes sides. No magnetite peak on the antiStokes side is visible for measurements below 150 K. Raman spectra are vertically shifted for clarity.

B.2 Population dynamics from antiStokes intensities

Figure B.2 provides the comparison between the values of the variation of the population $\frac{n(t)}{n_0}$ of the A_{1g} mode obtained from the antiStokes/Stokes intensity ratio and from the antiStokes ratio alone. It can be seen how the two methods give results in very good agreement, signalling a negligible dependence of the $C\chi^2$ factor on the pump-probe delay (see main text). This supports the solidity of the analysis on the E_g and B modes, where the measurements of the Stokes intensity is not possible.

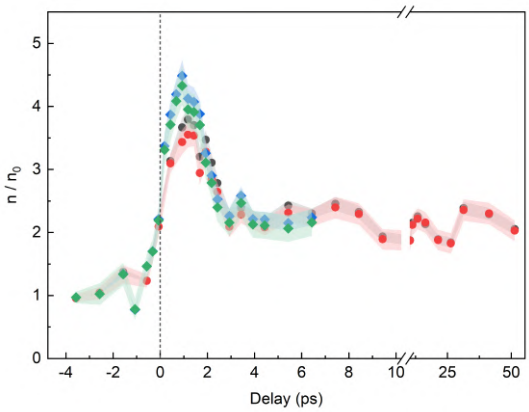

Figure B.2: Comparison of population dynamics calculations for the A_{1g} mode. The values obtained from the antiStokes/Stokes intensity ratio are shown as black and blue symbols for dataset 1 and dataset 2 respectively. Values obtained from the antiStokes ratio alone are shown as red and green symbols.

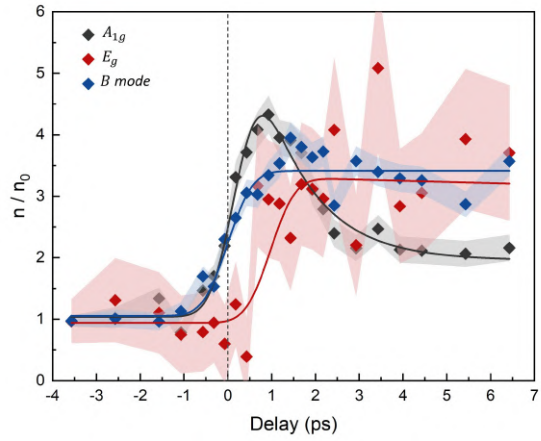

Figure B.3: Population dynamics extracted from dataset 2. The dynamics of the three modes display the same trends described in the main text for dataset 1.

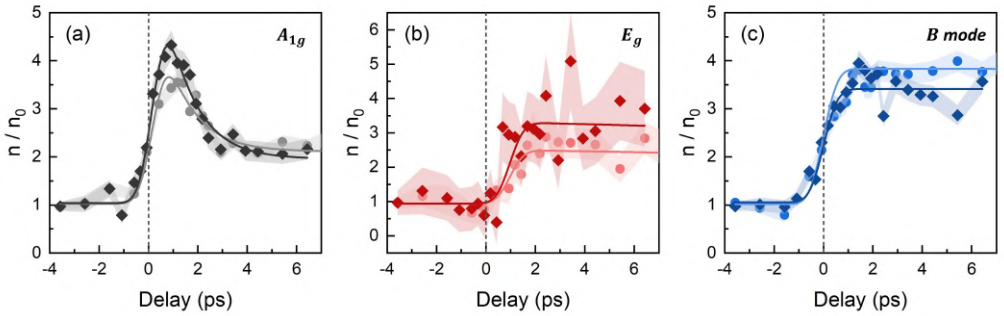

Figure B.4: Comparison between the population dynamics extracted from the two datasets at short delays. Light dots and dark symbols mark the values extracted from dataset 1 and 2 respectively, for (a) A_{1g} and (b) E_g phonon modes and (c) the broad B mode ascribed to electronic or magnonic scattering. The data from the two dataset display some differences in numerical values but consistent dynamics.

B.3 Additional temporal trends

Figure B.5 displays the temporal evolution of the intensity of the continuum background in the high energy region. The displayed values are obtained as the normalized variation of the integrated intensity of the Stokes Raman spectrum between 1000 and 1300 cm^{-1}, namely $\frac{A(t)-A_0}{A_0}$, where A_0 represents the average value of the integrated area at negative delays. The data from both datasets are in perfect agreement and were fitted with the function 7.2 described in the main text, allowing to retrieve a value of the onset time $t_0^{bkg} = 0.06 \pm 0.09$ ps and of the decay time $\tau^{bkg} = 7.5 \pm 3.3$ ps.

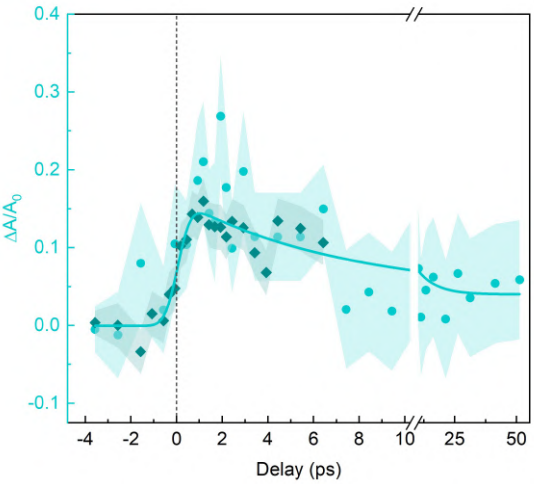

Figure B.5: Normalized intensity variations of the high energy background of the Stokes spectra. Light dots and dark symbols mark the results obtained from dataset 1 and 2, respectively. A solid line mark the result of the fit.

Bibliography

1. Zhang, J. & Averitt, R. Dynamics and Control in Complex Transition Metal Oxides. *Annual Review of Materials Research* **44,** 19–43. ISSN: 1545-4118. https://www.annualreviews.org/content/journals/10.1146/annurev-matsci-070813-113258 (2014).
2. Pincelli, T. *Probing electron correlation dynamics: a multi-technique study applied to the half-metallic oxide La3-xSrxMnO5* PhD thesis (Università degli Studi di Milano, 2017).
3. Maiuri, M., Garavelli, M. & Cerullo, G. Ultrafast Spectroscopy: State of the Art and Open Challenges. *Journal of the American Chemical Society* **142,** 3–15. https://doi.org/10.1021/jacs.9b10533 (2020).
4. Dong, T., Zhang, S.-J. & Wang, N.-L. Recent Development of Ultrafast Optical Characterizations for Quantum Materials. *Advanced Materials* **35,** 2110068 (2023).
5. Popmintchev, T., Chen, M.-C., Popmintchev, D., Arpin, P., Brown, S., Ališauskas, S., Andriukaitis, G., Balčiunas, T., Mücke, O. D., Pugzlys, A., Baltuška, A., Shim, B., Schrauth, S. E., Gaeta, A., Hernández-García, C., Plaja, L., Becker, A., Jaron-Becker, A., Murnane, M. M. & Kapteyn, H. C. Bright Coherent Ultrahigh Harmonics in the keV X-ray Regime from Mid-Infrared Femtosecond Lasers. *Science* **336,** 1287–1291. https://www.science.org/doi/abs/10.1126/science.1218497 (2012).
6. Lloyd-Hughes, J., Oppeneer, P. M., Pereira dos Santos, T., Schleife, A., Meng, S., Sentef, M. A., Ruggenthaler, M., Rubio, A., Radu, I., Murnane, M., Shi, X., Kapteyn, H., Stadtmüller, B., Dani, K. M., da Jornada, F. H., Prinz, E., Aeschlimann, M., Milot, R. L., Burdanova, M., Boland, J., Cocker, T. & Hegmann, F. The 2021 ultrafast spectroscopic probes of condensed matter roadmap. *Journal of Physics: Condensed Matter* **33,** 353001. https://doi.org/10.1088/1361-648X/abfe21 (2021).
7. Orenstein, J. Ultrafast spectroscopy of quantum materials. *Physics Today* **65,** 44–50. ISSN: 0031-9228. https://doi.org/10.1063/PT.3.1717 (2012).
8. De la Torre, A., Kennes, D. M., Claassen, M., Gerber, S., McIver, J. W. & Sentef, M. A. Colloquium: Nonthermal pathways to ultrafast control in quantum materials. *Rev. Mod. Phys.* **93,** 041002. https://link.aps.org/doi/10.1103/RevModPhys.93.041002 (2021).

9. Disa, A. S., Nova, T. F. & Cavalleri, A. Engineering crystal structures with light. *Nature Physics* **17,** 1087–1092. ISSN: 1745-2481. https://doi.org/10.1038/s41567-021-01366-1 (2021).
10. Fausti, D., Tobey, R. I., Dean, N., Kaiser, S., Dienst, A., Hoffmann, M. C., Pyon, S., Takayama, T., Takagi, H. & Cavalleri, A. Light-Induced Superconductivity in a Stripe-Ordered Cuprate. *Science* **331,** 189–191. https://www.science.org/doi/abs/10.1126/science.1197294 (2011).
11. Li, X., Qiu, T., Zhang, J., Baldini, E., Lu, J., Rappe, A. M. & Nelson, K. A. Terahertz field–induced ferroelectricity in quantum paraelectric SrTiO¡sub¿3¡/sub¿. *Science* **364,** 1079–1082. https://www.science.org/doi/abs/10.1126/science.aaw4913 (2019).
12. Zeng, Z., Först, M., Fechner, M., Buzzi, M., Amuah, E. B., Putzke, C., Moll, P. J. W., Prabhakaran, D., Radaelli, P. G. & Cavalleri, A. Photo-induced chirality in a nonchiral crystal. *Science* **387,** 431–436. https://www.science.org/doi/abs/10.1126/science.adr4713 (2025).
13. Fausti, D. & van Loosdrecht, P. H. in *Optical Techniques for Solid-State Materials Characterization* 507–527 (CRC Press, 2012). ISBN: 9780429192913.
14. Kukura, P., McCamant, D. W. & Mathies, R. A. Femtosecond Stimulated Raman Spectroscopy. *Annual Review of Physical Chemistry* **58,** 461–488. ISSN: 1545-1593. https://www.annualreviews.org/content/journals/10.1146/annurev.physchem.58.032806.104456 (2007).
15. Chou, T.-H., Först, M., Fechner, M., Henstridge, M., Roy, S., Buzzi, M., Nicoletti, D., Liu, Y., Nakata, S., Keimer, B. & Cavalleri, A. Ultrafast Raman thermometry in driven $YBa_2Cu_3O_{6.48}$. *Phys. Rev. B* **109,** 195141. https://link.aps.org/doi/10.1103/PhysRevB.109.195141 (2024).
16. Kuramochi, H. & Tahara, T. Tracking Ultrafast Structural Dynamics by Time-Domain Raman Spectroscopy. *Journal of the American Chemical Society* **143,** 9699–9717. https://doi.org/10.1021/jacs.1c02545 (2021).
17. René de Cotret, L. P., Pöhls, J.-H., Stern, M. J., Otto, M. R., Sutton, M. & Siwick, B. J. Time- and momentum-resolved phonon population dynamics with ultrafast electron diffuse scattering. *Phys. Rev. B* **100,** 214115. https://link.aps.org/doi/10.1103/PhysRevB.100.214115 (2019).
18. Mo, M., Tamm, A., Metsanurk, E., Chen, Z., Wang, L., Frost, M., Hartley, N. J., Ji, F., Pandolfi, S., Reid, A. H., Sun, P., Shen, X., Wang, Y., Wang, X., Glenzer, S. & Correa, A. A. Direct observation of strong momentum-dependent electron-phonon coupling in a metal. *Science Advances* **10,** eadk9051. https://www.science.org/doi/abs/10.1126/sciadv.adk9051 (2024).
19. Raman, C. V. & Krishnan, K. S. A New Type of Secondary Radiation. *Nature* **121,** 501–502. ISSN: 1476-4687. https://doi.org/10.1038/121501c0 (1928).
20. Loudon, R. Theory of the first-order Raman effect in crystals. *Proceedings of the Royal Society of London. Series A. Mathematical and Physical Sciences* **275,** 218–232. https://royalsocietypublishing.org/doi/abs/10.1098/rspa.1963.0166 (1963).

21. Chen, S.-H. & Kotlarchyk, M. *Interactions of Photons and Neutrons with Matter* 2nd. https://www.worldscientific.com/doi/abs/10.1142/4339 (WORLD SCIENTIFIC, 2007).
22. Yu, P. Y. & Cardona, M. *Fundamentals of Semiconductors* ISBN: 978-3-642-00710-1 (Springer Berlin, Heidelberg, 2010).
23. Zeyher, R., Bilz, H. & Cardona, M. On the 4 law in microscopic theories of inelastic light scattering. *Solid State Communications* **19,** 57–60. ISSN: 0038-1098. https://www.sciencedirect.com/science/article/pii/0038109876917282 (1976).
24. Compaan, A. & Trodahl, H. J. Resonance Raman scattering in Si at elevated temperatures. *Phys. Rev. B* **29,** 793–801. https://link.aps.org/doi/10.1103/PhysRevB.29.793 (1984).
25. Potts, J. E., Walker, C. T. & Nair, I. R. Temperature Dependence of Second-Order Raman Scattering in Potassium and Rubidium Halides. *Phys. Rev. B* **8,** 2756–2771. https://link.aps.org/doi/10.1103/PhysRevB.8.2756 (1973).
26. Wang, Y., Devereaux, T. P. & Chen, C.-C. Theory of time-resolved Raman scattering in correlated systems: Ultrafast engineering of spin dynamics and detection of thermalization. *Phys. Rev. B* **98,** 245106. https://link.aps.org/doi/10.1103/PhysRevB.98.245106 (2018).
27. Von der Linde, D., Kuhl, J. & Klingenberg, H. Raman Scattering from Nonequilibrium LO Phonons with Picosecond Resolution. *Phys. Rev. Lett.* **44,** 1505–1508. https://link.aps.org/doi/10.1103/PhysRevLett.44.1505 (1980).
28. Kash, J. A., Tsang, J. C. & Hvam, J. M. Subpicosecond Time-Resolved Raman Spectroscopy of LO Phonons in GaAs. *Phys. Rev. Lett.* **54,** 2151–2154. https://link.aps.org/doi/10.1103/PhysRevLett.54.2151 (1985).
29. Yang, J.-A., Parham, S., Dessau, D. & Reznik, D. Novel Electron-Phonon Relaxation Pathway in Graphite Revealed by Time-Resolved Raman Scattering and Angle-Resolved Photoemission Spectroscopy. *Scientific Reports* **7,** 40876. ISSN: 2045-2322. https://doi.org/10.1038/srep40876 (2017).
30. Fausti, D., Misochko, O. V. & van Loosdrecht, P. H. M. Ultrafast photoinduced structure phase transition in antimony single crystals. *Phys. Rev. B* **80,** 161207. https://link.aps.org/doi/10.1103/PhysRevB.80.161207 (2009).
31. Raciti, G., Abad, B., Dettori, R., Sen, R., Sivan, A. K., Sojo-Gordillo, J. M., Vast, N., Rurali, R., Melis, C., Sjakste, J. & Zardo, I. *Unraveling energy flow mechanisms in semiconductors by ultrafast spectroscopy: Germanium as a case study* Preprint. 2025. arXiv: 2508.10544 [cond-mat.mtrl-sci]. https://arxiv.org/abs/2508.10544.
32. Saichu, R. P., Mahns, I., Goos, A., Binder, S., May, P., Singer, S. G., Schulz, B., Rusydi, A., Unterhinninghofen, J., Manske, D., Guptasarma, P., Williamsen, M. S. & Rübhausen, M. Two-Component Dynamics of the Order Parameter of High Temperature $Bi_2Sr_2CaCu_2\mathbf{O}_{8+\delta}$ Superconductors Revealed by Time-Resolved Raman Scattering. *Phys. Rev. Lett.* **102,** 177004. https://link.aps.org/doi/10.1103/PhysRevLett.102.177004 (2009).

33. Gatuingt, L., Alekhin, A., Nilforoushan, N., Houver, S., Sacuto, A., Gu, G. & Gallais, Y. *Ultrafast Raman probe of the photoinduced superconducting to normal state transition in the cuprate $Bi_2Sr_2CaCu_2O_{8+\delta}$* Preprint. 2025. arXiv: 2508.04385 [cond-mat.supr-con https://arxiv.org/abs/2508.04385.
34. Han, S., Boguschewski, C., Gao, Y., Xiao, L., Zhu, J. & van Loosdrecht, P. H. M. Incoherent phonon population and exciton-exciton annihilation dynamics in monolayer WS2 revealed by time-resolved Resonance Raman scattering. *Opt. Express* **27,** 29949–29961. https://opg.optica.org/oe/abstract.cfm?URI=oe-27-21-29949 (2019).
35. Basov, D. N. & Timusk, T. Electrodynamics of high-T_c superconductors. *Rev. Mod. Phys.* **77,** 721–779. https://link.aps.org/doi/10.1103/RevModPhys.77.721 (2005).
36. Mak, K. F., Ju, L., Wang, F. & Heinz, T. F. Optical spectroscopy of graphene: From the far infrared to the ultraviolet. *Solid State Communications* **152.** Exploring Graphene, Recent Research Advances, 1341–1349. ISSN: 0038-1098. https://www.sciencedirect.com/science/article/pii/S0038109812002700 (2012).
37. Bisogni, V., Catalano, S., Green, R. J., Gibert, M., Scherwitzl, R., Huang, Y., Strocov, V. N., Zubko, P., Balandeh, S., Triscone, J.-M., Sawatzky, G. & Schmitt, T. Ground-state oxygen holes and the metal–insulator transition in the negative charge-transfer rare-earth nickelates. *Nature Communications* **7,** 13017. ISSN: 2041-1723. https://doi.org/10.1038/ncomms13017 (2016).
38. Cucini, R., Pincelli, T., Panaccione, G., Kopic, D., Frassetto, F., Miotti, P., Pierantozzi, G. M., Peli, S., Fondacaro, A., De Luisa, A., De Vita, A., Carrara, P., Krizmancic, D., Payne, D. T., Salvador, F., Sterzi, A., Poletto, L., Parmigiani, F., Rossi, G. & Cilento, F. Coherent narrowband light source for ultrafast photoelectron spectroscopy in the 17–31 eV photon energy range. *Structural Dynamics* **7,** 014303. ISSN: 2329-7778. https://doi.org/10.1063/1.5131216 (2020).
39. Perlangeli, M. *Ultrafast electron and exciton dynamics in transition metal dichalcogenides, studied by optical and photoelectron spectroscopies* PhD thesis (Università degli Studi di Trieste, 2024).
40. Carrara, P., Brioschi, M., Longo, E., Dagur, D., Polewczyk, V., Vinai, G., Mantovan, R., Fanciulli, M., Rossi, G., Panaccione, G. & Cucini, R. All-Optical Generation and Time-Resolved Polarimetry of Magnetoacoustic Resonances via Transient Grating Spectroscopy. *Phys. Rev. Appl.* **18,** 044009. https://link.aps.org/doi/10.1103/PhysRevApplied.18.044009 (2022).
41. Brioschi, M., Carrara, P., Polewczyk, V., Dagur, D., Vinai, G., Parisse, P., Zilio, S. D., Panaccione, G., Rossi, G. & Cucini, R. Multidetection scheme for transient-grating-based spectroscopy. *Opt. Lett.* **48,** 167–170. https://opg.optica.org/ol/abstract.cfm?URI=ol-48-1-167 (2023).
42. *NFFA-Trieste project* https://www.trieste.nffa.eu/.
43. Mariani, A., Campetella, M., Fasolato, C., Daniele, M., Capitani, F., Bencivenni, L., Postorino, P., Lupi, S., Caminiti, R. & Gontrani, L. A joint experimental and computational study on ethylammonium nitrate-ethylene glycol 1:1 mixture. Structural, kinetic, dynamic and spectroscopic properties. *Journal of Molecular Liquids* **226,** 2–8. ISSN: 0167-7322. https://www.sciencedirect.com/science/article/pii/S0167732216322565 (2017).

44. Zhu, J., Versteeg, R. B., Padmanabhan, P. & van Loosdrecht, P. H. M. Dynamical resonance quench and Fano interference in spontaneous Raman scattering from quasiparticle and collective excitations. *Phys. Rev. B* **99,** 094305. https://link.aps.org/doi/10.1103/PhysRevB.99.094305 (2019).

45. Polyanskiy, M. N. Refractiveindex.info database of optical constants. *Scientific Data* **11,** 94. ISSN: 2052-4463. https://doi.org/10.1038/s41597-023-02898-2 (2024).

46. Fano, U. Effects of Configuration Interaction on Intensities and Phase Shifts. *Phys. Rev.* **124,** 1866–1878. https://link.aps.org/doi/10.1103/PhysRev.124.1866 (1961).

47. Limonov, M. F., Rybin, M. V., Poddubny, A. N. & Kivshar, Y. S. Fano resonances in photonics. *Nature Photonics* **11,** 543–554. ISSN: 1749-4893. https://doi.org/10.1038/nphoton.2017.142 (2017).

48. Cerdeira, F., Fjeldly, T. A. & Cardona, M. Interaction between electronic and vibronic Raman scattering in heavily doped silicon. *Solid State Communications* **13,** 325–328. ISSN: 0038-1098. https://www.sciencedirect.com/science/article/pii/0038109873906029 (1973).

49. Cerdeira, F., Fjeldly, T. A. & Cardona, M. Effect of Free Carriers on Zone-Center Vibrational Modes in Heavily Doped *p*-type Si. II. Optical Modes. *Phys. Rev. B* **8,** 4734–4745. https://link.aps.org/doi/10.1103/PhysRevB.8.4734 (1973).

50. Burke, B. G., Chan, J., Williams, K. A., Wu, Z., Puretzky, A. A. & Geohegan, D. B. Raman study of Fano interference in p-type doped silicon. *Journal of Raman Spectroscopy* **41,** 1759–1764. https://analyticalsciencejournals.onlinelibrary.wiley.com/doi/abs/10.1002/jrs.2614 (2010).

51. Kato, K., Hasegawa, Y., Oguri, K., Tawara, T., Nishikawa, T. & Gotoh, H. Relationship between the Fano asymmetry parameter and time-domain spectra studied by time-resolved measurement of carriers and phonons in *p*-type Si. *Phys. Rev. B* **97,** 104301. https://link.aps.org/doi/10.1103/PhysRevB.97.104301 (2018).

52. Häcker, R. & Hangleiter, A. Intrinsic upper limits of the carrier lifetime in silicon. *Journal of Applied Physics* **75,** 7570–7572. ISSN: 0021-8979. https://doi.org/10.1063/1.356634 (1994).

53. Loudon, R. The Raman effect in crystals. *Advances in Physics* **13,** 423–482. https://doi.org/10.1080/00018736400101051 (1964).

54. Klemens, P. G. Anharmonic Decay of Optical Phonons. *Phys. Rev.* **148,** 845–848. https://link.aps.org/doi/10.1103/PhysRev.148.845 (1966).

55. Zhang, Y., Wang, Z., Xi, J. & Yang, J. Temperature-dependent band gaps in several semiconductors: from the role of electron–phonon renormalization. *Journal of Physics: Condensed Matter* **32,** 475503. https://dx.doi.org/10.1088/1361-648X/aba45d (2020).

56. Pötz, W. Hot-phonon effects in bulk GaAs. *Phys. Rev. B* **36,** 5016–5019. https://link.aps.org/doi/10.1103/PhysRevB.36.5016 (1987).

57. Renucci, J. B., Tyte, R. N. & Cardona, M. Resonant Raman scattering in silicon. *Phys. Rev. B* **11,** 3885–3895. https://link.aps.org/doi/10.1103/PhysRevB.11.3885 (1975).

58. Kumar, G. & Chung, P. W. Selective Phonon Stimulation Mechanism to Tune Thermal Transport. *ACS Omega* **7,** 12787–12794. https://doi.org/10.1021/acsomega.1c07364 (2022).

59. Finardi, A. M., Fasolato, C., Giugni, A., Capeccia, M., Cucini, R., Cappelluti, E., Sacchetti, F., Panaccione, G., Postorino, P., Petrillo, C. & Rossi, G. Transient photodoping and phonon dynamics in bulk and monolayer MoS2 by time resolved Raman scattering. *npj 2D Materials and Applications* **9,** 79. ISSN: 2397-7132. https://doi.org/10.1038/s41699-025-00601-0 (2025).

60. Liu, Y., Gao, Y., Zhang, S., He, J., Yu, J. & Liu, Z. Valleytronics in transition metal dichalcogenides materials. *Nano Research* **12,** 2695–2711. ISSN: 1998-0000. https://doi.org/10.1007/s12274-019-2497-2 (2019).

61. Mueller, T. & Malic, E. Exciton physics and device application of two-dimensional transition metal dichalcogenide semiconductors. *npj 2D Materials and Applications* **2,** 29. ISSN: 2397-7132. https://doi.org/10.1038/s41699-018-0074-2 (2018).

62. Zhang, X., Qiao, X.-F., Shi, W., Wu, J.-B., Jiang, D.-S. & Tan, P.-H. Phonon and Raman scattering of two-dimensional transition metal dichalcogenides from monolayer, multilayer to bulk material. *Chem. Soc. Rev.* **44,** 2757–2785. http://dx.doi.org/10.1039/C4CS00282B (2015).

63. Momma, K. & Izumi, F. *VESTA3* for three-dimensional visualization of crystal, volumetric and morphology data. *Journal of Applied Crystallography* **44,** 1272–1276. https://doi.org/10.1107/S0021889811038970 (2011).

64. Brumme, T., Calandra, M. & Mauri, F. First-principles theory of field-effect doping in transition-metal dichalcogenides: Structural properties, electronic structure, Hall coefficient, and electrical conductivity. *Phys. Rev. B* **91,** 155436. https://link.aps.org/doi/10.1103/PhysRevB.91.155436 (2015).

65. Chi, Z., Chen, H., Zhao, Q. & Weng, Y.-X. Observation of the hot-phonon effect in monolayer MoS2. *Nanotechnology* **31,** 235712. https://dx.doi.org/10.1088/1361-6528/ab79ad (2020).

66. Wang, T., Hopper, T. R., Mondal, N., Liu, S., Yao, C., Zheng, X., Torrisi, F. & Bakulin, A. A. Hot Carrier Cooling and Trapping in Atomically Thin WS2 Probed by Three-Pulse Femtosecond Spectroscopy. *ACS Nano* **17.** PMID: 36939760, 6330–6340. https://doi.org/10.1021/acsnano.2c10479 (2023).

67. Chi, Z., Chen, H., Chen, Z., Zhao, Q., Chen, H. & Weng, Y.-X. Ultrafast Energy Dissipation via Coupling with Internal and External Phonons in Two-Dimensional MoS2. *ACS Nano* **12.** PMID: 30114918, 8961–8969. https://doi.org/10.1021/acsnano.8b02354 (2018).

68. Britt, T. L., Li, Q., René de Cotret, L. P., Olsen, N., Otto, M., Hassan, S. A., Zacharias, M., Caruso, F., Zhu, X. & Siwick, B. J. Direct View of Phonon Dynamics in Atomically Thin MoS2. *Nano Letters* **22.** PMID: 35671172, 4718–4724. https://doi.org/10.1021/acs.nanolett.2c00850 (2022).

69. Pan, Y., Hildebrandt, P.-N., Zahn, D., Zacharias, M., Windsor, Y. W., Ernstorfer, R., Caruso, F. & Seiler, H. Momentum-Resolved Signatures of Carrier Screening Effects on Electron–Phonon Coupling in MoS2. *ACS Nano* **19.** PMID: 40088165, 11381–11389. https://doi.org/10.1021/acsnano.5c00744 (2025).

70. Capeccia, M., D'Alò, B. & Stellino, E. Capeccia, M. *Il Nuovo Cimento* **47,** 14670. https://doi.org/10.1393/ncc/i2024-24290-9 (2024).

71. Buscema, M., Steele, G. A., van der Zant, H. S. J. & Castellanos-Gomez, A. The effect of the substrate on the Raman and photoluminescence emission of single-layer MoS2. *Nano Research* **7,** 561–571. ISSN: 1998-0000. https://doi.org/10.1007/s12274-014-0424-0 (2014).

72. Panasci, S. E., Schilirò, E., Greco, G., Cannas, M., Gelardi, F. M., Agnello, S., Roccaforte, F. & Giannazzo, F. Strain, Doping, and Electronic Transport of Large Area Monolayer MoS2 Exfoliated on Gold and Transferred to an Insulating Substrate. *ACS Applied Materials & Interfaces* **13.** PMID: 34165956, 31248–31259. https://doi.org/10.1021/acsami.1c05185 (2021).

73. Stellino, E., D'Alò, B., Blundo, E., Postorino, P. & Polimeni, A. Fine-Tuning of the Excitonic Response in Monolayer WS2 Domes via Coupled Pressure and Strain Variation. *Nano Letters* **24.** PMID: 38506837, 3945–3951. https://doi.org/10.1021/acs.nanolett.4c00157 (2024).

74. Carvalho, B. R., Wang, Y., Mignuzzi, S., Roy, D., Terrones, M., Fantini, C., Crespi, V. H., Malard, L. M. & Pimenta, M. A. Intervalley scattering by acoustic phonons in two-dimensional MoS2 revealed by double-resonance Raman spectroscopy. *Nature Communications* **8,** 14670. ISSN: 2041-1723. https://doi.org/10.1038/ncomms14670 (2017).

75. Ermolaev, G. A., Stebunov, Y. V., Vyshnevyy, A. A., Tatarkin, D. E., Yakubovsky, D. I., Novikov, S. M., Baranov, D. G., Shegai, T., Nikitin, A. Y., Arsenin, A. V. & Volkov, V. S. Broadband optical properties of monolayer and bulk MoS2. *npj 2D Materials and Applications* **4,** 21. ISSN: 2397-7132. https://doi.org/10.1038/s41699-020-0155-x (2020).

76. König, T. A. F., Ledin, P. A., Kerszulis, J., Mahmoud, M. A., El-Sayed, M. A., Reynolds, J. R. & Tsukruk, V. V. Electrically Tunable Plasmonic Behavior of Nanocube–Polymer Nanomaterials Induced by a Redox-Active Electrochromic Polymer. *ACS Nano* **8.** PMID: 24870253, 6182–6192. https://doi.org/10.1021/nn501601e (2014).

77. Yan, R., Simpson, J. R., Bertolazzi, S., Brivio, J., Watson, M., Wu, X., Kis, A., Luo, T., Hight Walker, A. R. & Xing, H. G. Thermal Conductivity of Monolayer Molybdenum Disulfide Obtained from Temperature-Dependent Raman Spectroscopy. *ACS Nano* **8.** PMID: 24377295, 986–993. https://doi.org/10.1021/nn405826k (2014).

78. Lanzillo, N. A., Glen Birdwell, A., Amani, M., Crowne, F. J., Shah, P. B., Najmaei, S., Liu, Z., Ajayan, P. M., Lou, J., Dubey, M., Nayak, S. K. & O'Regan, T. P. Temperature-dependent phonon shifts in monolayer MoS2. *Applied Physics Letters* **103,** 093102. ISSN: 0003-6951. https://doi.org/10.1063/1.4819337 (2013).

79. Li, X., Li, J., Wang, K., Wang, X., Wang, S., Chu, X., Xu, M., Fang, X., Wei, Z., Zhai, Y. & Zou, B. Pressure and temperature-dependent Raman spectra of MoS2 film. *Applied Physics Letters* **109,** 242101. ISSN: 0003-6951. https://doi.org/10.1063/1.4968534 (2016).

80. Zhu, S. & Zheng, W. Temperature-Dependent Phonon Shifts in van der Waals Crystals. *The Journal of Physical Chemistry Letters* **12.** PMID: 34060315, 5261–5270. https://doi.org/10.1021/acs.jpclett.1c00947 (2021).

81. Lin, Z., Liu, W., Tian, S., Zhu, K., Huang, Y. & Yang, Y. Thermal expansion coefficient of few-layer MoS2 studied by temperature-dependent Raman spectroscopy. *Scientific Reports* **11,** 7037. ISSN: 2045-2322. https://doi.org/10.1038/s41598-021-86479-6 (2021).

82. Chakraborty, B., Bera, A., Muthu, D. V. S., Bhowmick, S., Waghmare, U. V. & Sood, A. K. Symmetry-dependent phonon renormalization in monolayer MoS_2 transistor. *Phys. Rev. B* **85,** 161403. https://link.aps.org/doi/10.1103/PhysRevB.85.161403 (2012).

83. Lu, X., Utama, M. I. B., Wang, X., Xu, W., Zhao, W., Owen, M. H. S. & Xiong, Q. Gate-Tunable Resonant Raman Spectroscopy of Bilayer MoS2. *Small* **13,** 1701039. https://onlinelibrary.wiley.com/doi/abs/10.1002/smll.201701039 (2017).

84. Sohier, T., Ponomarev, E., Gibertini, M., Berger, H., Marzari, N., Ubrig, N. & Morpurgo, A. F. Enhanced Electron-Phonon Interaction in Multivalley Materials. *Phys. Rev. X* **9,** 031019. https://link.aps.org/doi/10.1103/PhysRevX.9.031019 (2019).

85. Novko, D. Broken adiabaticity induced by Lifshitz transition in MoS2 and WS2 single layers. *Communications Physics* **3,** 30. ISSN: 2399-3650. https://doi.org/10.1038/s42005-020-0299-1 (2020).

86. Girotto, N., Caruso, F. & Novko, D. Ultrafast Nonadiabatic Phonon Renormalization in Photoexcited Single-Layer MoS2. *The Journal of Physical Chemistry C* **127,** 16515–16524. https://doi.org/10.1021/acs.jpcc.3c03664 (2023).

87. Fasolato, C., Stellino, E., Sacchetti, F. & Petrillo, C. Fast plasma production by intense femtosecond extreme ultraviolet and x-ray pulses. *Phys. Rev. Res.* **7,** 013072. https://link.aps.org/doi/10.1103/PhysRevResearch.7.013072 (2025).

88. Amani, M., Lien, D.-H., Kiriya, D., Xiao, J., Azcatl, A., Noh, J., Madhvapathy, S. R., Addou, R., KC, S., Dubey, M., Cho, K., Wallace, R. M., Lee, S.-C., He, J.-H., Ager, J. W., Zhang, X., Yablonovitch, E. & Javey, A. Near-unity photoluminescence quantum yield in MoS¡sub¿2¡/sub¿. *Science* **350,** 1065–1068. https://www.science.org/doi/abs/10.1126/science.aad2114 (2015).

89. Wang, H., Zhang, C. & Rana, F. Ultrafast Dynamics of Defect-Assisted Electron–Hole Recombination in Monolayer MoS2. *Nano Letters* **15.** PMID: 25546602, 339–345. https://doi.org/10.1021/nl503636c (2015).

90. Yu, Y., Yu, Y., Xu, C., Barrette, A., Gundogdu, K. & Cao, L. Fundamental limits of exciton-exciton annihilation for light emission in transition metal dichalcogenide monolayers. *Phys. Rev. B* **93,** 201111. https://link.aps.org/doi/10.1103/PhysRevB.93.201111 (2016).

91. Robert, C., Lagarde, D., Cadiz, F., Wang, G., Lassagne, B., Amand, T., Balocchi, A., Renucci, P., Tongay, S., Urbaszek, B. & Marie, X. Exciton radiative lifetime in transition metal dichalcogenide monolayers. *Phys. Rev. B* **93,** 205423. https://link.aps.org/doi/10.1103/PhysRevB.93.205423 (2016).

92. Sun, Y., Wang, R. & Liu, K. Substrate induced changes in atomically thin 2-dimensional semiconductors: Fundamentals, engineering, and applications. *Applied Physics Reviews* **4,** 011301. ISSN: 1931-9401. https://doi.org/10.1063/1.4974072 (2017).

93. Bhanu, U., Islam, M. R., Tetard, L. & Khondaker, S. I. Photoluminescence quenching in gold - MoS2 hybrid nanoflakes. *Scientific Reports* **4,** 5575. ISSN: 2045-2322. https://doi.org/10.1038/srep05575 (2014).

94. Zhang, L., Yan, H., Sun, X., Dong, M., Yildirim, T., Wang, B., Wen, B., Neupane, G. P., Sharma, A., Zhu, Y., Zhang, J., Liang, K., Liu, B., Nguyen, H. T., Macdonald, D. & Lu, Y. Modulated interlayer charge transfer dynamics in a monolayer TMD/metal junction. *Nanoscale* **11,** 418–425. http://dx.doi.org/10.1039/C8NR08728H (2019).

95. Pincelli, T., Vasileiadis, T., Dong, S., Beaulieu, S., Dendzik, M., Zahn, D., Lee, S.-E., Seiler, H., Qi, Y., Xian, R. P., Maklar, J., Coy, E., Mueller, N. S., Okamura, Y., Reich, S., Wolf, M., Rettig, L. & Ernstorfer, R. Observation of Multi-Directional Energy Transfer in a Hybrid Plasmonic–Excitonic Nanostructure. *Advanced Materials* **35,** 2209100. https://advanced.onlinelibrary.wiley.com/doi/abs/10.1002/adma.202209100 (2023).

96. Kukucska, G. & Koltai, J. Theoretical Investigation of Strain and Doping on the Raman Spectra of Monolayer MoS2. *physica status solidi (b)* **254,** 1700184. https://onlinelibrary.wiley.com/doi/abs/10.1002/pssb.201700184 (2017).

97. Zhu, C. R., Wang, G., Liu, B. L., Marie, X., Qiao, X. F., Zhang, X., Wu, X. X., Fan, H., Tan, P. H., Amand, T. & Urbaszek, B. Strain tuning of optical emission energy and polarization in monolayer and bilayer MoS_2. *Phys. Rev. B* **88,** 121301. https://link.aps.org/doi/10.1103/PhysRevB.88.121301 (2013).

98. Wang, Y., Cong, C., Qiu, C. & Yu, T. Raman Spectroscopy Study of Lattice Vibration and Crystallographic Orientation of Monolayer MoS2 under Uniaxial Strain. *Small* **9,** 2857–2861. https://onlinelibrary.wiley.com/doi/abs/10.1002/smll.201202876 (2013).

99. Kaźmierczak-Bałata, A., Bodzenta, J., Dehbashi, M., Mayandi, J. & Venkatachalapathy, V. Influence of Post Processing on Thermal Conductivity of ITO Thin Films. *Materials* **16.** ISSN: 1996-1944. https://www.mdpi.com/1996-1944/16/1/362 (2023).

100. Scotognella, F., Della Valle, G., Srimath Kandada, A. R., Dorfs, D., Zavelani-Rossi, M., Conforti, M., Miszta, K., Comin, A., Korobchevskaya, K., Lanzani, G., Manna, L. & Tassone, F. Plasmon Dynamics in Colloidal Cu2–xSe Nanocrystals. *Nano Letters* **11.** PMID: 21939261, 4711–4717. https://doi.org/10.1021/nl202390s (2011).

101. Sadasivam, S., Chan, M. K. Y. & Darancet, P. Theory of Thermal Relaxation of Electrons in Semiconductors. *Phys. Rev. Lett.* **119,** 136602. https://link.aps.org/doi/10.1103/PhysRevLett.119.136602 (2017).

102. Cappelluti, E., Caruso, F. & Novko, D. Properties and challenges of hot-phonon physics in metals: MgB2 and other compounds. *Progress in Surface Science* **97,** 100664. ISSN: 0079-6816. https://www.sciencedirect.com/science/article/pii/S0079681622000119 (2022).

103. Mansart, B., Cottet, M. J. G., Mancini, G. F., Jarlborg, T., Dugdale, S. B., Johnson, S. L., Mariager, S. O., Milne, C. J., Beaud, P., Grübel, S., Johnson, J. A., Kubacka, T., Ingold, G., Prsa, K., Rønnow, H. M., Conder, K., Pomjakushina, E., Chergui, M. & Carbone, F. Temperature-dependent electron-phonon coupling in $La_{2-x}Sr_xCuO_4$ probed by femtosecond x-ray diffraction. *Phys. Rev. B* **88,** 054507. https://link.aps.org/doi/10.1103/PhysRevB.88.054507 (2013).

104. Goldstein, T., Chen, S.-Y., Tong, J., Xiao, D., Ramasubramaniam, A. & Yan, J. Raman scattering and anomalous Stokes–anti-Stokes ratio in MoTe2 atomic layers. *Scientific Reports* **6,** 28024. ISSN: 2045-2322. https://doi.org/10.1038/srep28024 (2016).

105. Zardo, I., Yazji, S., Hörmann, N., Hertenberger, S., Funk, S., Mangialardo, S., Morkötter, S., Koblmüller, G., Postorino, P. & Abstreiter, G. E1(A) Electronic Band Gap in Wurtzite InAs Nanowires Studied by Resonant Raman Scattering. *Nano Letters* **13.** PMID: 23701454, 3011–3016. https://doi.org/10.1021/nl304528j (2013).

106. Sokalski, P., Han, Z., Fleming, G. C., Smith, B., Sullivan, S. E., Huang, R., Ruan, X. & Shi, L. Effects of hot phonons and thermal stress in micro-Raman spectra of molybdenum disulfide. *Applied Physics Letters* **121,** 182202. ISSN: 0003-6951. https://doi.org/10.1063/5.0122945 (2022).

107. Ortenzi, L., Pietronero, L. & Cappelluti, E. Zero-point motion and direct-indirect band-gap crossover in layered transition-metal dichalcogenides. *Phys. Rev. B* **98,** 195313. https://link.aps.org/doi/10.1103/PhysRevB.98.195313 (2018).

108. Caruso, F. Nonequilibrium Lattice Dynamics in Monolayer MoS2. *The Journal of Physical Chemistry Letters* **12.** PMID: 33569950, 1734–1740. https://doi.org/10.1021/acs.jpclett.0c03616 (2021).

109. Han, Z., Sokalski, P., Shi, L. & Ruan, X. Prediction of hot zone-center optical phonons in laser-irradiated molybdenum disulfide with a semiconductor multitemperature model. *Phys. Rev. B* **107,** L041407. https://link.aps.org/doi/10.1103/PhysRevB.107.L041407 (2023).

110. Goodman, A. J., Willard, A. P. & Tisdale, W. A. Exciton trapping is responsible for the long apparent lifetime in acid-treated MoS_2. *Phys. Rev. B* **96,** 121404. https://link.aps.org/doi/10.1103/PhysRevB.96.121404 (2017).

111. Wang, H., Zhang, C. & Rana, F. Surface Recombination Limited Lifetimes of Photoexcited Carriers in Few-Layer Transition Metal Dichalcogenide MoS2. *Nano Letters* **15.** PMID: 26535607, 8204–8210. https://doi.org/10.1021/acs.nanolett.5b03708 (2015).

112. Rustagi, A. & Kemper, A. F. Theoretical Phase Diagram for the Room-Temperature Electron–Hole Liquid in Photoexcited Quasi-Two-Dimensional Monolayer MoS2. *Nano Letters* **18.** PMID: 29215286, 455–459. https://doi.org/10.1021/acs.nanolett.7b04377 (2018).

113. Radisavljevic, B. & Kis, A. Mobility engineering and a metal–insulator transition in monolayer MoS2. *Nature Materials* **12,** 815–820. ISSN: 1476-4660. https://doi.org/10.1038/nmat3687 (2013).

114. Steinhoff, A., Florian, M., Rösner, M., Schönhoff, G., Wehling, T. O. & Jahnke, F. Exciton fission in monolayer transition metal dichalcogenide semiconductors. *Nature Communications* **8,** 1166. ISSN: 2041-1723. https://doi.org/10.1038/s41467-017-01298-6 (2017).

115. Bae, S., Matsumoto, K., Raebiger, H., Shudo, K.-i., Kim, Y.-H., Handegård, Ø. S., Nagao, T., Kitajima, M., Sakai, Y., Zhang, X., Vajtai, R., Ajayan, P., Kono, J., Takeda, J. & Katayama, I. K-point longitudinal acoustic phonons are responsible for ultrafast intervalley scattering in monolayer MoSe2. *Nature Communications* **13,** 4279. ISSN: 2041-1723. https://doi.org/10.1038/s41467-022-32008-6 (2022).

116. Liu, H. & Di Valentin, C. Band Gap in Magnetite above Verwey Temperature Induced by Symmetry Breaking. *The Journal of Physical Chemistry C* **121,** 25736–25742. https://doi.org/10.1021/acs.jpcc.7b09387 (2017).

117. Walz, F. The Verwey transition - a topical review. *Journal of Physics: Condensed Matter* **14,** R285. https://dx.doi.org/10.1088/0953-8984/14/12/203 (2002).

118. García, J. & Subías, G. The Verwey transition—a new perspective. *Journal of Physics: Condensed Matter* **16,** R145. https://dx.doi.org/10.1088/0953-8984/16/7/R01 (2004).

119. Wang, W., Li, J., Liang, Z., Wu, L., Lozano, P. M., Komarek, A. C., Shen, X., Reid, A. H., Wang, X., Li, Q., Yin, W., Sun, K., Robinson, I. K., Zhu, Y., Dean, M. P. & Tao, J. Verwey transition as evolution from electronic nematicity to trimerons via electron-phonon coupling. *Science Advances* **9,** eadf8220. https://www.science.org/doi/abs/10.1126/sciadv.adf8220 (2023).

120. Kukreja, R., Hua, N., Ruby, J., Barbour, A., Hu, W., Mazzoli, C., Wilkins, S., Fullerton, E. E. & Shpyrko, O. G. Orbital Domain Dynamics in Magnetite below the Verwey Transition. *Phys. Rev. Lett.* **121,** 177601. https://link.aps.org/doi/10.1103/PhysRevLett.121.177601 (2018).

121. Verwey, E. J. W. Electronic Conduction of Magnetite (Fe3O4) and its Transition Point at Low Temperatures. *Nature* **144,** 327–328. ISSN: 1476-4687. https://doi.org/10.1038/144327b0 (1939).

122. Senn, M. S., Wright, J. P. & Attfield, J. P. Charge order and three-site distortions in the Verwey structure of magnetite. *Nature* **481,** 173–176. ISSN: 1476-4687. https://doi.org/10.1038/nature10704 (2012).

123. De Jong, S., Kukreja, R., Trabant, C., Pontius, N., Chang, C. F., Kachel, T., Beye, M., Sorgenfrei, F., Back, C. H., Bräuer, B., Schlotter, W. F., Turner, J. J., Krupin, O., Doehler, M., Zhu, D., Hossain, M. A., Scherz, A. O., Fausti, D., Novelli, F., Esposito, M., Lee, W. S., Chuang, Y. D., Lu, D. H., Moore, R. G., Yi, M., Trigo, M., Kirchmann, P., Pathey, L., Golden, M. S., Buchholz, M., Metcalf, P., Parmigiani, F., Wurth, W., Föhlisch, A., Schüßler-Langeheine, C. & Dürr, H. A. Speed limit of the insulator–metal transition in magnetite. *Nature Materials* **12,** 882–886. ISSN: 1476-4660. https://doi.org/10.1038/nmat3718 (2013).

124. Randi, F., Vergara, I., Novelli, F., Esposito, M., Dell'Angela, M., Brabers, V. A. M., Metcalf, P., Kukreja, R., Dürr, H. A., Fausti, D., Grüninger, M. & Parmigiani, F. Phase separation in the nonequilibrium Verwey transition in magnetite. *Phys. Rev. B* **93,** 054305. https://link.aps.org/doi/10.1103/PhysRevB.93.054305 (2016).

125. Wang, W., Li, J., Wu, L., Sears, J., Ji, F., Shen, X., Reid, A. H., Tao, J., Robinson, I. K., Zhu, Y. & Dean, M. P. M. Dual-stage structural response to quenching charge order in magnetite. *Phys. Rev. B* **106,** 195131. https://link.aps.org/doi/10.1103/PhysRevB.106.195131 (2022).

126. Truc, B., Usai, P., Pennacchio, F., Berruto, G., Claude, R., Madan, I., Sala, V., LaGrange, T., Vanacore, G. M., Benhabib, S. & Carbone, F. Ultrafast generation of hidden phases via energy-tuned electronic photoexcitation in magnetite. *Proceedings of the National Academy of Sciences* **121,** e2316438121. https://www.pnas.org/doi/abs/10.1073/pnas.2316438121 (2024).

127. Borroni, S., Teyssier, J., Piekarz, P., Kuzmenko, A. B., Oleś, A. M., Lorenzana, J. & Carbone, F. Light scattering from the critical modes of the Verwey transition in magnetite. *Phys. Rev. B* **98,** 184301. https://link.aps.org/doi/10.1103/PhysRevB.98.184301 (2018).

128. Borroni, S. *New Insights into the Verwey Transition in Magnetite* PhD thesis (École Polytechnique Fédérale de Lausanne, 2018).

129. Shebanova, O. N. & Lazor, P. Raman spectroscopic study of magnetite (FeFe2O4): a new assignment for the vibrational spectrum. *Journal of Solid State Chemistry* **174,** 424–430. ISSN: 0022-4596. https://www.sciencedirect.com/science/article/pii/S0022459603002949 (2003).

130. Piekarz, P., Legut, D., Baldini, E., Belvin, C. A., Kołodziej, T., Tabiś, W., Kozłowski, A., Kakol, Z., Tarnawski, Z., Lorenzana, J., Gedik, N., Oleś, A. M., Honig, J. M. & Parlinski, K. Trimeron-phonon coupling in magnetite. *Phys. Rev. B* **103,** 104303. https://link.aps.org/doi/10.1103/PhysRevB.103.104303 (2021).

131. Gasparov, L. V., Tanner, D. B., Romero, D. B., Berger, H., Margaritondo, G. & Forró, L. Infrared and Raman studies of the Verwey transition in magnetite. *Phys. Rev. B* **62,** 7939–7944. https://link.aps.org/doi/10.1103/PhysRevB.62.7939 (2000).

132. Baghaie Yazdi, M., Choi, K.-Y., Wulferding, D., Lemmens, P. & Alff, L. Raman study of the Verwey transition in magnetite thin films. *New Journal of Physics* **15,** 103032. https://iopscience.iop.org/article/10.1088/1367-2630/15/10/103032 (2013).

133. Gasparov, L. V., Rush, A., Güntherodt, G. & Berger, H. Electronic Raman scattering in magnetite: Spin versus charge gap. *Phys. Rev. B* **79,** 144303. https://link.aps.org/doi/10.1103/PhysRevB.79.144303 (2009).

134. Orgiani, P., Chaluvadi, S. K., Chalil, S. P., Mazzola, F., Jana, A., Dolabella, S., Rajak, P., Ferrara, M., Benedetti, D., Fondacaro, A., Salvador, F., Ciancio, R., Fujii, J., Panaccione, G., Vobornik, I. & Rossi, G. Dual pulsed laser deposition system for the growth of complex materials and heterostructures. *Review of Scientific Instruments* **94,** 033903. ISSN: 0034-6748. https://doi.org/10.1063/5.0138889 (2023).

135. Li, X. W., Gupta, A., Xiao, G. & Gong, G. Q. Transport and magnetic properties of epitaxial and polycrystalline magnetite thin films. *Journal of Applied Physics* **83,** 7049–7051. ISSN: 0021-8979. https://doi.org/10.1063/1.367547 (1998).

136. Piekarz, P., Parlinski, K. & Ole ś, A. M. Origin of the Verwey transition in magnetite: Group theory, electronic structure, and lattice dynamics study. *Phys. Rev. B* **76,** 165124. https://link.aps.org/doi/10.1103/PhysRevB.76.165124 (2007).

137. Verble, J. L. Temperature-dependent light-scattering studies of the Verwey transition and electronic disorder in magnetite. *Phys. Rev. B* **9,** 5236–5248. https://link.aps.org/doi/10.1103/PhysRevB.9.5236 (1974).

138. Saleh, B. E. A. & Teich, M. C. in *Fundamentals of Photonics* 80–107 (John Wiley and Sons, Ltd, 1991). ISBN: 9780471213741. https://onlinelibrary.wiley.com/doi/abs/10.1002/0471213748.ch3.

List of abbreviations

1L	Monolayer.
ARPES	Angle-Resolved Photoemission Spectroscopy.
BZ	Brillouin Zone.
CBM	Conduction Band Minimum.
CCD	Charge-Coupled Device.
CW	Continuous-Wave.
FWHM	Full-Width Half Maximum.
FSRS	Femtosecond Stimulated Raman Scattering.
HHG	High-Harmonic Generation.
ITO	Indium-Tin Oxide.
LA	Longitudinal Acoustic.
LO	Longitudinal Optical.
MIT	Metal-Insulator Transition.
NA	Numerical Aperture.
OPA	Optical-Parametric Amplifier.
TG	Transient Grating spectroscopy.
TMD	Transition Metal Dichalcogenides.
TR	Time-Resolved.
TRRS	Time-Resolved spontaneous Raman Spectroscopy.
TRPES	Time-Resolved Photoemission Spectroscopy.

TR-XRD Time-Resolved X-Ray Diffraction.

UED Ultrafast Electron Diffraction.

UEDS Ultrafast Elecron Diffuse Scattering.

UHV Ultra-High Vacuum.

VBM Valence Band Maximum.

WD Working Distance.

List of publications

Refereed publications

A.M. Finardi, C. Fasolato, A. Giugni, R. Cucini, A. Fondacaro, G.M. Pierantozzi, D. Benedetti, F. Sacchetti, P. Postorino, G. Panaccione, C. Petrillo and G. Rossi, *A UHV-compatible, time-resolved spontaneous Raman spectrometer for multi-messenger ultrafast studies: design and applications to photoinduced dynamics*, Structural Dynamics 12, 064302 (2025).

DOI: 10.1063/4.0000780

A.M. Finardi, C. Fasolato, A. Giugni, M. Capeccia, R. Cucini, E. Cappelluti, F. Sacchetti, G. Panaccione, P. Postorino, C. Petrillo and G. Rossi, *Transient photodoping and phonon dynamics in bulk and monolayer MoS_2 by time resolved Raman scattering*, npj 2D Materials and Applications 9, 79 (2025).

DOI: 10.1038/s41699-025-00601-0

D. Dagur, **A.M. Finardi**, V. Polewczyk, A.Y. Petrov, S. Dolabella, F. Motti, H. Sharma, E. Dobovicnik, A. Giugni, G. Rossi, C. Fasolato, P. Torelli and G. Vinai, *Thermal Treatment Effects on PMN-$_{0.4}$PT/Fe Multiferroic Heterostructures*, ACS Applied Electronic Materials 6 (9), 6648-6656 (2024).

DOI: 10.1021/acsaelm.4c01095

G.M. Pierantozzi, A. De Vita, R. Cucini, **A.M. Finardi**, T. Pincelli, F. Sirotti, J. Fujii, C. Dri, G. Brajnik, R. Sergo, G. Cautero, G. Panaccione and G. Rossi, *Relevance of thermal disorder in the electronic and spin ultrafast dynamics of iron in the low-perturbation regime*, Physical Review B 109 (6), 064411 (2024).

DOI: 10.1103/PhysRevB.109.064411

Acknowledgments

Just when you feel like you're out on your own
Just look over you shoulder, you're not alone

Big Brother & The Holding Company, *Call On Me*

Nessuna persona è un'isola, meno che mai nella scienza, che può essere una buona scienza solo se fatta di confronti, scambi di punti di vista e di conoscenze pratiche e collaborazioni quotidiane. Questa tesi racchiude quindi sforzi non solo miei per costruire, misurare, analizzare, interpretare. Questa sezione è dedicata perciò a ringraziare di cuore chi ha contribuito a questa tesi e a questi anni di dottorato, dall'interno del laboratorio, dal "mondo esterno", o un po' a cavallo dei due.

Il primo ringraziamento va al prof. Giorgio Rossi, per essere stato una guida e un supporto costante durante tutto il dottorato. Sono particolarmente grata per la libertà e l'autonomia che mi ha lasciato nel lavoro di ricerca, ma essendo sempre pronto a offrire suggerimenti puntuali e ad indicare nuove direzioni scientifiche. La sua capacità di unire una visione ampia e di lungo periodo della ricerca con la voglia di ragionare approfonditamente su ogni esperimento (ma anche su ogni intoppo o miglioria tecnica), è per me di grande ispirazione. Grazie per avermi spinta sempre ad allargare lo sguardo al di fuori della comodità e sicurezza del proprio laboratorio, trasmettendomi la curiosità per tecniche diverse e argomenti e progetti nuovi, e per avermi messo a disposizione un grande numero di opportunità di crescita scientifica e personale.

Allo stesso modo, voglio ringraziare in modo sentito Giancarlo, per la pazienza e la capacità di ascolto con cui gestisce la vita quotidiana a Sprint. Grazie per aver trovato soluzioni a tutti i problemi piccoli e grandi con cui ti sono venuta a disturbare, bilanciando la mia cocciutaggine con una visione più ampia del lavoro e della scienza, e per la capacità di rassicurare con ironia e pragmaticità romane. Grazie per considerare sempre, quando chiediamo consiglio, la dimensione personale oltre a quella professionale.

Un immenso grazie va a Claudia, in egual misura dal punto di vista professionale e personale, per essere stata un esempio di scienziata e un supporto costante in laboratorio e fuori. Per aver condiviso le frustrazioni delle giornate no al tavolo ottico e le gioie dei risultati, per aver ragionato con me su ogni dato e ogni analisi, e per avermi mostrato una strada per fare scienza in modo collettivo ed entusiasmandosi, che mi auguro di seguire per molti anni futuri. Grazie anche per avere sempre uno sguardo al ruolo politico e sociale di ciò che facciamo e infine per essere un'amica fidata.

Un grande grazie va ad Andrea, per aver con pazienza e dedizione lavorato alla costruzione e al miglioramento costante del setup. Per essere una fonte inesauribile di conoscenze tecniche sul Raman, sull'ottica, sull'elettronica e su qualsiasi cosa possa venire in mente di costruire e automatizzare, e per aver avuto la disponibilità e la pazienza di necessarie a trasmettermene almeno una piccola parte.

Difficile esprimere quanto sia grata a tutti gli Sprinters. Trovare un gruppo così accogliente e unito, capace di rendere leggero il lavoro quotidiano, è una fortuna tutt'altro che banale. Grazie a Riccardo, per aver creato dal nulla la mia confidenza con i laser e con il tavolo ottico, insegnandomi il bello di "smanettare" e che nessun errore di allineamento è per sempre se si ha la pazienza di tornare indietro a correggerlo; ma più di tutto grazie per avermi portata a vedere il Cabildo. Ringrazio Gian, per il supporto che ha dato a me come a tutti i dottorandi di Sprint, pronto ad aiutare in ogni esperimento come se fosse suo, per l'entusiasmo e la leggerezza che porta nel gruppo e per aver sempre voglia di parlare di scienza, per avermi trasmesso la FOMO da beamtime e la carica anche nei turni di notte, per avermi fatto scoprire lo spritz pompelmo e per essere fonte di giri di amici e gite al mare che hanno sicuramente reso la mia permanenza a Trieste più frizzante. E per avermi fatto apprezzare il tennis, o almeno le finali di Wimbledon.

Un sentito grazie ad Andrea per avermi insegnato a gestire il vuoto e il freddo e la disponibilità e la professionalità con cui aiuti a migliorare tutti i nostri setup, a Marta, amica di sfasi da laboratorio, fallimenti di sup e avventure ungheresi di grande successo, a Michele, esempio di precisione in laboratorio e di gentilezza in ogni circostanza, a Sara, nuova leva paziente e curiosa sempre pronta a scoppiare in una risata, e a Monika per la creatività e le numerosissime torte e tutte le proposte di pause caffè. Ringrazio anche gli Sprinters emeriti, Pietro, per la profondità di riflessione scientifica che ho avuto il piacere di osservare negli esperimenti fatti insieme e per l'ironia dei momenti ludici, e Ale, per fornire un punto di vista originale e approfondito in ogni scambio, e per le battute e foto di gatti che fa arrivare anche da oltralpe.

Grazie anche a Cristian e Schio, per l'amicizia, il supporto e la confidenza di questi anni. Forse senza tutti gli aperitivi a Barcola con voi il mio dottorato sarebbe stato più produttivo, ma sicuramente meno felice.

Infine, un grazie al mio altro gruppo di appartenenza, quello romano: a Mattia, che ha condiviso con me molte ore in laboratorio a Trieste quando era ancora il regno delle tenebre, a Elena e Beatrice, duo comico da cui ho imparato la competenza più odiata del mio dottorato (esfoliare), al prof. Postorino, che mi ha sempre seguita da lontano, e a tutta la vecchia e nuova HPS, sempre pronta ad accogliermi a braccia aperte.

Un ultimo ringraziamento va alla mia famiglia. A mia madre e a mio padre che mi hanno insegnato la curiosità verso ogni cosa e a mio fratello che da sempre la condivide con me.